ABSTRACT

Chalcogenide-Glass Negative Curvature Fibers

Chengli Wei, Ph.D.

Advisor: Jonathan Hu, Ph.D.

Hollow-core negative curvature fibers have drawn lots of attention due to their attractive properties, including a low transmission loss, a wide transmission bandwidth, low power ratio in the glass, and a simple structure. In this dissertation, we describe the history, guiding mechanism, advances, and future prospects for negative curvature fibers. We focus our studies on negative curvature fibers using chalcogenide glasses, which have low material loss in the mid-infrared region. Optical fibers used for lasers in mid-infrared region have important applications for chemical sensing, environmental monitoring, homeland security, and medical diagnostics.

We study one-dimensional slab waveguides, two-dimensional annular core fibers, and negative curvature tube-lattice fibers to illustrate the inhibited coupling guiding mechanism. Antiresonance in the glass at the core boundary and a wavenumber mismatch between the core and cladding modes inhibit coupling between the modes and have led to remarkably low loss in negative curvature fibers.

We show computational studies to design negative curvature fibers that improve the performance of the hollow core fibers. First, we compare loss in silica and chalcogenide negative curvature fibers and consider both simple and nested geometries as the transmission wavelength varies. At wavelengths shorter than 4.5 μm, silica negative curvature fibers have a loss that is around or below 10^{-1} dB/m and are preferable

to chalcogenide fibers. At wavelengths longer than 4.5 μm, it is preferable to use As_2S_3 chalcogenide or As_2Se_3 chalcogenide negative curvature fibers since their loss is one or more orders of magnitude lower than the loss of silica negative curvature fibers. Second, we find the impact of cladding tubes in chalcogenide negative curvature fibers. The leakage loss is decreased by a factor of 19 and the operating bandwidth is almost doubled when the optimal gap between cladding tubes is used in negative curvature fibers with 6 tubes. The optimal gap in a fiber with 6 cladding tubes is 3 times as large as the optimal gap in fibers with 8 or 10 cladding tubes. A larger gap is needed in a fiber with 6 cladding tubes to remove the weak coupling between the central core mode and the tube modes. Third, we study conditions for suppression of higher-order core modes in chalcogenide negative curvature fibers with an air core. An avoided crossing between the higher-order core modes and the fundamental modes in the tubes surrounding the core can be used to resonantly couple these modes, so that the higher-order core modes become lossy. Fourth, we study bend loss in chalcogenide negative curvature fibers with different polarizations, different tube wall thicknesses, and different bend directions relative to the mode polarization. The coupling between the core mode and tube modes induces bend loss peaks in the two non-degenerate modes at the same bend radius. There is as much as a factor of 28 difference between the losses of the two polarization modes. Last, we propose a polarization-filtering and polarization-maintaining negative curvature fiber in which two nested resonant tubes are added to a standard negative curvature fiber with one ring of tubes. The coupling between the glass modes in the nested resonant tubes and the fundamental core modes is used to increase the birefringence and differential loss for the fundamental core modes in the two polarizations.

At the end, we discuss the future prospects for negative curvature fibers and give a summary.

Chalcogenide-Glass Negative Curvature Fibers

by

Chengli Wei, B.S., M.S.

A Dissertation

Approved by the Department of Electrical and Computer Engineering

---

Kwang Y. Lee, Ph.D., Chairperson

Submitted to the Graduate Faculty of
Baylor University in Partial Fulfillment of the
Requirements for the Degree
of
Doctor of Philosophy

Approved by the Dissertation Committee

Jonathan Hu, Ph.D., Chairperson

Robert J. Marks, Ph.D.

Randall Jean, Ph.D.

Linda Olafsen, Ph.D.

Zhenrong Zhang, Ph.D.

Accepted by the Graduate School
May 2018

J. Larry Lyon, Ph.D., Dean

Page bearing signatures is kept on file in the Graduate School.

TABLE OF CONTENTS

LIST OF FIGURES

LIST OF TABLES

ACKNOWLEDGMENTS

First of all, I would like to thank Dr. Jonathan Hu, my dissertation supervisor, for introducing me to this fascinating dissertation topic and letting me participate in research projects. I learned a lot from him by his strict attitude on research and consistent godly behavior. I am grateful to him for patiently helping me all the time. His encouragement and support guided me to make continuous progress. I consider him as my teacher, mentor, and model for my teaching and research career.

I would like to thank Dr. Robert J. Marks, who enlightened my spiritual life. I will never forget the precious time he spent with me on Bible study and his inspiring personal stories with the Lord that he shared with me. The most precious thing that I learned from him is that I should always pray and always surrender to the Lord. I would like to thank our department chair, Dr. Kwang Y. Lee, our previous graduate director and my teacher of Advanced Electromagnetics, Dr. Randall Jean, Dr. Scott Koziol, and Prof. Miller for their help during my school years and job search process. I would like to thank my other dissertation committee members Dr. Linda Olafsen and Dr. Zhenrong Zhang for their helpful guidance and thoughtful discussions on my proposal, dissertation, and research.

I would like to thank Dr. Curtis R. Menyuk. He contributed a lot of time, effort, and ideas on our research projects. I am honored to work with such a rigorous, smart, hard-working, and respectable senior professor. Also, I appreciate his selfless and patient help during my job search process. I would like to thank Dr. Jiming Bao and the research group from the University of Houston. It is such a wonderful experience to collaborate with them on different research projects on naonophotonics. I would like to thank Dr. Francois Chenard and the support from his company IRflex. It is such a pleasant experience to collaborate with them on the research project of chalcogenide negative curvature fibers. I would like to thank my co-workers, Dr.

Joseph Weiblen and Dr. Robinson Kuis who provided many helpful suggestions during the writing and revision of our collaborative papers.

I would like to recognize my friends and colleagues, Chao Niu, Jinjie Chen, Wenlei Bai, Guiying Wu, Yanqing Liu, Fan Zhang, Dong Xue, Bin Xu, Josh Young, Larry Gee, Andre Morton, and Chenguang Li for their help in both school and life.

I would like to thank members of Waco Chinese Church. This is my second home in the USA. I enjoyed all the happy and joyful times with my brothers and sisters in my home church. The study and service in church made me grow on the way of pursuing the Lord.

I would like to thank my parents for giving me consistent and selfless support in the past thirty years. They taught me how to love, how to be thankful, and how to be humble and consistent. I believe these are the most precious treasures they have given me in my whole life. I also would like to thank my wonderful wife, Dandan Zhang, who always supported me. She contributed all her time and effort to our family and children. I could not have focused on my research and teaching without her help. She is a great wife, mother, and daughter.

Finally, I would like to thank Baylor University, where I spent my six years. This is the place where I met the Lord and started my new life in the USA. I am grateful to my friends, colleagues, and mentors at Baylor for their support and encouragement. All glory be to the Lord.

To my wife and parents

ATTRIBUTIONS

Chapter One is based on the paper "Negative curvature fibers" in the journal of *Advances in Optics and Photonics*. The first author, Chengli Wei, wrote the initial draft. The second author, R. Joseph Weiblen, analyzed data, gave helpful suggestions, and proofread the paper. The third author, Curtis R. Menyuk, suggested this research topic at the beginning, analyzed data, and contributed a lot on revision. The last author, Jonathan Hu, mentored the first author, Chengli Wei, to write this paper.

Chapter Two is based on the paper "Negative curvature fibers" in the journal of *Advances in Optics and Photonics*. The first author, Chengli Wei, carried out the main simulation work and wrote the initial draft. The second author, R. Joseph Weiblen, analyzed data, gave helpful suggestions, and proofread the paper. The third author, Curtis R. Menyuk, suggested this research topic at the beginning, analyzed data, and contributed a lot on revision. The last author, Jonathan Hu, mentored the first author, Chengli Wei, to write this paper.

Chapter Three is based on the paper "Comparison of loss in silica and chalcogenide negative curvature fibers as the wavelength varies" in the journal of *Frontiers in Physics*. The first author, Chengli Wei, carried out the main simulation work and wrote the initial draft. The second author, Jonathan Hu, worked as the advisor of the first author, Chengli Wei, to write this paper. The last author, Curtis R. Menyuk, analyzed data, gave constructive suggestions, and contributed a lot on revision.

Chapter Four is based on the paper "Impact of cladding tubes in chalcogenide negative curvature fibers" in the journal of *IEEE Photonics Journal*. The first author, Chengli Wei, carried out the main simulation work and wrote the initial draft. The second author, Curtis R. Menyuk, analyzed data, gave constructive suggestions, and contributed a lot on revision. The last author, Jonathan Hu, worked as the advisor of the first author, Chengli Wei, to write this paper.

Chapter Five is based on the paper "Higher-order mode suppression in chalcogenide negative curvature fibers" in the journal of *Optics Express*. The first author, Chengli Wei, carried out the main simulation work and wrote the initial draft. The second author, Robinson A. Kuis, suggested negative curvature fibers at the beginning of this research project and revised this paper. The third author, Francois Chenard, also suggested negative curvature fibers at the beginning of this research project and revised this paper. The fourth author, Curtis R. Menyuk, analyzed data, gave constructive suggestions, and contributed a lot on revision. The last author, Jonathan Hu, worked as the advisor of the first author, Chengli Wei, to write this paper.

Chapter Six is based on the paper "Bending-induced mode non-degeneracy and coupling in chalcogenide negative curvature fibers" in the journal of *Optics Express*. The first author, Chengli Wei, carried out the main simulation work and wrote the initial draft. The second author, Curtis R. Menyuk, analyzed data, gave constructive suggestions, and contributed a lot on revision. The last author, Jonathan Hu, worked as the advisor of the first author, Chengli Wei, to write this paper.

Chapter Seven is based on the paper "Polarization-filtering and polarization-maintaining low-loss negative curvature fibers" in the journal of *Optics Express*. The first author, Chengli Wei, carried out the main simulation work and wrote the initial draft. The second author, Curtis R. Menyuk, analyzed data, gave constructive suggestions, and contributed a lot on revision. The last author, Jonathan Hu, worked as the advisor of the first author, Chengli Wei, to write this paper.

Chapter Eight is based on the paper "Negative curvature fibers" in the journal of *Advances in Optics and Photonics*. The first author, Chengli Wei, wrote the initial draft. The second author, R. Joseph Weiblen, analyzed data, gave helpful suggestions, and proofread the paper. The third author, Curtis R. Menyuk, suggested this research topic at the beginning, analyzed data, and contributed a lot on revision. The last author, Jonathan Hu, mentored the first author, Chengli Wei, to write this paper.

CHAPTER ONE

Introduction

This chapter published as part of [1]: C. Wei, R. J. Weiblen, C. R. Menyuk, and J. Hu, "Negative curvature fibers," Adv. Opt. Photon. **9**, 504–561 (2017).

In this chapter, we present the history of hollow-core fibers and hollow-core negative curvature fibers. We also describe recent applications of negative curvature fibers.

1.1 History of Hollow-Core Fibers

Conventional step-index optical fibers have a higher index material in the center and a lower index material in the cladding in order to guide light by total internal reflection. Their guided modes have an effective index that is between the refractive indices of the core and cladding regions. The first microstructured optical fiber was fabricated in 1974 and consisted of a small-diameter rod supported on a thin plate in the center of a larger-diameter protective tube [2]. Research on periodic optical structures has grown rapidly [3] since photonic crystals were introduced in 1987 [4,5]. The first photonic crystal fiber (PCF) was demonstrated in 1996 [6,7]. It had a solid core with hexagonally arranged air holes along the entire length of the fiber with one missing defect hole that confined light in the central core [7,8]. In photonic crystal fibers of this type, there are one or more defect holes missing in the center, and these defects form the central core. The holey cladding forms an effective low-index material and confines the light. The effective index of the cladding is determined by the fundamental space-filling mode [8] and can be calculated using the tight-binding model [9–12]. The confinement mechanism is still effectively the same as in conventional step-index fibers that use total internal reflection. Because of the flexibility of fiber design that includes air holes in the fiber, PCFs can have attractive properties, such as higher nonlinearity, endlessly single-mode transmission, tunable dispersion, and high birefringence [8, 13–16].

In the late 1970s, a cylindrical Bragg waveguide, which consists of alternating rings of high- and low-refractive index materials, was proposed. This waveguide uses a bandgap or a forbidden gap to confine the light in the central core with a low refractive index [17, 18]. A bandgap implies that certain frequencies cannot propagate. If the light frequency is in the frequency range of the bandgap, the periodic cladding structure can confine the light in the central air core [14, 15, 19]. In addition, the effective index of the fundamental core mode will reside in the range of the bandgap [14, 15, 19]. In the late 1990s, hollow-core photonic bandgap fibers using a two-dimensional periodic cladding structure with an air core in the center attracted a large amount of interest due to their potential to realize optical properties that are not possible in conventional fibers [20, 21]. The hollow-core photonic bandgap fibers can overcome some of the fundamental limitations of conventional step-index fibers and can in theory lead to reduced transmission loss, lower nonlinearity, and a higher damage threshold [19, 22–24]. The central core, which confines the light, can be filled with gases or other materials, leading to long light-matter interaction lengths [19, 25–27]. Later, kagome fibers were also developed to obtain low-loss transmission in an air core [28–31].

Besides the periodic cladding structure, antiresonant reflection can also confine light in the region with a low refractive index. It was first studied and experimentally realized in a one-dimensional slab waveguide in 1986 [32, 33]. Two-dimensional structures with light transmission in a low-index core that use the same confinement mechanism have been studied [34–36]. Antiresonant reflective structures have been used to design the inner core boundary of photonic crystal fibers that have different cladding structures. These include kagome fibers, square-lattice hollow-core fibers, and bandgap fibers [29, 30, 37–44]. By tuning the thickness of the core boundary, the antiresonant structure can also be used to minimize the field intensity at the glass and air interface [44–46].

1.2 History of Hollow-Core Negative Curvature Fibers

Research on antiresonance and kagome fibers finally led to negative curvature fibers with a cladding that consists of one ring of tubes, taking advantage of both the simple cladding structure and the negative curvature of the core boundary [47–54]. In a negative curvature fiber, the surface normal vector of the core boundary is oppositely directed from a radial unit vector [37, 48, 55]. Figure 1.1 illustrates different kinds of curvature in core boundary. Left image illustrates the positive curvature core boundary. Middle image illustrates the flat core boundary. Right image illustrates the negative curvature core boundary. The negative curvature inhibits coupling between the fundamental core mode and the cladding modes. The cladding modes are modes that reside primarily inside the tubes, in the glass, or in the interstices between the tubes and the outer glass ring. Antiresonance is necessary to inhibit coupling between core and cladding modes in negative curvature fibers, but it is not sufficient. A combination of antiresonance in the glass at the core boundary and a wavenumber mismatch between the core and the cladding modes inhibits coupling between the modes and has led to remarkably low loss. By taking advantage of inhibited coupling, silica negative curvature fibers have been demonstrated with low

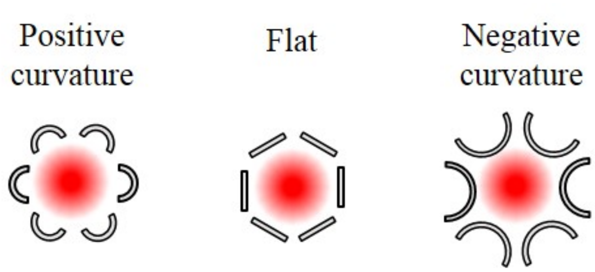

Figure 1.1: Different kinds of curvature in core boundary. Red contour indicates mode profile.

transmission loss on the order of 10 dB/km [37, 50–53, 56–61]. Lower losses are relative easier to achieve at larger core diameters [62]. Many analyses have been done on negative curvature fibers to study the effect on the fiber loss of the curvature of core boundary, the number of cladding tubes, the thickness of the tubes, and the bend radius [43, 63–72]. Enhancements of negative curvature fibers have also been suggested, including fibers with gaps between the cladding tubes [43,66–69] and fibers that include one or more nested tubes with additional reflecting surfaces [43, 65, 66]. Since no bandgap is used in negative curvature fibers, there is no requirement for a periodic cladding structure. The simplicity of the negative curvature structure opens up the possibility of fabricating fiber devices for mid-infrared (IR) applications using non-silica glasses [73–77], such as chalcogenide, since the development of hollow-core chalcogenide fibers has been hampered by fabrication difficulties [55, 78, 79].

Figure 1.2 shows scanning electron micrographs (SEMs) of hollow-core fibers with a negative curvature core-cladding interface. In particular, Figs. 1.2(a) and 1.2(c) show negative curvature fibers with six [80] and seven [58] cladding tubes to suppress higher-order core modes. Figure 1.2(b) shows a negative curvature fiber for Raman spectroscopy using ethanol [81]. Figure 1.2(d) shows a negative curvature fiber used for penalty-free 10G on-off keying data transmission through 100 m of fiber [60]. Figure 1.2(e) shows the fiber with one ring of touching tubes [49]. The loss can be further reduced by introducing a separation between the cladding tubes, as shown in Fig. 1.2(f) [51]. The mode content in a negative curvature fiber shown in Fig. 1.2(g) has been experimentally measured using spatially and spectrally resolved imaging [82]. A negative curvature fiber with a loss of 7.7 dB/km at 750 nm has been reported, as shown in Fig. 1.2(h) [57]. A negative curvature fiber with a larger separation between tubes corresponding to a small tube diameter has also been proposed for lower bend loss as shown in Fig. 1.2(i) [69]. A 10.6 μm CO_2-laser delivery system has been fabricated with a chalcogenide negative curvature fiber, as shown in Fig. 1.2(j) [55]. Figure 1.2(k) shows a chalcogenide negative curvature fiber that was fabricated using extrusion [77]. Figure 1.2(l) shows a hollow-core negative curvature fiber made with polymethylmethacrylate (PMMA) tubes for THz spectrum transmission [83]. Figure 1.2(m) shows a hollow-core negative curvature fiber [50], which has been used for high power applications in the mid-IR region [53, 84]. Figures 1.2(n) and 1.2(o) show double antiresonant fibers with one small tube inside another tube [62, 85]. Figure 1.2(p) shows a hypocycloid-shaped kagome fiber, in

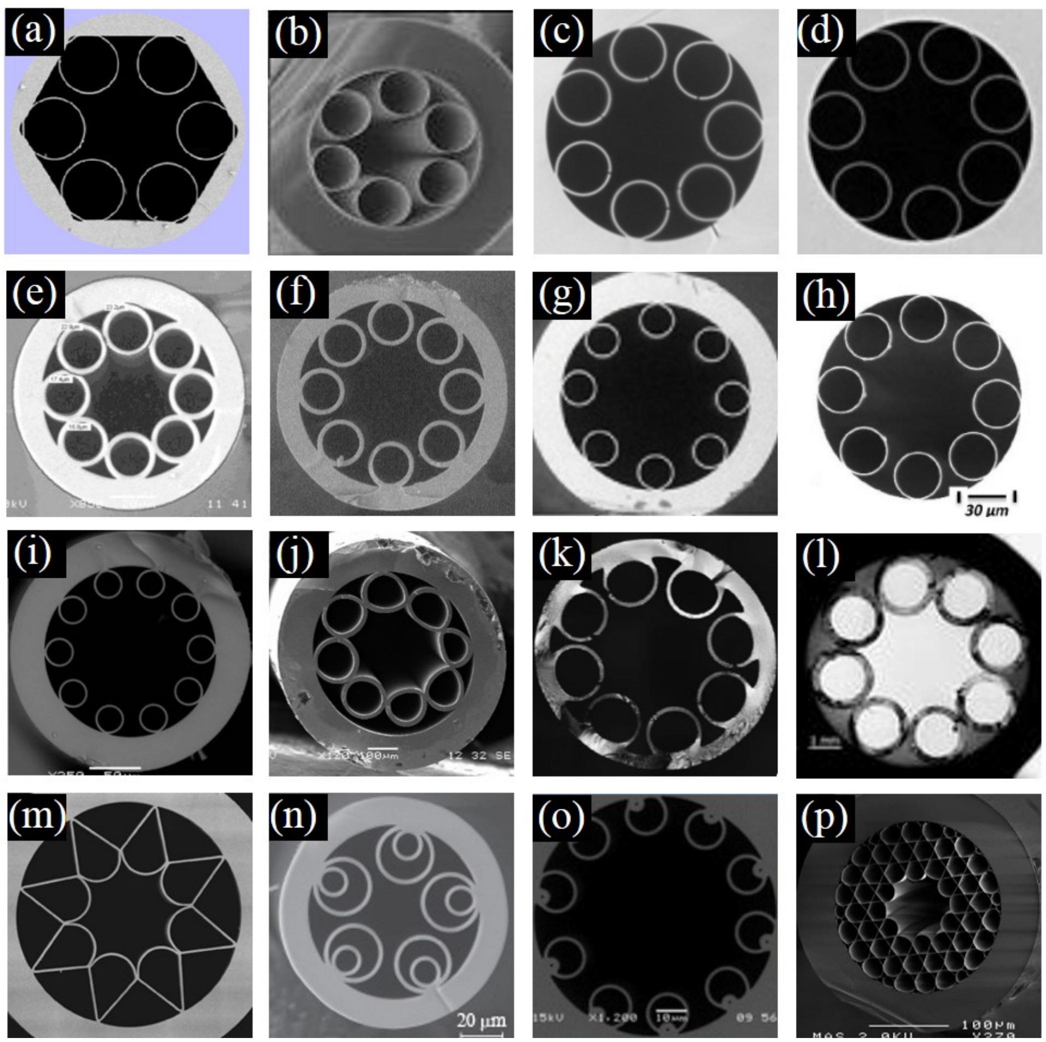

Figure 1.2: Scanning electron micrographs (SEMs) of negative curvature fibers listed in Table 1.1.

Table 1.1. Parameters in negative curvature fibers

Figure	Fiber material	Core diameter	Wall thickness	Loss	Wavelength	Ref
(a)	Silica	30 μm	0.44 μm	0.18 dB/m	1.6 μm	[80]
(b)	Silica	32 μm	0.25 μm	100 dB/km	1.3 μm	[81]
(c)	Silica	30 μm	0.83 μm	30 dB/km	1.09 μm	[58]
(d)	Silica	40.2 μm	0.359 μm	25 dB/km	1.2 μm	[60]
(e)	Silica	27 μm	2.0 μm	$<$1 dB/m	1 μm	[49]
(f)	Silica	119 μm	6 μm	50 dB/km	3.39 μm	[51]
(g)	Silica	70 μm	1.2 μm	0.68 dB/m	1.5 μm	[82]
(h)	Silica	41 μm	0.545 μm	7.7 dB/km	0.75 μm	[57]
(i)	Silica	109 μm	2.4 μm	100 dB/km	3.1 μm	[69]
(j)	Chalcogenide	380 μm	18 μm	11 dB/m	10.6 μm	[55]
(k)	Chalcogenide	172 μm	7 μm	2.1 dB/m	10 μm	[77]
(l)	PMMA	3.24 mm	252 μm	0.16 dB/cm	362 μm	[83]
(m)	Silica	94 μm	2.66 μm	34 dB/km	3.05 μm	[50]
(n)	Silica	25 μm	2.3 μm	75 dB/km	1.85 μm	[62]
(o)	Silica	51 μm	1.27 μm	175 dB/km	0.48 μm	[85]
(p)	Silica	60 μm	1.4 μm	17 dB/km	1.064 μm	[37, 86]

which curvature of the core boundary can be adjusted [37,86]. Table 1.1 displays the parameters of the fibers that are shown in Fig. 1.2.

In the literature, negative curvature fibers are referred to as hollow or hollow-core antiresonant fibers [64, 65, 69, 85, 87–91], hypocycloid-shaped hollow-core photonic crystal fibers [37, 38, 48, 86, 92–97], inhibited coupling fibers [95, 98–101], negative curvature fibers [51–55, 63, 67, 68, 70, 78, 102], revolver fibers [62, 103–106], and tube lattice fibers [83, 107–113]. Since all these fibers take advantage of negative curvature in the region surrounding the central core, we will refer to them collectively as negative curvature fibers, which are the focus of this dissertation. Hollow-core fibers with straight membranes in the region surrounding the central core also use antiresonant reflection which contributes to inhibited coupling [30, 41, 42, 114–117]. However, they do not use negative curvature and are outside the scope of this dissertation.

1.3 Recent Applications of Negative Curvature Fibers

In this section, we describe results that have appeared in Refs. [50, 53, 54, 84, 118], to explain the recent applications of negative curvature fibers, including mid-IR fiber lasers, micromachining, and surgical procedures.

1.3.1 Mid-IR Fiber Lasers

The invention of hollow-core fibers and their ability to host gases for long interaction lengths and micron-scale mode areas have enabled new gas-filled hollow-core fiber lasers. Wang *et al.* demonstrated mid-IR emission using acetylene-filled hollow-core negative curvature fibers [84]. The fiber had a core diameter of 109 μm, a tube diameter of 27.9 μm, a silica wall thickness of 2.4 μm, and a fiber length of 10.5 m. The pump diode laser had a wavelength of 1530.37 nm, a repetition rate of 10 kHz, and a pulse duration of 20 ns. The loss at the pump wavelength of 1.53 μm was 0.11 dB/m. The loss was 0.1 dB/m near the output laser wavelengths of 3.1–3.2 μm. The fiber was filled with acetylene using two gas cells. This pumping creates an immediate population inversion, which leads to two lasing lines at wavelengths of 3.12 μm and 3.16 μm.

By properly designing the fiber's transmission bands, and carefully selecting active gases and pump lasers, efficient, compact, high-power mid-IR fiber gas lasers can potentially be obtained at a number of wavelengths. Negative curvature fibers with a low transmission loss, a wide bandwidth, a large core size, and a high damage threshold can play an important role in hollow-core gas fiber lasers [119, 120]. In addition, the pulse propagation in the hollow-core fiber has a very low nonlinearity, which can be used to increase the cavity length of the fiber laser loop.

1.3.2 Micromachining

High power lasers are widely used in micromachining because of their accuracy and flexibility. Unfortunately, nonlinearity limits high power delivery in solid-core optical fibers. Hollow-core fibers confine the light inside a hollow air core surrounded by a photonic crystal cladding, which can provide low loss and high power transmission [22]. Negative curvature fibers, as one kind of hollow-core fiber, can be used for high power delivery by taking advantage of low nonlinearity, a high damage threshold, and low material absorption because most of the light power propagates in the air core. Jaworski *et al.* [54] showed that high-average-power picosecond and nanosecond pulse delivery using negative curvature fibers can be used for micromachining. The fiber used in this experiment was a silica negative curvature hollow-core fiber fabricated by the commonly stack and draw technique [50]. Experiments were carried out to demonstrate high-quality machining of 0.15 mm thick fused silica using a TRUMPF TruMicro picosecond laser. The wavelength was 1030 nm, the duration was 6 ps, the pulse energy was 52 μJ, and the repetition rate of the laser pulses was 400 kHz. The fiber had a length of 1 m and an attenuation of 0.23 dB/m at 1030 nm. The micro-milled pattern had been realized using a laser pulse that is transmitted by a negative curvature fiber with no cracks on the glass sample. The spot diameter of the focused laser at the workpiece was calculated to be 36 μm and the marking speed was 100 mm/s, which makes it possible to fabricate features with the dimensions less than 1 mm $\times$ 1 mm with a depth of 30 μm. It is hard to achieve crack-free machining of glass with picosecond pulses that are delivered at wavelengths near 1 μm using solid-core large mode-area fibers or conventional hollow-core fibers due to the low damage threshold and nonlinear effects in the short pulse regime. Later, 10 meter-long kagome fibers were also used for laser micromachining in glass sheet [121].

Precision machining experiments at wavelengths of 532 nm and 515 nm were also carried out in negative curvature fibers [122]. The energy threshold damage was measured to be 5 mJ level in hypocycloid-shaped kagome fibers [123, 124]. The energy handling capability of these fibers is higher than that of standard hollow-core bandgap fibers [93] and conventional silica fibers. Hence, negative curvature fibers provide a strong candidate for a solution to high power handling requirements.

1.3.3 Surgical Procedures

Biological tissue with water absorbs mid-IR radiation very well. Mid-IR lasers can offer a safe, effective, and precise surgical cutting tool for minimally invasive surgical procedures [125,126]. The benefit includes small penetration depth, high precision, no additional pressure, and a minimal heat-affected zone to reduce collateral damage and cell death in surrounding tissue [127, 128]. A flexible transmission tool from the laser to the patient is required for successful surgery, and optical fibers are good candidates, because of their small size, weight, and flexibility. Urich *et al.* demonstrated high energy delivery through a negative curvature fiber, which can be used for soft and hard tissue ablation under both dry and aqueous conditions [53, 118]. This negative curvature fiber has a core diameter of 94 μm [50]. The attenuation of this fiber is 34 dB/km at a wavelength of 3.05 μm. An Impex High Tech ERB 15 laser was used to generate optical pulses at a wavelength of 2.937 μm, a full-width half-maximum (FWHM) of 225 μs, and a repetition rate of 15 Hz. The laser light has a focused spot size diameter of 67 μm. The maximum coupling efficiency achieved was around 35% due to a mismatch between the laser mode and fiber mode profiles. A total fiber length of 6.5 m was used, where 5.5 m of the fiber was coiled with a diameter of 0.5 m. The fiber attenuation was measured to be 0.183 dB/m at a wavelength of 2.94 μm. In order to avoid fiber contamination, the fiber end was encapsulated with a sapphire endtip, which was mounted onto the fiber using a heat-shrinking tube. The output power at the surface of the endtip was 30 mJ at 2.94 μm with a divergence half angle of 36 mrad and an energy density of larger than 500 J/cm^2 at the contact point. This energy density far exceeds the ablation thresholds necessary for biological tissue. At the same time, this energy density is well within the operating capability of the device. Using this fiber system with an endtip, soft tissue in muscle and hard tissue in bone can be ablated in both air and water. The width of the cut is around 300 μm, and the depth of the cut is 220 μm. This system for high power applications at 2.94 μm demonstrates a promising surgical device for minimally invasive surgical procedures.

Laser poration can remove the barrier skin layer, and thereby provides a route for the diffusion of applied drugs [129]. Femtosecond pulsed laser ablation was demonstrated to enhance drug delivery across the skin [130]. A negative curvature fiber was used to deliver femtosecond pulsed visible light. The optical nonlinearity and dispersive effects in conventional step-index fibers are too high for this application [130]. Light guided in the negative curvature fibers is confined to an air core with low nonlinearity and dispersion, which allows the delivery of high-peak-power femtosecond pulses [131].

1.4 Organization of Dissertation

The rest of the dissertation is organized as follows: Chapter two describes the inhibited coupling guidance mechanism in one-dimensional slab waveguides, two-dimensional annular core fibers, and negative curvature fibers. The guidance mechanism, the transmission loss, and the mode properties have been studied separately in slab waveguides [32, 33], annular core fibers [90, 107, 132], and negative curvature fibers [49–52]. Annular core fibers can be used to predict the effective indices of the modes in negative curvature fibers, although not the loss. Chapter three describes comparison of loss in silica and chalcogenide negative curvature fibers as the wavelength varies. Chapter four presents impact of cladding tubes in chalcogenide negative curvature fibers. Chapter five presents higher-order mode suppression in chalcogenide negative curvature fibers. Chapter six describes bending-induced mode non-degeneracy and coupling in chalcogenide negative curvature fibers. Chapter seven describes polarization-filtering and polarization-maintaining low-loss negative curvature fibers. We discuss future prospects for negative curvature fibers in Chapter eight. A summary is also given in Chapter eight.

CHAPTER TWO

Guidance Mechanism

This chapter published as part of [1]: C. Wei, R. J. Weiblen, C. R. Menyuk, and J. Hu, "Negative curvature fibers," Adv. Opt. Photon. **9**, 504–561 (2017).

In this chapter, we describe the guidance mechanism in negative curvature fibers. The guidance mechanism in negative curvature fibers is inhibited coupling between light that propagates in the fiber core and light that propagates in the glass, in the cladding tubes, or in the interstices between the cladding tubes and the glass wall. Antiresonance plays a critical role in inhibiting the coupling between light in the core and in other regions of the negative curvature fiber, although some wavenumber mismatch is always needed. In section 2.1, we describe antiresonant reflection in one-dimensional slab waveguides, two-dimensional annular core fibers, and negative curvature fibers. In section 2.2, we describe that a wavenumber mismatch between the core and cladding modes will contribute to inhibited coupling. The combination of antiresonance and a wavenumber mismatch between the fundamental core and the cladding modes inhibits coupling between the modes. The inhibited coupling mechanism differs significantly from the guidance mechanism in photonic bandgap fibers. In section 2.3, we compare these two guidance mechanisms. Throughout Chapter two, we use a wavelength of 1.0 μm, a refractive index of 1.45 for silica glass, and a refractive index of 1.0 for air.

2.1 Antiresonant Reflection

We show simulation results with different structures that summarize simulations that have appeared in [49, 90, 107, 133, 134], to illustrate the antiresonant reflection mechanism, the transmission loss, and the mode properties. This section illustrates the important role of antiresonant reflection in guiding the light.

2.1.1 *Slab Waveguide*

We first study the modes in a one-dimensional M-type slab waveguide. A schematic illustration of the refractive index profile of the M-type slab waveguide that extends infinitely in y- and z-directions, is shown in Fig. 2.1. The gray regions represent glass. The white regions represent air. The normalized electric field intensity of the fundamental mode is shown in Fig. 2.2. The width of the air core is 30 μm, and the glass thickness is 0.8 μm. We calculate the effective index and leakage loss for the fundamental core mode in the M-type slab waveguide, with both the mode-matching method [135,136] and the finite-element method (FEM) [137,138], as shown in Fig. 2.3. The details of the mode-matching method and the FEM for the slab waveguide can be found in Refs. [135,138]. Both the mode-matching method and the FEM can give accurate predictions for the effective index and the loss in the M-type slab waveguide. It takes 2 seconds and 11 seconds on a desktop computer with a CPU speed of 3.4 GHz using the mode-matching method and the FEM, respectively, to find the effective index of the fundamental core mode in the M-type slab waveguide shown in Fig. 2.1. The mesh size and thickness of the absorbing layers must be verified for convergence when using the FEM, leading to additional computational cost. Given the complex effective index $n_{\mathrm{comp}} = n_{\mathrm{eff}} + in_{\mathrm{imag}}$, which is what either method directly yields, the leakage loss is calculated as Loss $= 40\pi\ n_{\mathrm{imag}}/[\ln(10)\lambda]$, where λ

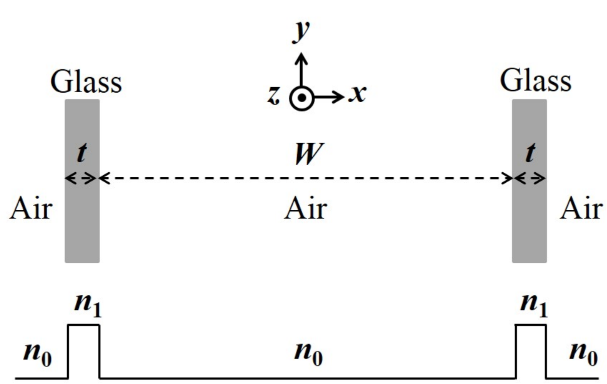

Figure 2.1. Cross section and index profile of an M-type slab waveguide.

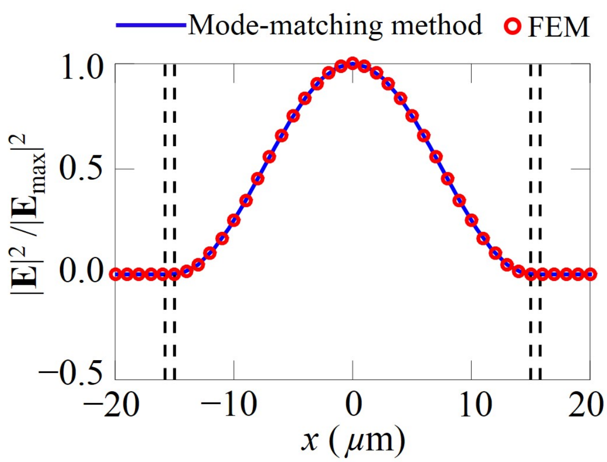

Figure 2.2: Normalized electric field intensity of the fundamental core mode in an M-type slab waveguide. The blue curve and red circles are the results from the mode-matching method and the FEM, respectively. The dashed lines indicate interfaces between air and glass.

is the wavelength [139, 140]. The effective index equals the real part of the complex effective index. As the glass thickness increases from 0.2 μm to 1.5 μm, there are three high loss thicknesses of 0.48 μm, 0.95 μm, and 1.43 μm, as shown in Fig. 2.3.

A schematic illustration of the reason for the high loss, which is due to a resonance condition, is shown in Fig. 2.4. For the core mode in the structure with a large core width where $W \gg \lambda$, the longitudinal wave vector, k_{L}, can be approximated by n_0k_0, and the transverse wave vector, k_{T}, in the glass region, can be approximated by $k_0(n_1^2 - n_0^2)^{1/2}$. The parameter $k_0 = 2\pi/\lambda$ denotes the wave vector in the air. Then, the phase difference between the waves passing through the glass slab with and without additional reflections is $2tk_0(n_1^2 - n_0^2)^{1/2}$. The resonance condition that the phase difference is a multiple of 2π yields $t = m\lambda/[2(n_1^2 - n_0^2)^{1/2}]$, where m equals any positive integer [32–34]. The values of the thickness, t, corresponding to the resonances at $m = 1$, 2, and 3, are 0.48 μm, 0.95 μm, and 1.43 μm, respectively, which correspond to the high-loss regions in Fig. 2.3(b). The minimum loss of 2.4 dB/m is the same in different transmission bands in the M-type slab waveguide. We also show

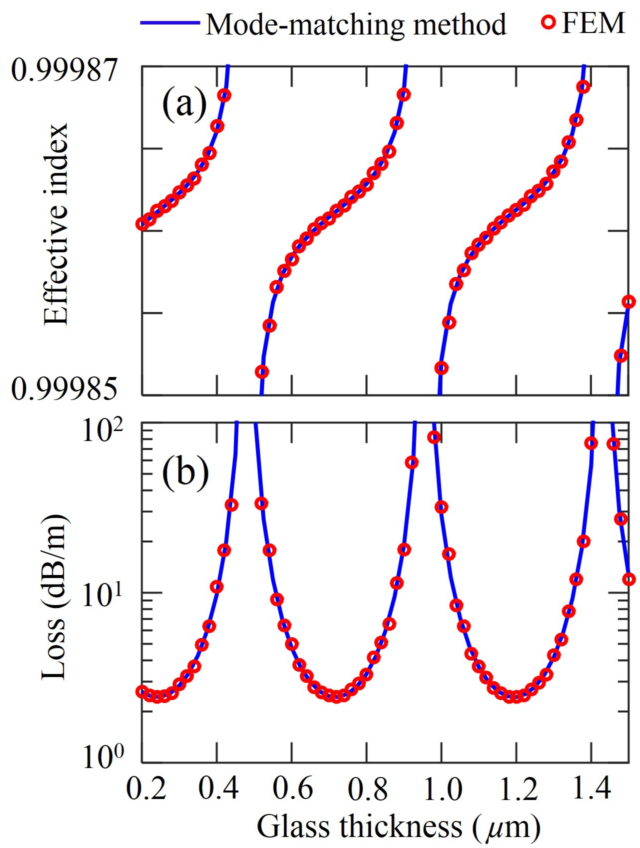

Figure 2.3: (a) Effective index and (b) leakage loss of the fundamental core mode as a function of glass layer thickness, t. The blue curves and red circles are the results from the mode-matching method and the FEM, respectively.

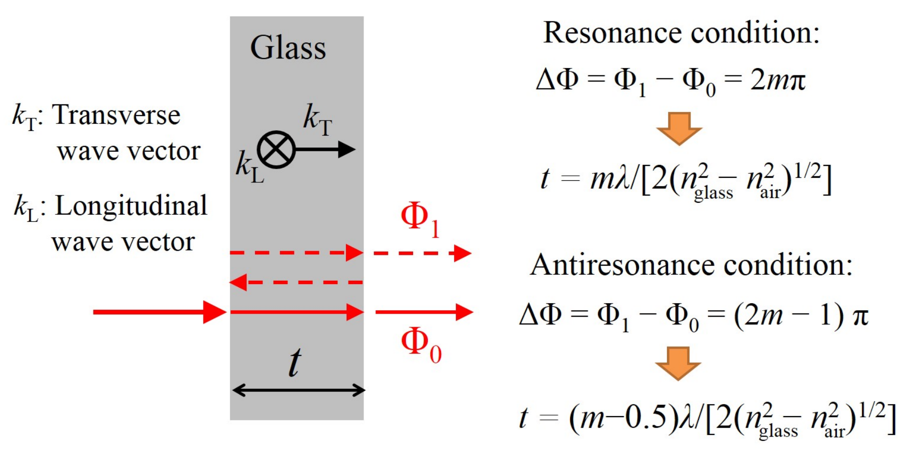

Figure 2.4. Schematic illustration of the resonance and antiresonance conditions.

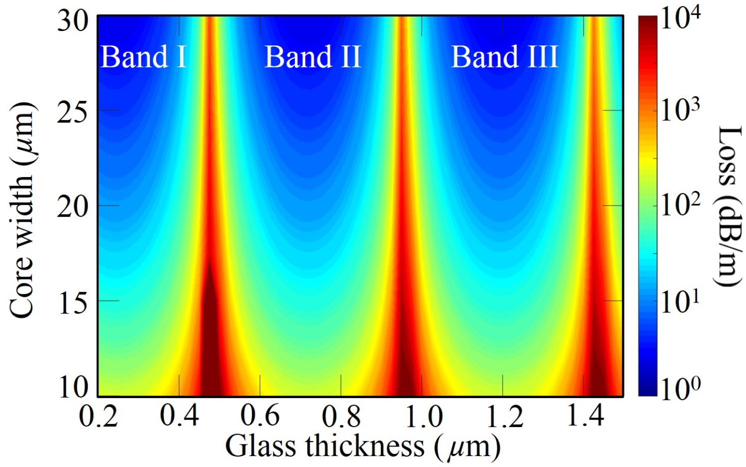

Figure 2.5: Leakage loss of the fundamental core mode in the M-type slab waveguide as a function of the glass thickness and the core width.

a contour plot of the leakage loss of the fundamental core mode as a function of the glass thickness and the air-core width in Fig. 2.5. There are three transmission bands, I, II and III near the antiresonance condition, $t = (m - 0.5)\lambda/[2(n_1^2 - n_0^2)^{1/2}]$, where m equals any positive integer [34, 141, 142]. These transmission bands are between the high-loss regions corresponding to the resonance condition at glass thicknesses of 0.48 μm, 0.95 μm, and 1.43 μm. The resonance condition does not change with different widths of the air core. The leakage loss decreases as the width of the air core increases [43, 112, 143]. Note that the resonance condition and antiresonance condition can also be derived by using the conditions of minimum and maximum reflection, respectively, from the equations for multiple-beam fringes with a plane-parallel plate [144].

2.1.2 Annular Core Fiber

The cylindrical waveguide that corresponds most closely to the M-type slab is the annular core fiber, which has a high index ring in the fiber geometry [145–147]. In Fig. 2.6, we show the cross section and the index profile along the radial direction of the annular core fiber. The gray regions represent the glass. The white regions

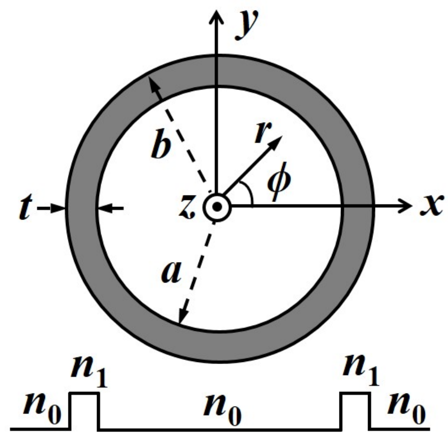

Figure 2.6: Cross section and index profile along the radial direction of an annular core fiber.

represent the air. Annular core fibers with modes that exist in the glass ring have been extensively studied [145–147]. The effective index in this case is between the refractive indices of n_0 and n_1. This section focuses on annular core fibers with modes that exist inside the central air core. These modes have an effective index that is less than either of the refractive indices n_0 or n_1 [90, 107, 132–134]. We find the core mode using the mode-matching method [145, 148] and FEM [137, 138].

Figure 2.7 shows a contour plot of the normalized electric field intensity of the fundamental core mode in an annular core fiber with an air-core diameter of 30 μm and a glass thickness of 0.8 μm. Figures 2.8(a) and 2.8(b) show the effective index and the leakage loss of the fundamental core mode as a function of glass thickness. The blue solid curves represent the results from the mode-matching method. The red circles represent results that are calculated using the FEM. We calculate the fiber modes and their propagation constants using Comsol Multiphysics, a commercial full-vector mode solver based on the FEM. Anisotropic, perfectly matched layers (PMLs) are positioned outside the cladding in order to reduce the size of the simulation window [149]. It takes 7 seconds and 29 seconds on a desktop computer with a CPU speed of 3.4 GHz using the mode-matching method and the FEM, respectively, to

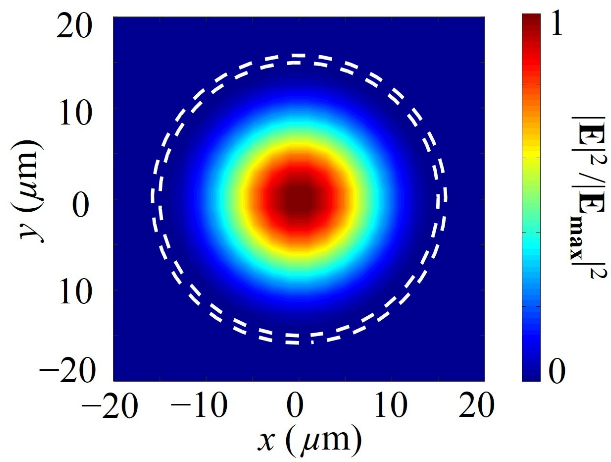

Figure 2.7: Contour plot of the normalized electric field intensity of the fundamental core mode in an annual core fiber. The white dashed lines indicate the boundaries of the glass ring.

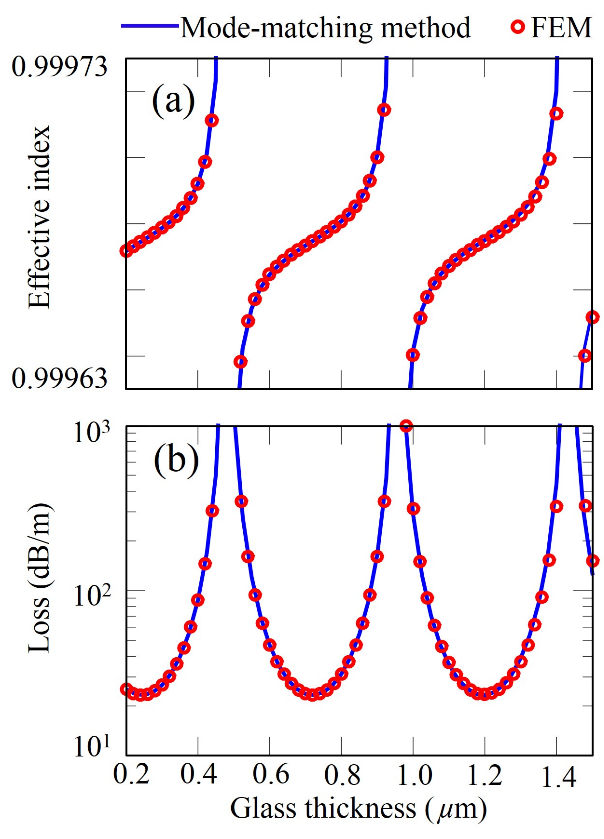

Figure 2.8: (a) Effective index and (b) leakage loss of the fundamental core mode as a function of glass thickness. The blue solid curves and red circles represent the results from the mode-matching method and the FEM, respectively.

find the effective index of the mode in the annular core fiber shown in Fig. 2.6. A longer time is required to use the FEM since a small mesh size is required in the model, especially in the thin glass regions. Also, convergence tests must be carried out on the mesh sizes in different regions of the fiber structure and on the thickness of the PML in order to obtain accurate results. While the mode-matching method runs more quickly, it can only be used in highly regular geometries like the annular core fiber, and cannot be used in irregular waveguide geometries, such as the negative curvature fibers that are shown in Fig. 1.2. We can see three high-loss regions at 0.48 μm, 0.95 μm, and 1.43 μm in Fig. 2.8(b), which are consistent with the results shown in Fig. 2.3(b) for the M-type slab waveguide. The minimum loss of 23 dB/m is the same in different transmission bands in the annual core fiber. In Fig. 2.9, we also show a contour plot of the loss of the fundamental core mode as a function of the glass thickness and the core diameter. Low-loss antiresonant transmission bands exist between the high-loss regions corresponding to the resonance condition at the glass thicknesses of 0.48 μm, 0.95 μm, and 1.43 μm. The resonance condition does not change with different air-core diameters. The leakage loss decreases as the air-core diameter increases [43, 112, 143].

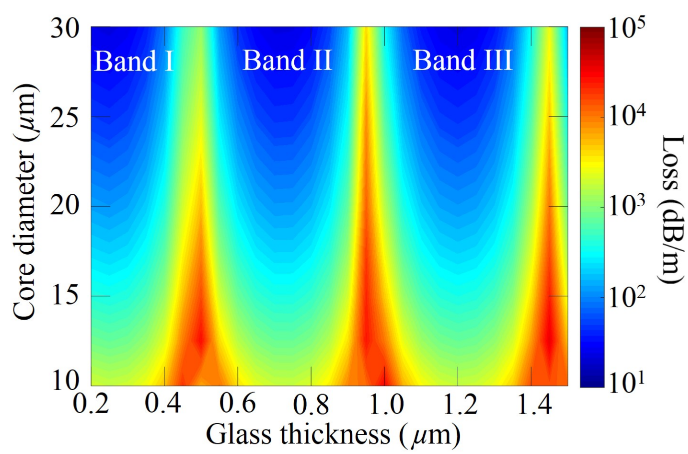

Figure 2.9: Leakage loss of the fundamental core mode in the annual core fiber as a function of the glass thickness and the core diameter.

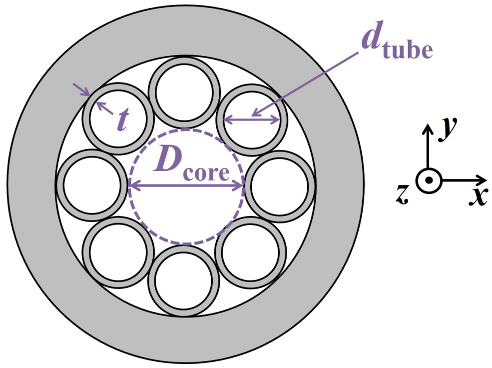

Figure 2.10. Full hollow-core negative curvature fiber geometry.

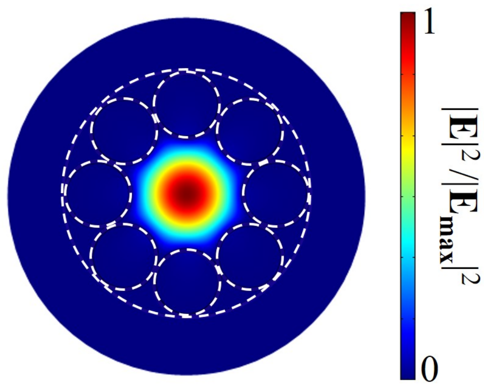

Figure 2.11: Normalized electric field intensity of the fundamental core mode in a negative curvature fiber. The white dashed curves indicate the boundaries of the glass.

2.1.3 Negative Curvature Fiber

We now consider the fundamental core mode in a simple negative curvature fiber. The full fiber geometry is shown in Fig. 2.10. The gray regions represent glass, and the white regions represent air. We model a negative curvature fiber with eight cladding tubes. The thickness of the tube walls, t, the inner tube diameter, d_{tube}, the number of tubes, p, and the core diameter D_{core}, are related by the expression $D_{\text{core}} = (d_{\text{tube}}+2t)/\sin(\pi/p)-(d_{\text{tube}}+2t)$ [58,70,141,142,150]. The normalized electric field intensity of the fundamental core mode with parameters D_{core} = 30 μm and t = 0.8 μm, is shown in Fig. 2.11. Only a quarter of the geometry is used in modeling the hollow-core fiber in Fig. 2.10 because of the symmetry of the modes [139, 151].

Figures 2.12(a) and 2.12(b) compare the effective index and leakage loss of the fundamental core mode as a function of glass thickness in the negative curvature fiber and in the annular core fiber. The results in the negative curvature fiber were obtained using the FEM, and the results in the annular core fiber were obtained using the mode-matching method. The core diameter of the annular core fiber and the negative curvature fiber are both 30 μm. In Fig. 2.12(a), the effective index of

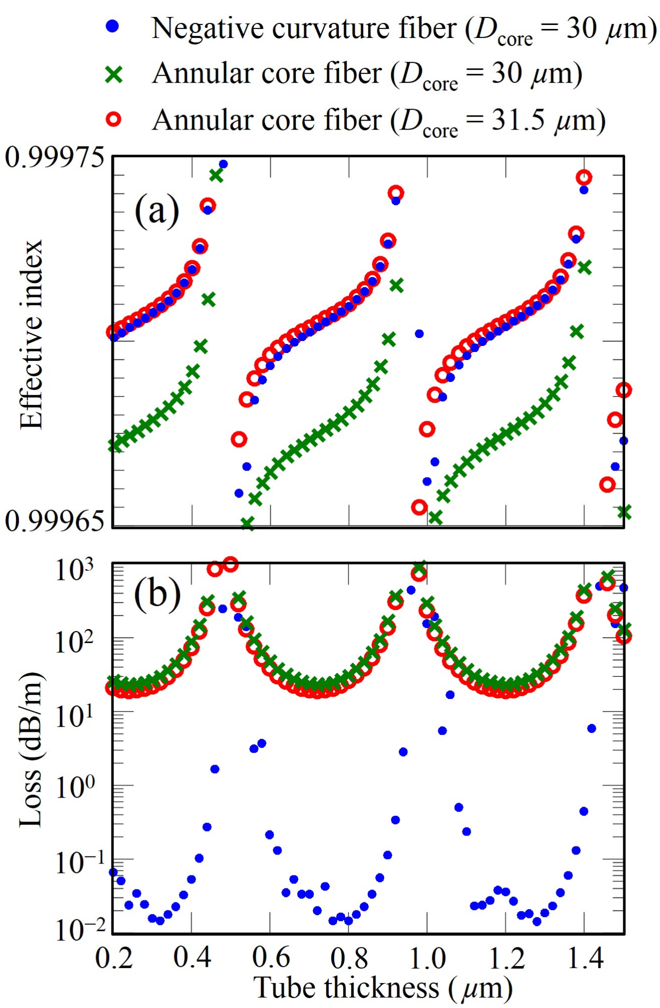

Figure 2.12: (a) Effective index and (b) leakage loss of the fundamental core mode as a function of tube thickness. The blue dots, the green crosses, and the red circles represent the results in the negative curvature fiber with a core diameter of 30 μm, the annular core fiber with a core diameter of 30 μm, and the annular core fiber with a core diameter of 31.5 μm, respectively.

the fundamental core mode in the negative curvature fiber is larger than the effective index of the fundamental core mode in the annular core fiber by 3×10^{-5}. The reason is that the negative curvature boundary effectively increases the core diameter in the negative curvature fiber [70]. We next calculate the mode in the annular core fiber with a core diameter of 31.5 μm, which is increased by 5% to compensate for the effective increase in the core diameter that occurs in a negative curvature fiber. The corresponding results for the effective index and loss for an annular core fiber with a core diameter of 31.5 μm are marked by the red circles in Fig. 2.12. With an empirical 5% increase in the core diameter, the effective indices of the core modes in the annular core fiber match the effective indices of the core modes in the negative curvature fiber when the glass thickness is in the antiresonant region in Fig. 2.12(a). In Fig. 2.12(b), the glass thicknesses corresponding to the resonance conditions or high-loss regions in the negative curvature fiber are slightly larger than the glass thicknesses in the annular core fiber. The reason is that the curvature effectively lowers the glass thickness [71]. The leakage loss decreases slightly when the core diameter increases from 30 μm to 31.5 μm in the annular core fiber. However, the leakage loss in the negative curvature fiber is lower than the leakage loss in the annular fiber by three orders of magnitude due to the negative curvature [37, 64]. Since cladding tubes are touching, localized nodes are created, and glass modes exist in the localized node area [51]. Fluctuations of the leakage loss in the transmission bands are due to the mode field in the localized node area in negative curvature fibers [37].

Figure 2.13 shows a contour plot of the leakage loss of the fundamental core mode as a function of the glass thickness and the core diameter in the negative curvature fiber. The three transmission bands are still visible between the high-loss regions, corresponding to the resonance conditions. The resonance condition does not change with different air core diameters. The leakage loss decreases as the air-core diameter increases [43, 112, 143].

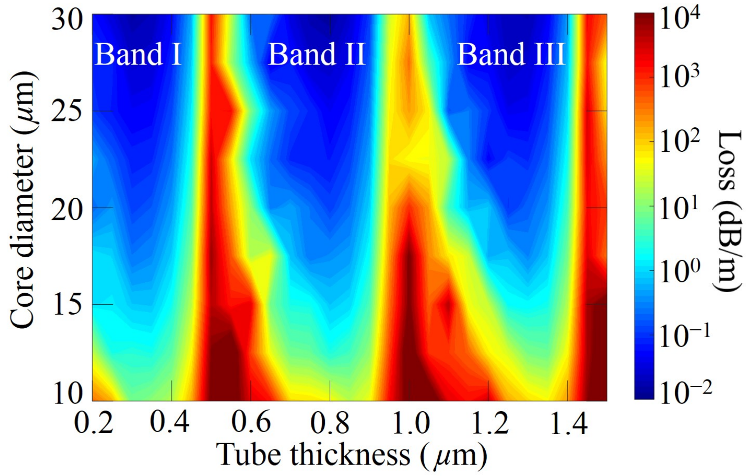

Figure 2.13: Leakage loss of the fundamental core mode in the negative curvature fiber as a function of the tube thickness and the core diameter.

The same transmission bands are obtained in simulations with silica glass that includes an imaginary refractive index of 9×10^{-8}, in accordance with the experimentally measured material loss [152]. The leakage loss increases by less than 5% compared with the previous simulation that did not include the imaginary part of the complex refractive index of the silica glass.

2.2 Inhibited Coupling

Antiresonant reflection impedes the penetration of light into the glass that surrounds the core, and is necessary to achieve the low loss that has been observed in negative curvature fibers. However, as the comparison between annular core and negative curvature fibers in sections 2.1.2 and 2.1.3 shows, it is not sufficient. More generally, the coupling between the core and cladding modes must be inhibited [37, 57]. Inhibited coupling means that leakage of the core mode into the cladding is suppressed by a strong reduction in the coupling between the core mode and the cladding modes [37, 57]. The coupling between the core and cladding modes is reduced by having a small spatial mode overlap and a mismatch of their wavenumbers or effective indices [37, 57]. In order to effectively inhibit coupling, both conditions should be met. Antiresonance reduces the mode overlap. A smaller overlap reduces in turn the wavenumber mismatch that is needed to inhibit coupling, but some mismatch is always needed.

In this section, we first review inhibited coupling in a three-slab waveguide in which glass partitions separate an air-core slab from two surrounding air-cladding slabs. We then review inhibited coupling in the simple negative curvature fiber that we considered in section 2.1.3, although here we consider the effect of decreasing in tube diameter, which creates gaps between the tubes, on the loss of the fundamental core modes. The analogy to the slab waveguide sheds useful light on the mechanism of inhibited coupling in negative curvature fiber. However, this analogy is imperfect. In particular, a correct adjustment of the gap between the cladding tubes is important in minimizing the loss of the fundamental core mode. There is no analogous parameter in the slab waveguide. Simulation results that we present summarize work that is presented in Refs. [12, 30, 37, 39, 57, 95, 98, 136, 153].

In the waveguides that we will consider here, the true modes of the waveguide are the solutions of Maxwell's equations that are obtained by solving for the modes in the complete waveguide structure. All true modes are hybrid modes and are all mutually orthogonal (or, strictly speaking, biorthogonal once losses are taken into account). The true modes are neither pure core modes nor pure cladding modes, although the power in either the core or cladding region can be very low when coupling is inhibited between the core and the cladding. Alternatively, there are approximate modes that are the mode solutions of Maxwell's equations for the stand-alone core or cladding structures. The approximate modes reside almost entirely in the core or in the cladding. These approximate modes are not orthogonal and have a non-zero overlap that leads to mode coupling. Antiresonant reflection, discussed in section 2.1, greatly reduces the overlap, but does not eliminate it. As long as the wavenumbers of the modes do not match, the effect of the overlap is weak, the approximate modes do not couple, and the true modes are well-approximated by the approximate core or cladding modes. However, when the wavenumbers match, an avoided crossing is created in which the true modes reside in both the core and the cladding. The loss of these hybrid modes is typically far larger than the loss of modes that reside almost entirely in the core. If the overlap is weak, then the frequency range over which this resonant behavior occurs is restricted, but it will always be present when the wavenumbers match. To inhibit coupling, it is thus necessary to design waveguides that minimize the overlap between the core and cladding modes and in which the wavenumbers do not match over the frequency range of interest.

2.2.1 Slab Waveguide

In this section, we describe inhibited coupling in a one-dimensional, three-layer slab waveguide with three air layers and four glass partitions. The three-layer slab waveguide is used here to study the mode coupling between the fundamental core mode that is between the two central glass partitions and the cladding mode that is between the two glass partitions on each side. Figure 2.14 shows the cross section and index profile of the waveguide. The thickness of the glass layers, t, is 0.72 μm, which corresponds to the second antiresonant thickness that we described in the previous section. We focus here on leaky modes that exist primarily in the air slabs and have effective indices that are less than the air index of 1.0. There are glass modes with effective indices greater than 1.0, which we do not consider here. The true modes in this waveguide always exist in all three air slabs, as well as the glass. However, approximate modes that exist in the individual slabs can couple. The mode coupling in this simple slab waveguide is analogous to the mode coupling in negative curvature fibers between the fundamental core modes and the tube modes. The cladding modes in the slab waveguide are the modes in the stand-alone slab waveguide 2 that is shown in the green dashed box in Fig. 2.14. The approximate core modes in the

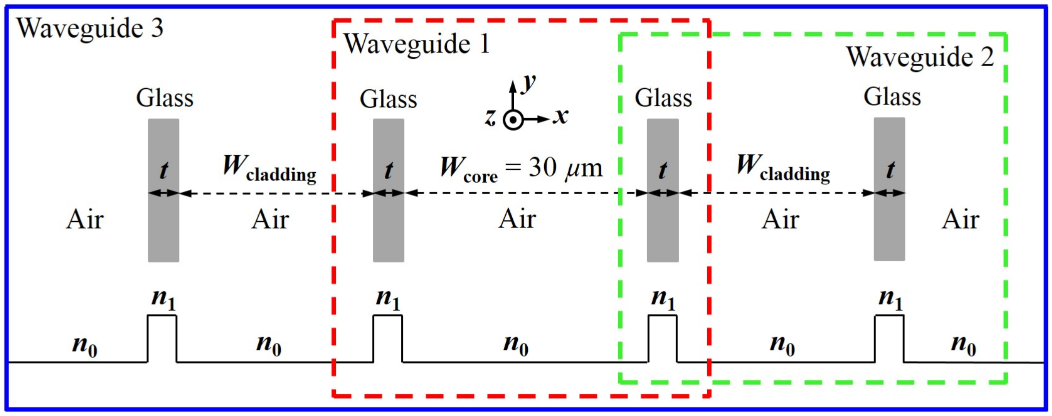

Figure 2.14: Cross section and index profile of a three-layer slab waveguide with four glass partitions. The red and green dashed boxes show the cross sections of the stand-alone slab waveguide 1 and waveguide 2, respectively.

stand-alone slab waveguide 2 will resemble the true cladding modes in the three-layer slab waveguide except near the avoided crossing.

The blue solid curve in Fig. 2.15(a) shows the effective index of the fundamental core mode as a function of the width of the air cladding, W_{cladding}, in the waveguide. The inner core width, W_{core}, is 30 μm. The effective index of the true fundamental mode in waveguide 3 has three avoided crossings. The red and green dashed curves indicate the effective indices of the modes in the stand-alone, single-slab waveguide 1 and waveguide 2, respectively, and they overlap with the solid curve except at the avoided crossings. The loss of the true fundamental core mode in the three-layer slab waveguide 3 is shown in Fig. 2.15(b). The loss is high at $W_{\text{cladding}} = 30$ μm, 60 μm, and 90 μm, when the effective indices of the core mode and cladding modes match, as shown in Fig. 2.15(a).

The high loss at $W_{\text{cladding}} = 30$ μm, 60 μm, and 90 μm can also be explained by the resonance condition in the low-index air cladding layer [32,34]. The fundamental core mode satisfies the resonance condition in the air core, $2k_T W_{\text{core}} = 2\pi$, where k_T is the transverse wave vector [154]. This resonance occurs because the phase change in one round trip of the air-core layer in the transverse direction is 2π [154].

When the low-index cladding layer satisfies the resonance condition $2k_T W_{\text{cladding}} = 2m\pi$, corresponding to $W_{\text{cladding}} = 30\ \mu\text{m}$, $60\ \mu\text{m}$, and $90\ \mu\text{m}$, the leakage loss is high, as shown in Fig. 2.15(b). Thus, we find that resonance and antiresonance in the low-index layer induce strong coupling and inhibited coupling, respectively [32, 34]. In negative curvature fibers, the thickness of the low-index layer cannot be exactly quantified; so, the analogy is not exact. However, it is qualitatively useful in understanding the role that antiresonance plays in inhibiting coupling between core modes and cladding modes.

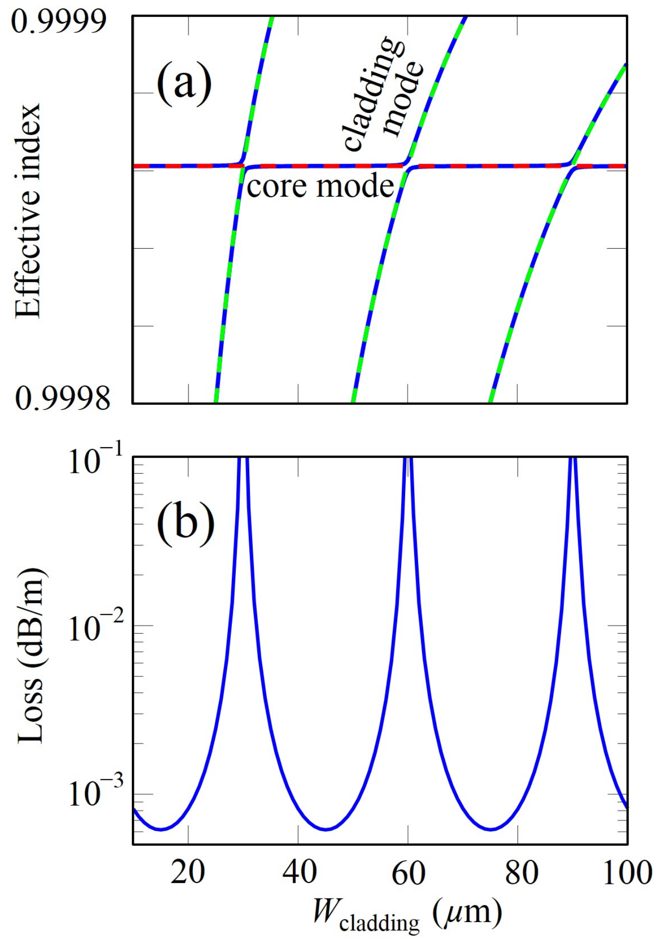

Figure 2.15: (a) Effective index of the true modes in the three-layer slab waveguide 3 (blue solid curve) and the stand-alone single-slab waveguide 1 (red dashed curve) and waveguide 2 (green dashed curve). (b) Leakage loss of the true fundamental core mode in the three-layer slab waveguide.

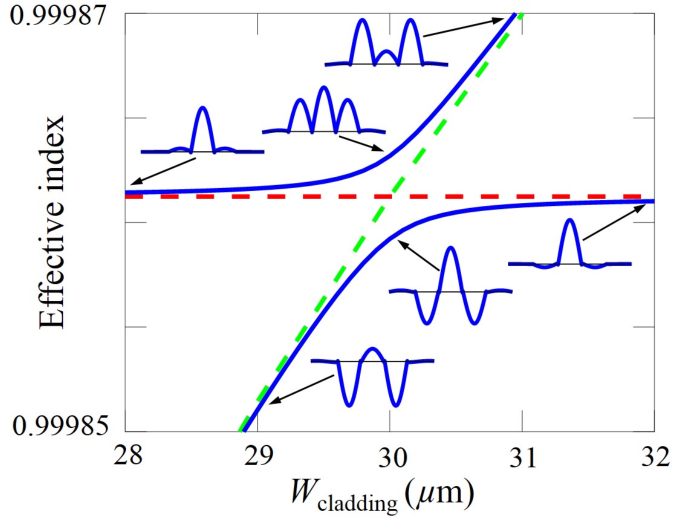

Figure 2.16: Effective indices of the air-slab modes in the three-layer slab near the avoided crossing at $W_{\text{cladding}} = 30\ \mu$m. The insets show field distributions of the true modes in the three-layer slab.

Figure 2.16 shows a blow-up of the first avoided crossing near $W_{\text{cladding}} = 30\ \mu$m in Fig. 2.15(a). The two blue solid curves are effective indices of the two true modes in the three-layer slab waveguide in Fig. 2.14. The red and green dashed lines are the effective indices of the approximate modes in waveguide 1 and waveguide 2. When $W_{\text{cladding}} < 29\ \mu$m, the indices of the two approximate modes do not match and the coupling is inhibited. The fields of the two true modes mainly reside in either waveguide 1 or waveguide 2. When $W_{\text{cladding}} = 30\ \mu$m, the indices of the two approximate modes match and coupling occurs. The avoided crossing occurs and the two true modes become hybrid modes residing in both waveguide 1 and waveguide 2. When $W_{\text{cladding}} > 31\ \mu$m, the indices of the two approximate modes do not match and the coupling is once again inhibited. The fields of the two true modes mainly reside in either waveguide 1 or waveguide 2. In the neighborhood of the avoided crossing, the two true modes switch position between the waveguide 1 and waveguide 2 as W_{cladding} increases [136, 153].

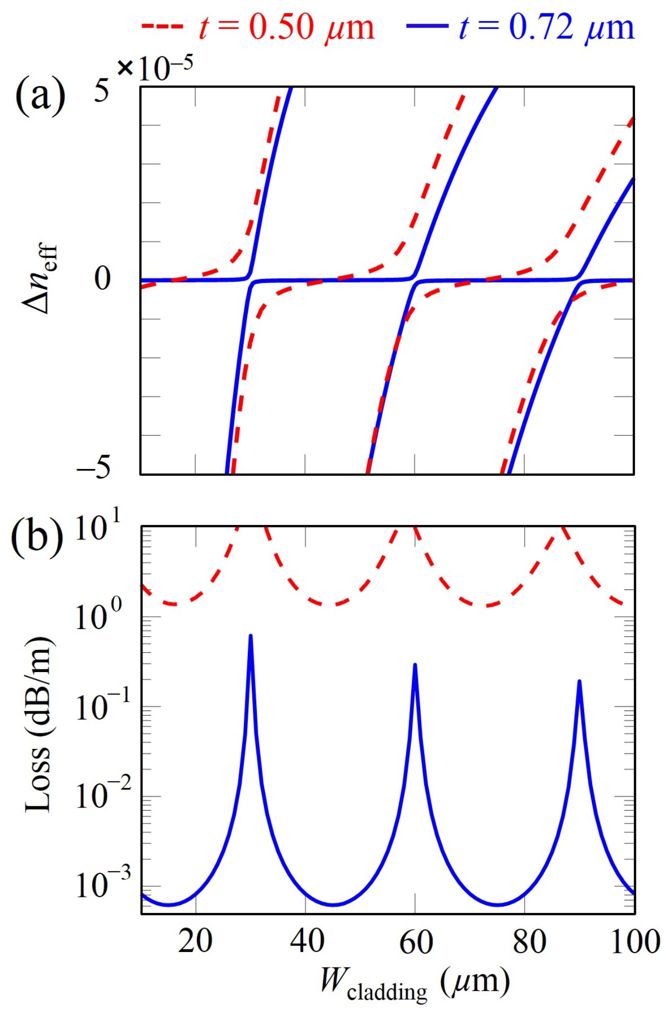

Figure 2.17: (a) Effective index difference, Δn_{eff}, between the effective indices of the modes in waveguide 1 and waveguide 3, as illustrated in Fig. 2.14. The condition $\Delta n_{\text{eff}} = 0$ indicates that there is a mismatch between the wavenumbers of the approximate core and cladding modes in the three-layer slab waveguide. (b) Leakage loss of the true modes in the three-layer slab waveguide.

We studied antiresonant reflection using a one-layer slab waveguide in section 2.1.1. We now revisit antiresonance in the case of a three-layer slab waveguide. Figure 2.17 shows Δn_{eff} and the loss as W_{cladding} varies for glass thicknesses of 0.50 μm and 0.72 μm. These glass thicknesses correspond respectively to resonance and to antiresonance, as shown in Fig. 2.3. We set $W_{\text{core}} = 30$ μm. The quantity Δn_{eff} is the difference between the effective indices in waveguide 1 and waveguide 3, as illustrated in Fig. 2.14. When $\Delta n_{\text{eff}} = 0$, the cladding layers do not affect the core layer, and the wavenumbers of the approximate core and cladding modes are mismatched. When the glass thickness t equals 0.50 μm, the resonance condition is fulfilled, and coupling is strong for a wide range of values of W_{cladding} around which the effective indices of the approximate modes cross. For this range of values, we find $\Delta n_{\text{eff}} \neq 0$, as shown by the red dashed curves. When the glass thickness t equals 0.72 μm, the antiresonance condition is fulfilled, and the range of values of W_{cladding} over which strong coupling occurs is greatly reduced, and the range of values for which $\Delta n_{\text{eff}} \neq 0$ is correspondingly reduced, as shown by the blue solid curves. Nonetheless, some wavenumber mismatch is needed. Figure 2.17(b) shows the leakage loss of the true fundamental modes in the three-layer slab waveguide, and we see that it always peaks when the effective indices of the approximate modes cross, but it is also consistently smaller when the antiresonance condition is met. Figure 2.18 shows the normalized electric field with $W_{\text{cladding}} = 45$ μm. We see that the field is higher in the cladding regions when the resonance condition is met, than it is when the antiresonance condition is met. That is consistent with the larger loss when the resonance condition is met. We conclude that while some wavenumber mismatch is needed between the approximate core and cladding modes, antiresonance plays a critical role in inhibiting coupling between these modes.

2.2.2 Negative Curvature Fiber

In this section, we describe inhibited coupling in negative curvature fibers. We show the cross section of a negative curvature fiber with six cladding tubes in Fig. 2.19. The core diameter, D_{core}, is 30 μm. The modes in a stand-alone annular core fiber, as shown in the red dotted box of Fig. 2.19, are approximate cladding modes in the negative curvature fiber.

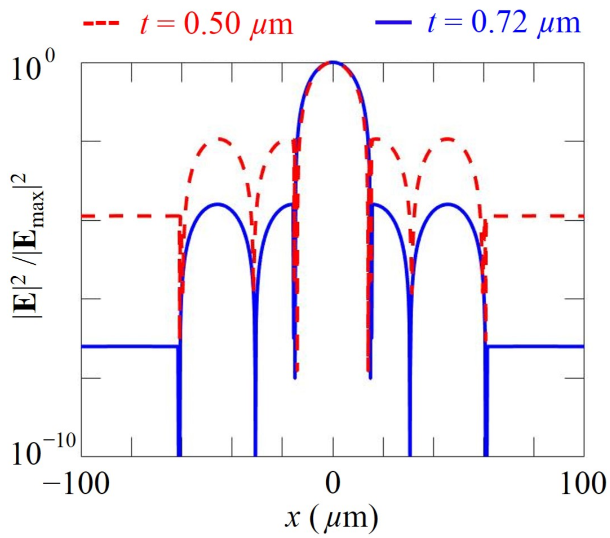

Figure 2.18: Normalized electric field intensity of the true modes in the three-slab waveguide with glass thicknesses of 0.50 μm and 0.72 μm and with $W_{\text{cladding}} = 45$ μm.

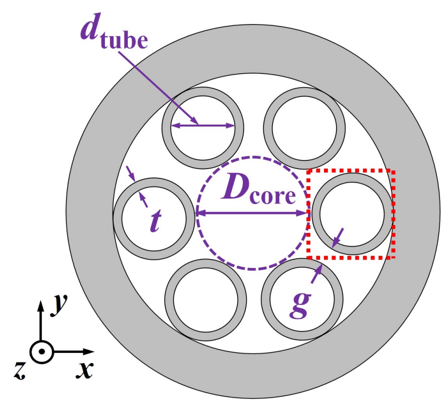

Figure 2.19: Cross section of a negative curvature fiber with six cladding tubes. The red dotted box shows the cross section of the stand-alone annular core fiber.

Figure 2.20(a) shows the effective index of the true modes in the negative curvature fiber as a function of the gap, g, or the diameter of the cladding tubes, d_{tube}. The thickness of the cladding tubes, t, is 0.72 μm, which corresponds to the antiresonance condition described in section 2.1.1. The blue solid curve and red solid curve show the effective indices of the true fundamental core mode and the true cladding tube mode, respectively. Note that core modes reside primarily in the central air core of the fiber, while tube modes reside primarily inside the cladding tubes. The effective indices of the true core mode and true cladding tube mode approach when the gap decreases and the tube diameter increases. The effective index of the approximate tube mode in the stand-alone annular core fiber is plotted using the green dashed curve, which matches the true tube mode in the negative curvature fiber. There is no avoided crossing visible. The true modes are almost entirely in the core or in the cladding. It is not obvious how to define an approximate core mode in this case.

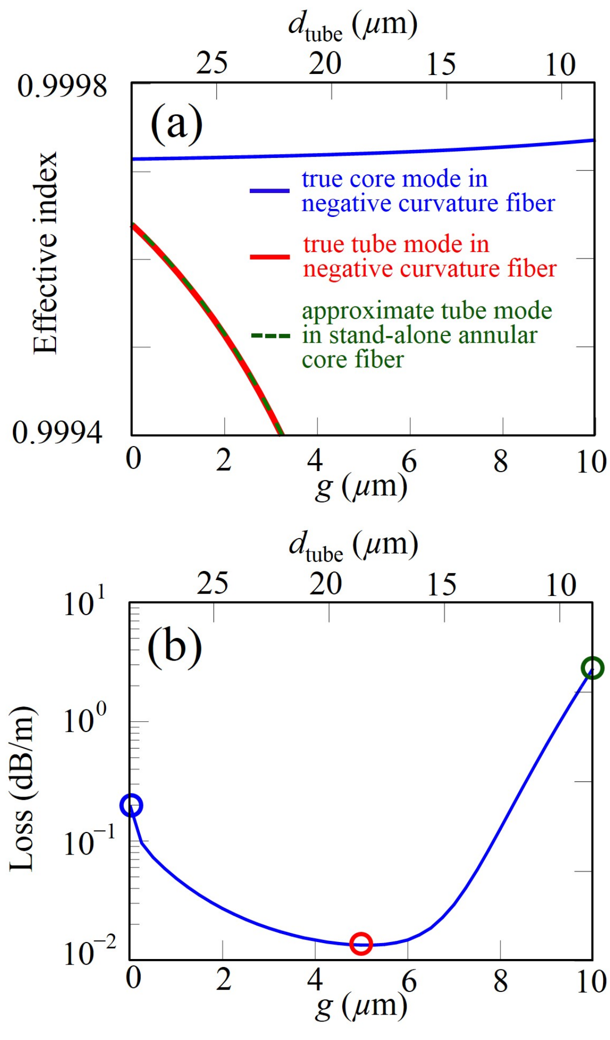

Figure 2.20: (a) Effective indices of the modes in the negative curvature fiber and the stand-alone annular core fiber. (b) Leakage loss of the fundamental core mode in the negative curvature fiber.

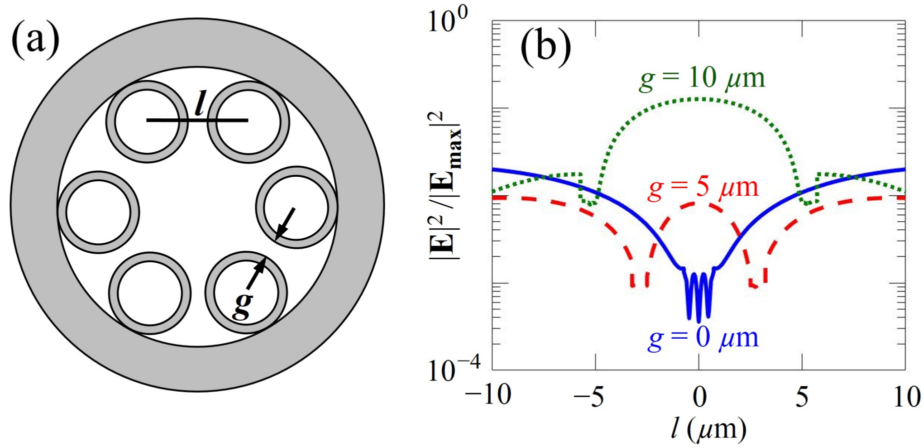

Figure 2.21: (a) Schematic illustration of a negative curvature fiber in which the black solid line connects the center of two adjacent cladding tubes. (b) The electric field intensity normalized to the electric field intensity in the center of the core at $g = 0\ \mu$m, 5 μm, and 10 μm, corresponding to the three circles in Fig. 2.20(b).

However, we already showed in section 2.1.3 that it corresponds to the mode of an annular core fiber in which the diameter is slightly larger than D_{core}. Figure 2.20(b) shows the loss of the true fundamental core mode in the negative curvature fiber. The loss is larger when there is no gap due to coupling to glass modes. The minimum loss occurs when the gap, g, is 5 μm. The loss is high with a larger tube diameter, which induces weak mode coupling between the fundamental core mode and the cladding tube modes [141]. It is analogous to the mode coupling in the three-layer slab waveguide that was described in section 2.2.1. However, there is no analogy to this gap in the slab waveguide that we considered in section 2.2.1.

The leakage loss increases as the gap increases from 5 μm to 10 μm due to leakage of the electric field through the air gap. Figures 2.21(b) shows the mode profile along the line connecting the center of two adjacent cladding tubes in the negative curvature fiber in Fig. 2.21(a) indicated by the black solid line. Similar plots have been presented in Ref. [57]. The mode intensity increases inside the gap when the gap increases from 0 to 10 μm. The increased leakage through the gap leads to an increased loss when the gap increases from 5 μm to 10 μm in Fig. 2.20(b).

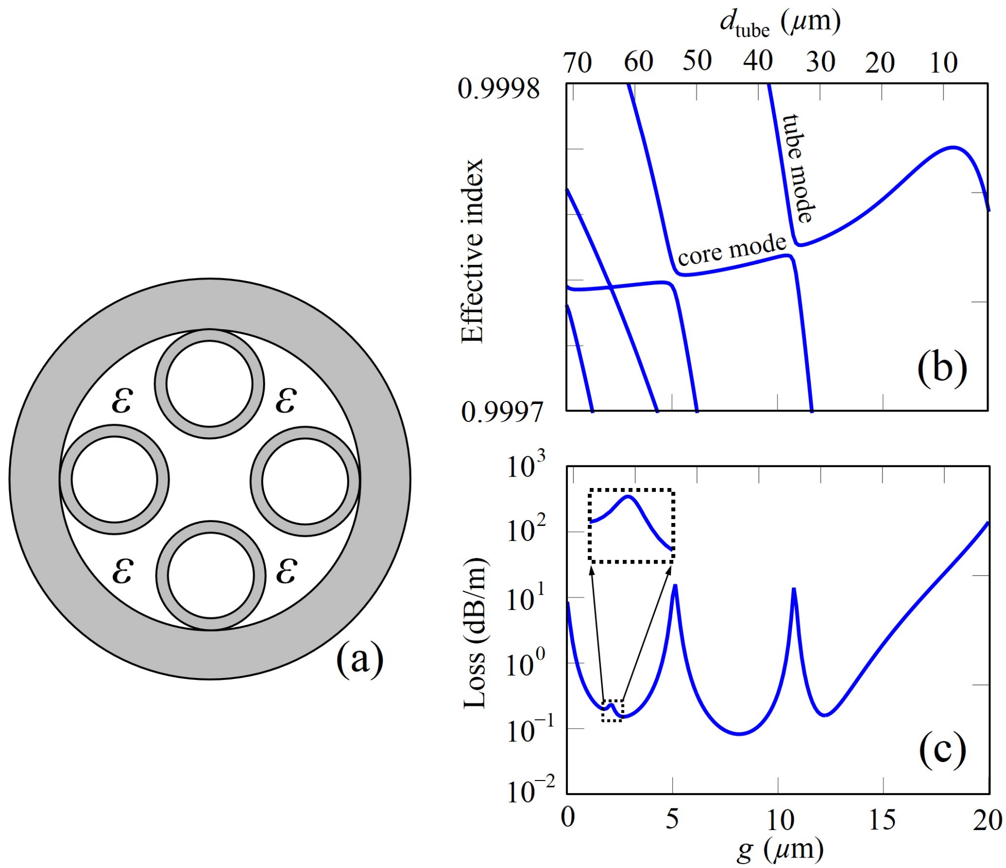

Figure 2.22: (a) Cross section of a negative curvature fiber with four cladding tubes. (b) Effective index of different modes and (c) leakage loss of the fundamental core mode in the negative curvature fiber with four cladding tubes. Inset shows a blow-up of the loss around $g = 2$ μm.

There is no complete avoided crossing between the fundamental core mode and the tube mode in negative curvature fibers using six cladding tubes. The tube diameter, d_{tube}, the core diameter, D_{core}, the glass wall thickness of the cladding tubes, t, the minimum gap distance between the cladding tubes, g, and the number of tubes, p, are related by the expression: $D_{\mathrm{core}} = (d_{\mathrm{tube}} + 2t + g)\sin(\pi/p) - (d_{\mathrm{tube}} + 2t)$ [58, 70, 141, 142, 150]. For a fiber with six cladding tubes ($p = 6$), the core diameter has the relation, $D_{\mathrm{core}} = d_{\mathrm{tube}} + 2t + 2g$. The core diameter of the fiber is always larger than the tube diameter by twice the glass wall thickness and the gap between the cladding tubes, so that the effective index of the fundamental core mode is always larger than that of the tube mode. Hence, only part of an avoided crossing is seen near $g = 0\ \mu$m in Fig. 2.20(a). We now examine negative curvature fibers with four cladding tubes. Figures 2.22(a) and 2.22(b) show a schematic illustration and mode effective index of a negative curvature fiber with four cladding tubes. We can see avoided crossings with gaps of 0 μm, 5 μm, or 11 μm. Note that the crossing [155, 156] at a gap of 2 μm occurs between the fundamental core mode and the cladding mode that is located in the interstices between the tubes and the outer glass ring, marked ε in Fig. 2.22(a). Figure 2.22(c) shows the leakage loss of the fundamental core mode. As expected, the loss of the fundamental core mode increases dramatically at the avoided crossing at a gap of 0 μm, 5 μm, or 11 μm. A small bump in the loss curve is observed at a gap of 2 μm due to a match of the effective index and a mode overlap between the fundamental core mode and the interstice mode in the region marked ε in Fig. 2.22(a) [156]. A blow-up of this small bump is shown by the inset in Fig. 2.22(c). Comparison between Figs. 2.20 and 2.22 shows that the coupling between the fundamental core mode and the tube mode is automatically avoided in negative curvature fibers using six cladding tubes with small air regions in the cladding outside the tubes. These small air regions in the cladding of the fibers that use six cladding tubes are helpful in inhibiting the coupling between the fundamental core mode and the cladding modes.

Figure 2.23 shows a magnification at the avoided crossing near a gap of 11 μm, as shown in Fig. 2.22(b). The two blue solid curves are effective indices of the two true modes in the negative curvature fibers. The corresponding mode field intensities at marked circles are shown in Fig. 2.24. We see avoided crossings that are analogous to the avoided crossings in the slab waveguide of section 2.2.1. While it is not obvious how to define an approximate core mode in this case, a study of the true modes shows that at gaps, g, that are far from the avoided crossings, the true modes reside almost entirely in the core or cladding, while at the avoided crossings, the true modes are

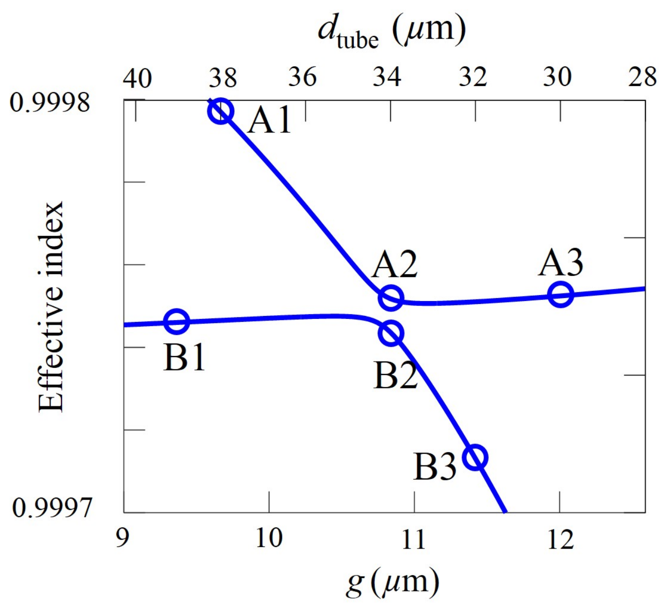

Figure 2.23: Effective index of the fundamental core mode near the avoided crossing at g = 11 μm.

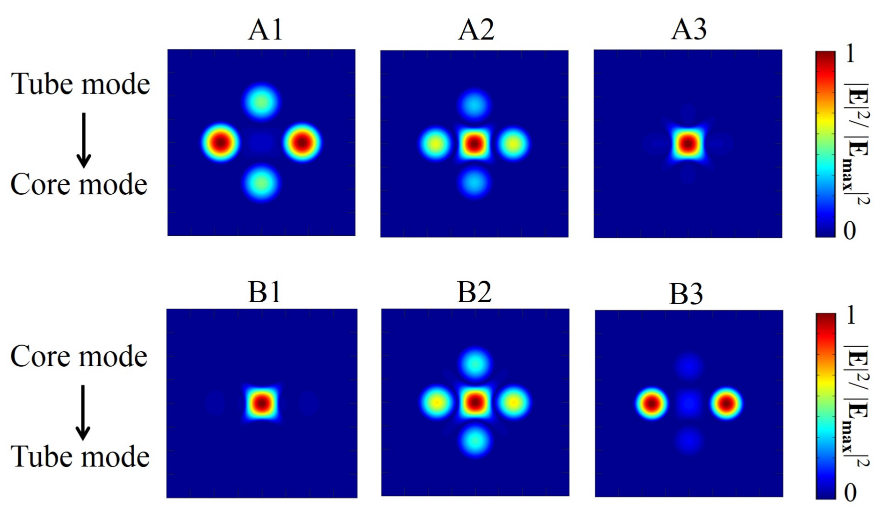

Figure 2.24: Normalized electric field intensity near the avoided crossing at g = 11 μm, corresponding to the circles in Fig. 2.23.

hybrid modes that reside in both the core and the cladding. In the neighborhood of the avoided crossing, the two true modes switch position between the core and the cladding tubes as the gap increases or the tube diameter decreases [136, 153].

While a negative curvature fiber with four cladding tubes is evidently easier to fabricate than a fiber with six or more cladding tubes, the existence of avoided crossings and the large loss that accompanies them make these fibers uninteresting in practice. This example illustrates once again that while antiresonance is necessary to inhibit coupling between core and cladding modes in negative curvature fibers, it is not sufficient.

2.3 Comparison of the Guiding Mechanisms

Hollow-core photonic bandgap fibers using a two-dimensional periodic cladding structure have attracted great interest due to their ability to transmit light power in the central air core [20, 21]. A bandgap implies that certain frequencies are forbidden. If the light frequency is in the frequency range of the bandgap, the periodic cladding structure can confine the light in the central air core [14, 15, 19]. In addition, the effective index of the fundamental core mode will reside in the range of the bandgap [14,15,19,140,157]. Hence, the leakage loss can be reduced by simply adding more rings to the bandgap structures [158]. Currently, the lowest transmission loss in photonic bandgap fibers that has been demonstrated is $1.2-1.8$ dB/km, which was achieved at around 1550 nm [19, 22, 44, 159, 160]. By taking advantage of inhibited coupling, the lowest losses that have currently been achieved in silica negative curvature fibers range from 7.7 dB/km to 50 dB/km at wavelengths between 0.75 μm to 3.39 μm [37, 50–53, 56–61]. It is difficult to arrange the antiresonant membranes to achieve coherent light reflection in the radial direction. Simply adding more tubes rings as is done in photonic bandgap fiber is not successful for negative curvature fibers due to the interconnecting struts or nodes [41, 43]. A double antiresonant structure or a nested structure might provide a solution to this issue [43, 65, 66, 85, 161].

In a bandgap fiber, light scattering in the bandgap region acts constructively to confine the light in the defect core. The nature of this guidance yields oscillatory light fields in the glass region [135, 162]. Surface roughness on the interface between the glass and air created during the fiber cooling process dominates the loss in bandgap fibers [22, 43, 163]. In negative curvature fibers, the antiresonant glass membranes act as a mirror to reflect light back into the central core region. The outgoing and reflected light cancel out near the glass at the boundary of the core. Additionally, there is a wavenumber mismatch between the core and glass modes. As a consequence, coupling between the core mode and glass modes is inhibited, yielding a very low power ratio in the glass region of less than 0.01% [60, 164]. Hence, surface scattering in negative curvature fibers can be possibly lower than in bandgap fibers. For the same reason, the power damage threshold is also expected to be higher in negative curvature fibers [165].

CHAPTER THREE

Comparison of Loss in Silica and Chalcogenide Negative Curvature Fibers

This chapter published as [142]: C. Wei, J. Hu, and C. R. Menyuk, "Comparison of loss in silica and chalcogenide negative curvature fibers as the wavelength varies," Front. Phys. **4**, 30 (2016).

In this chapter, we computationally study fiber loss in negative curvature fibers made with silica, As_2S_3 chalcogenide, and As_2Se_3 chalcogenide glasses with a fixed core-diameter-to-wavelength ratio of 30. We consider both simple and nested geometries as the transmission wavelength varies. At wavelengths shorter than 4.5 μm, silica negative curvature fibers have a loss that is around or below 10^{-1} dB/m and are preferable to chalcogenide fibers. At wavelengths longer than 4.5 μm, it is preferable to use As_2S_3 chalcogenide or As_2Se_3 chalcogenide negative curvature fibers since their loss is one or more orders of magnitude lower than the loss of silica negative curvature fibers. With nested negative curvature fibers, chalcogenide fibers have losses that are lower than those of silica fibers at wavelengths larger than 2 μm. However, it is still preferable to use silica nested negative curvature fibers at wavelengths less than 4.5 μm and with a loss around or lower than 10^{-1} dB/m due to the fabrication advantages of silica fibers.

3.1 Introduction

Hollow-core photonic crystal fibers can confine light in the air core, leading to a low transmission loss, a low nonlinearity, and a high damage threshold [15,20,45,140,166]. Hollow-core photonic bandgap fibers use a periodic structure in the fiber cladding that creates a bandgap or a forbidden gap, which confines the light at the forbidden frequencies to the central air core [19]. Silica bandgap fibers have been demonstrated to transmit light up to 2.2 μm [19, 167]. Development of hollow-core fibers using non-silica glasses, such as chalcogenide, has been hampered by fabrication difficulties. Recently, low-loss transmission has been observed in a new kind of hollow-core fiber, called negative curvature fiber [43, 47–51, 67, 70, 119, 150]. Negative curvature implies that the surface normal to the core boundary is oppositely directed from the core. Since no bandgap is used, there is no requirement for a periodic cladding structure. The relative simplicity of the negative curvature structure could enable the fabrication of fiber devices for mid-IR applications using non-silica glasses, such as chalcogenide [78, 79]. Using chalcogenide negative curvature fibers, the delivery of mid-infrared radiation has been successfully demonstrated for a CO_2 laser at a wavelength of 10.6 μm [55].

An important reason for the low loss in negative curvature fibers relative to hollow-core bandgap fibers with positive curvature is the relatively low overlap between the mode field and the glass [48,51]. In the bandgap fiber, light scattering in the bandgap region acts constructively to confine the light in the defect core. The nature of this guidance yields oscillatory light fields in the glass regions [135, 162]. In negative curvature fibers, the antiresonant glass membranes act as a mirror to reflect the light back to the central core region. The outgoing and reflected light cancel out around the glass regions and yield a very low power ratio in the glass regions of less than 0.01% [58, 164]. With a low overlap, the impact of the material loss is decreased. Silica has a high material loss at wavelengths above 2 μm [51, 168]. The low overlap between the mode field and glass will enable low loss transmission in silica negative curvature fibers for wavelengths longer than 2 μm. The low loss in negative curvature fibers makes silica a competitive choice of material for mid-IR applications. Transmission losses of 0.05 dB/m and 0.085 dB/m have been realized at 3.4 μm and 4.0 μm respectively in silica negative curvature fibers [51,52]. To date, it has not been determined how far out in wavelength it is possible to use silica and still achieve losses that are competitive or better than what can be achieved using chalcogenide or other glasses, with low material losses in the mid-IR. This chapter addresses this question for chalcogenide glasses. We focus on chalcogenide glasses because the material losses of other mid-IR glasses, such as ZBLAN and Tellurite, are higher than chalcogenide glass beyond 4.5 μm [75, 169–171]. Comparing the losses of silica glass and chalcogenide glass fibers as a function of wavelength in negative curvature fibers will guide the choice of which type of fiber to use for mid-IR applications. In this chapter, we compare the performance of negative curvature fibers that are made with silica glass to those that are made with chalcogenide glass.

In hollow-core negative curvature fibers, the total fiber loss is influenced by both the mode confinement loss and material loss. In this chapter, we calculate the total fiber loss in negative curvature fibers with both simple and nested geometries. We analyze the impact from the confinement and the material loss on the total fiber loss in negative curvature fibers, comparing fibers that are made with silica, As_2S_3 chalcogenide, and As_2Se_3 chalcogenide glasses. We find that, using a simple negative curvature fiber with a fixed core diameter to wavelength ratio of 30, a fiber made with silica glass has comparable loss to fibers made with As_2S_3 and As_2Se_3 chalcogenide glasses for wavelengths shorter than 4.5 μm. Hence, it is preferable to use silica glass because of the relatively simple fabrication process for fibers made from silica glass. It is preferable to use negative curvature fibers made with As_2S_3 and As_2Se_3 chalcogenide glasses when the wavelength is longer than 4.5 μm, since the losses are more than one order of magnitude lower than the loss in negative curvature fibers that are made with silica glass.

The rest of the chapter is organized as follows: section 3.2 presents the antiresonance condition and the confinement loss as a function of wavelength and refractive index. We analyze the fiber loss for silica glass fibers in section 3.3 and for As_2S_3 and As_2Se_3 chalcogenide glass fibers in section 3.4. section 3.5 shows a direct comparison among fibers made with different glasses. Conclusions are given in section 3.6.

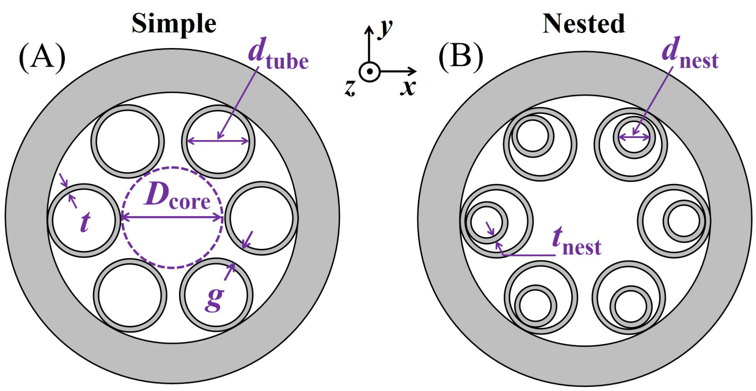

Figure 3.1. Cross sections of (A) a simple and (B) a nested negative curvature fiber.

3.2 Antiresonance Condition and Confinement Loss

Figure 3.1(A) shows a schematic illustration of a simple negative curvature fiber. The gray regions represent glass, and the white regions represent air. The outer tube diameter, d_{tube}, the core diameter, D_{core}, the tube wall thickness, t, and the minimum gap between the cladding tubes, g, are related by the expression:$D_{\text{core}} = (d_{\text{tube}} + 2t + g)/\sin(\pi/6) - (d_{\text{tube}} + 2t)$. Figure 3.1(B) shows a schematic illustration of a nested negative curvature fiber, which has an additional nested tube with a tube diameter, d_{nest}, and a wall thickness, t_{nest}, inside each of the major tube. The total fiber loss is obtained from the imaginary part of the propagation constant,

$$\text{Loss} = \frac{40\pi}{\ln(10)} \frac{\text{Im}(n_{\text{eff}})}{\lambda}, \tag{3.1}$$

where λ is wavelength [135, 139]. In this chapter, we use total fiber loss to describe the mode leakage, which includes the mode confinement loss and the material loss due to glass light absorption.

The tube thickness t for both the outer tubes and nested tubes that is required by the antiresonance condition is given by

$$t = (m - 0.5)\lambda/[2(n_1^2 - n_0^2)^{1/2}], \tag{3.2}$$

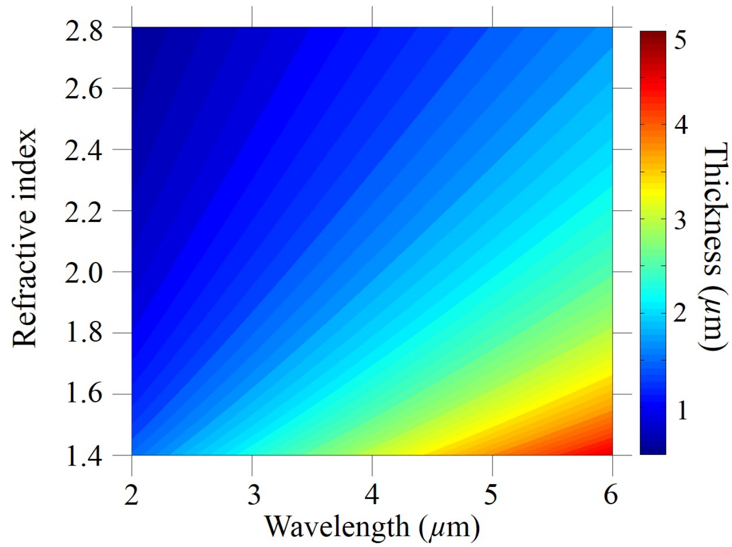

Figure 3.2: Contour plot of the tube thicknesses that satisfy the antiresonance condition, $t = (m - 0.5)\lambda/[2(n_1^2 - n_0^2)^{1/2}]$, where $m = 2$.

where n_1 and n_0 are the real part of refractive indices of the glass and air, λ is the light wavelength, and m is the antiresonance order [32,34]. We use the second antiresonance transmission band for which $m = 2$. We ran additional simulations on the first and third transmission bands, and we obtained similar losses to the loss that we obtained using the second antiresonance transmission band [141]. A higher-order antiresonance implies thicker tube wall thickness, especially for shorter wavelengths, which makes fabrication easier; however, the analysis and conclusions in this chapter still hold if we use the first or third transmission band. In Fig. 3.2, we use Eq. 3.2 to plot the antiresonant tube thickness as a function of wavelength, λ, and the refractive index, n_1. Figure 3.3 shows the confinement loss of simple and nested negative curvature fibers that are calculated using the antiresonant tube thickness as a function of the wavelength and the refractive index. We assume no material loss in this section, in order to focus on the confinement loss. The core diameter, D_{core}, and the minimum gap between tubes, g, are fixed at 60 μm and 10 μm, respectively. The ratio of the diameter of the nested tube to the diameter of the outer tube is fixed at, $d_{\mathrm{nest}}/d_{\mathrm{tube}}$

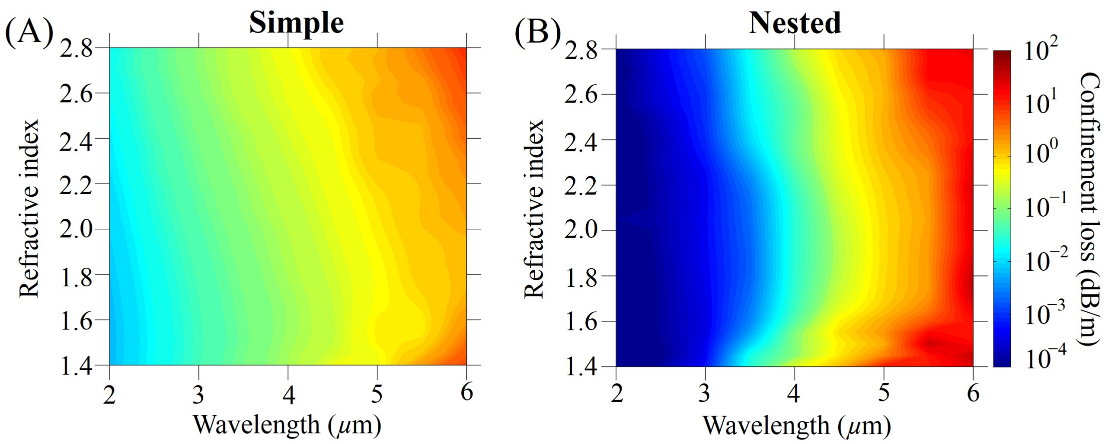

Figure 3.3: Contour plot of fiber loss in (A) simple and (B) nested negative curvature fibers. No material loss is included.

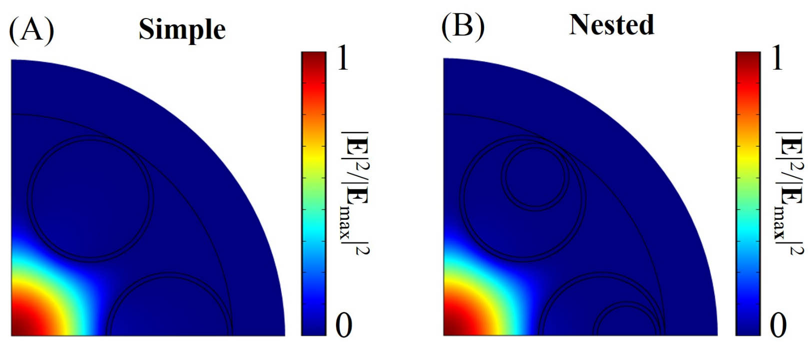

Figure 3.4: Normalized mode intensity at a wavelength of 2.00 μm in both (A) simple and (B) nested negative curvature fibers.

= 0.5. We see that the confinement loss increases as the wavelength increases in both simple and nested fibers, which implies that the loss is mainly determined by the wavelength, and the index of refraction has a relatively low impact on the fiber loss.

The normalized mode intensity in both simple and nested negative curvature fibers is shown in Fig. 3.4. Only a quarter of the geometry is used in modeling the fiber because of the symmetry of the fundamental modes [139]. The refractive index and wavelength are 1.45 and 2.00 μm, respectively. We use antiresonant tube wall thicknesses that are given by Eq. 3.2. In both simple and nested negative curvature fibers, the mode field is well-confined in the core.

3.3 Silica Glass

In this section, we study fiber loss in negative curvature fibers made with silica. Keeping the geometry of the fiber fixed, as shown in Fig. 3.1, we calculate the total fiber loss as a function of both the material loss and the wavelength. The material loss increases from 10^{-1} dB/m to 10^{5} dB/m and the wavelength increases from 2 μm to 6 μm. The fundamental mode will change as a function of these two parameters, which will in turn change the confinement loss. The total fiber loss is a combination of the material loss and the confinement loss. Since the material loss is not an arbitrary parameter, the value of this plot requires some explanation. As the material loss increases at a fixed wavelength, the total fiber loss will initially be dominated by the confinement loss and will be almost constant and then later will be dominated by the material loss and change proportional to the material loss. By plotting the actually material loss on a contour plot of the total fiber loss as a function of both the material loss and the wavelength, it is possible to immediately determine by visual inspection whether material loss or confinement loss dominates the total fiber loss.

We show the results of this procedure for silica fiber in Fig. 3.5. We denote the region in the parameter space in which confinement loss dominates as region I and the region in which material loss dominates as region II. The two regions are separated by a black dashed curve that is drawn through the points of maximum curvature in the contour plot [172]. We have set the refractive index $n_1 = 1.45$, and we do not include the small effect of dispersion. As noted previously, we use the second transmission band, $m = 2$, as shown in Eq. 3.2. We set the core diameter $D_{\mathrm{core}} = 60$ μm and we set the minimum gap between tubes $g = 10$ μm. Comparing Figs. 3.5(A) and 3.5(B), we first observe that the total fiber loss is smaller below 3.5 μm for the nested fiber

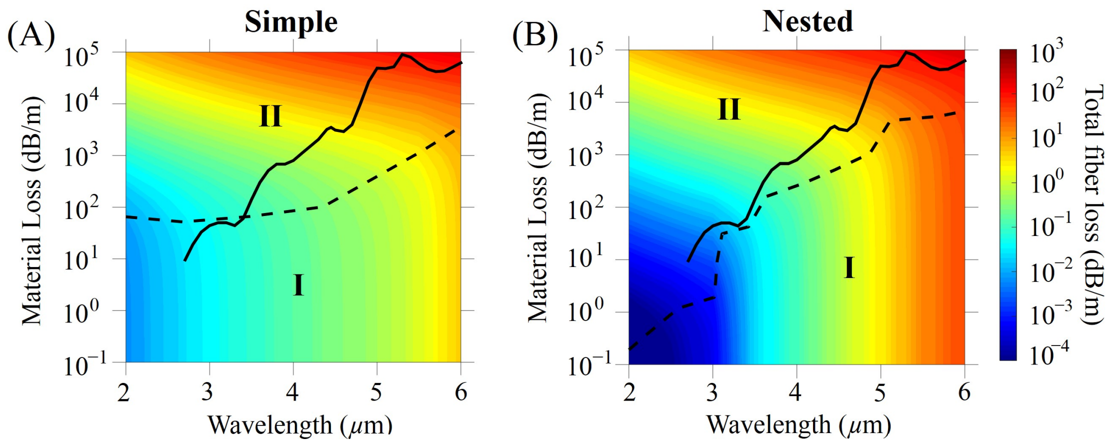

Figure 3.5: Contour plot of fiber loss in (A) simple and (B) nested negative curvature fibers made with silica glass. The black solid curves show the material loss of silica glass. The black dashed curves separate regions I and II.

than it is for the simple fiber. The reason is that the nested tubes provide a second antiresonant layer and enhance the confinement. However, above 4.5 μm, the loss in the nested fiber is larger than in the simple fiber. The reason is that the diameters of the nested tubes are too small for them to function as antiresonant layers, and they add to the material loss and the total fiber loss. For example, when $\lambda = 5$ μm, the inner and outer diameter (d_{in} and d_{out}) of the nested tubes, 16.4 μm and 23.6 μm, are only a few times the wavelength. To confirm this point, we show the fiber loss as a function of the diameter of the nested tube, as shown in Fig. 3.6. We fixed $D_{\text{core}} = 60$ μm, $g = 10$ μm, $\lambda = 2$ μm, and $n_1 = 1.45$. We also set the material loss equal to zero. We can see that, when the diameter of the nested tube is less than four to five times the wavelength, the fiber confinement loss increases significantly.

We also plot the material loss of silica [51, 168] using the black solid curve in Figs. 3.5(A) and 3.5(B). The high loss bumps in the black solid curve are due to overtones and combination vibrations from the absorption bands at longer wavelengths of 8.9 μm, 12.5 μm, and 21.5 μm [168]. The corresponding simple and nested fiber losses located at the material loss curves are extracted from Figs. 3.5(A) and 3.5(B)

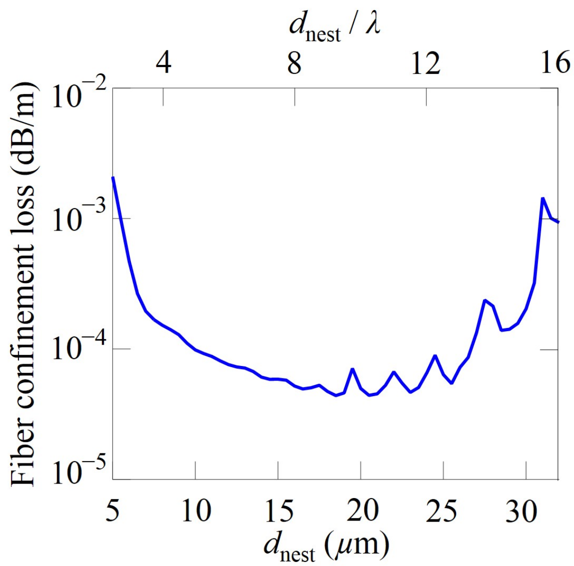

Figure 3.6: Fiber confinement loss as a function of diameter of the nested tube. No material loss is included. We set $\lambda = 2$ μm.

and plotted in Fig. 3.7 using red solid and red dashed curves, respectively. Since most of the mode propagates in air, the bulk material loss is several orders of magnitude higher than the total fiber loss. We also observe that the total fiber loss increases with wavelength. It is lower in the nested fiber than in the simple fiber when the wavelength is less than 3.5 μm. However, when the wavelength is larger than 3.5 μm, nested tubes do not lower the total fiber loss, and the losses indicated by the red solid curve and red dashed curve are almost the same.

The core diameter is fixed at 60 μm in Figs. 3.5(A) and 3.5(B). At longer wavelengths, it is better to use a larger core in order to lower the fiber loss. Negative curvature fibers have been fabricated using a ratio of the core diameter to the wavelength that varies from 31 to 36 [49–51, 69]. We then study negative curvature fibers with a fixed ratio of the core diameter to the wavelength, D_{core} / $\lambda = 30$. We can directly extract the total loss from the data in Fig. 3.5 by using the constraint D_{core} / $\lambda = 30$ and the scale invariance of Maxwell's equations [3]. As the wavelength

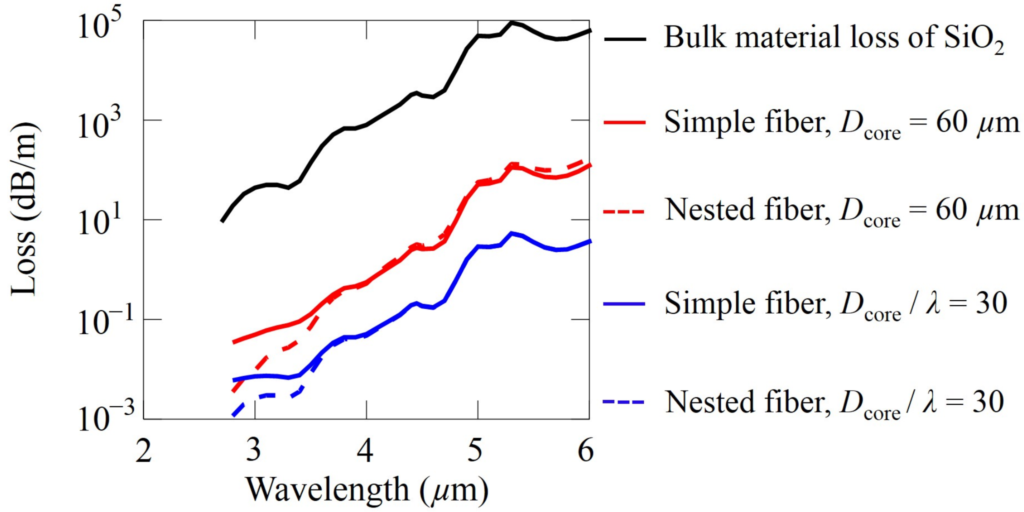

Figure 3.7: Fiber loss of simple and nested negative curvature fibers made with silica glass.

and fiber geometry increase proportionally, the total fiber loss is determined by the material loss of the glass. The corresponding total fiber loss of simple and nested fibers are shown as blue solid and dashed curves in Fig. 3.7, respectively. When the wavelength is larger than 3.5 μm, the bulk material loss is higher than 10^2 dB/m in region II, and the total fiber losses of the simple and nested fibers are similar and dominated by the material loss. When the wavelength is less than 3.5 μm, the nested fiber has a low confinement loss with an additional antiresonant layer. Hence, the blue dashed curve for the total fiber loss in the nested fiber has a similar shape as the curve for the bulk material loss, as shown in Fig. 3.7.

Overall, with a fixed ratio of $D_{\rm core}$ / $\lambda = 30$, the simple and nested negative curvature fibers can be used for transmission with a loss around or less than 10^{-1} dB/m up to a wavelength of around 4.5 μm.

3.4 Chalcogenide Glasses

In this section, we carry out the same loss analysis on negative curvature fibers made with As_2S_3 and As_2Se_3 chalcogenide glasses as what we carried out in section

3.3 for silica glass. For As_2S_3, we have $n_1 = 2.4$ and for As_2Se_3, $n_1 = 2.8$. The small dispersive contribution is again ignored. The tube wall thickness using Eq. 3.2 in the second antiresonance transmission band $m = 2$ is again used. Figures 3.8(A) and 3.8(C) show the total fiber loss in simple and nested negative curvature fibers, respectively, for As_2S_3, and Figs. 3.8(B) and 3.8(D) show the total fiber loss in simple and nested negative curvature fibers for As_2Se_3. We use a wavelength range of 2 μm to 6 μm in Fig. 3.8. We note however that As_2Se_3 has a broader transmission window that goes out approximately to 10 μm [173].

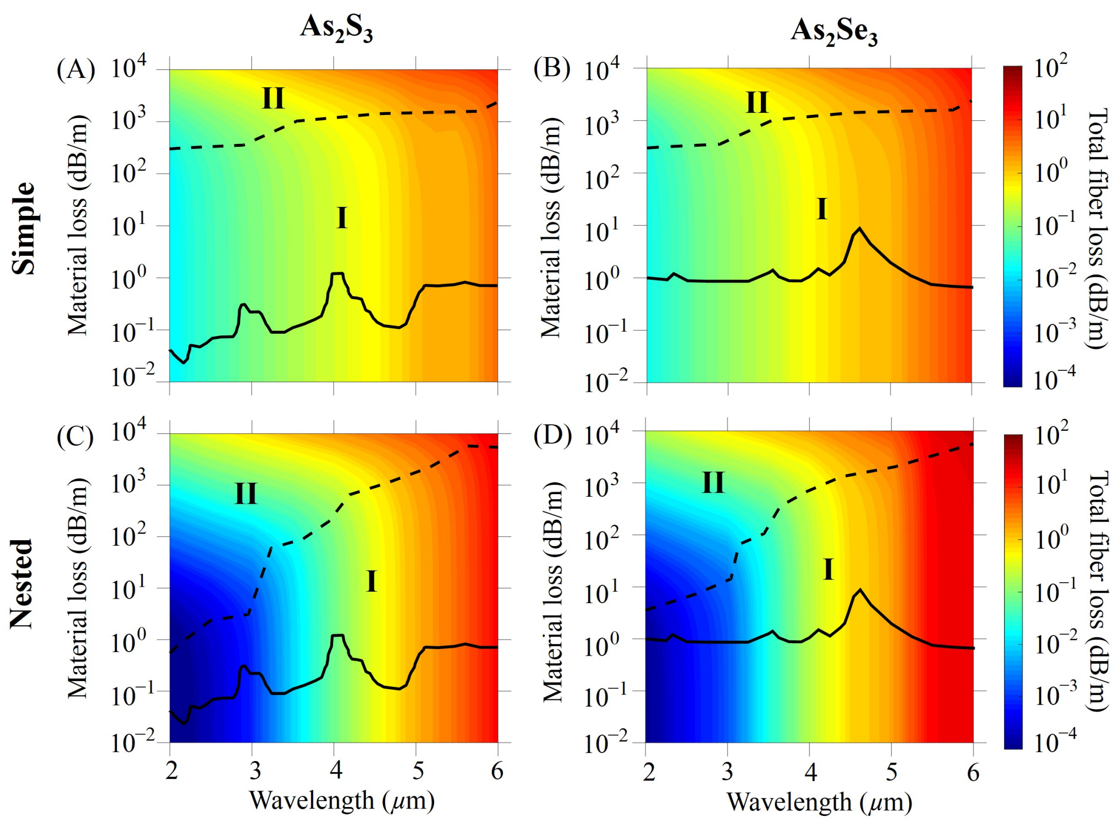

Figure 3.8: Contour plot of fiber loss in (A) simple and (C) nested negative curvature fibers made with As_2S_3 chalcogenide glass. Contour plot of fiber loss in (B) simple and (D) nested negative curvature fibers made with As_2Se_3 chalcogenide glass. The black solid curves show the material loss of chalcogenide glass. The black dashed curves separate regions I and II.

The bulk material loss is shown using black solid curves [173,174]. In Figs. 3.8(A) and 3.8(C), the peaks in the material loss curve of As_2S_3 at wavelengths of 2.8 μm, 2.92 μm, and 4.05 μm are due to the absorption bands of impurities of H_2O, OH, and SH, respectively [175]. In Figs. 3.8(B) and 3.8(D), the peak in the material loss curve of As_2Se_3 at a wavelength of 4.57 μm is due to the H-Se stretching vibration [173, 176]. The three minor peaks at wavelengths of 2.32 μm, 3.55 μm, and 4.15 μm are attributed to the combination and first overtone of the H-Se stretching vibration at 4.57 μm [173,176]. In Fig. 3.8, just as in the case of silica fibers, two regions, denoted I and II, are separated by a black dashed curve in which confinement loss and material loss dominate, respectively. In contrast to silica fibers, we see that confinement loss dominates the total fiber loss at all wavelengths.

With a fixed $D_{\text{core}} = 60$ μm, the corresponding simple and nested fiber loss located at the material loss curves are extracted from Figs. 3.8(A) and 3.8(C) and plotted in Fig. 3.9(A) using red solid and red dashed curves, respectively. The total fiber loss increases almost linearly and has no similarity with the shape of the material loss curve of As_2S_3, which is consistent with the observation that the total fiber loss is dominated by the confinement loss. The total fiber loss is lower in the nested fiber than in the simple fiber when the wavelength is less than 4.5 μm. The total fiber loss is a little higher in the nested fiber than in the simple fiber when the wavelength is larger than 4.5 μm, because, just as the case in silica fibers, the diameter of the nested tube is too small for it to act effectively as an antiresonant layer.

When the ratio of the core diameter to the wavelength, D_{core} / $\lambda = 30$, the blue solid and dashed curves show respectively the corresponding total fiber loss of simple and nested As_2S_3 fibers in Fig. 3.9(A). When the wavelength increases from 2 μm to 6 μm, the total fiber loss decreases slightly in the simple fiber, as shown by the blue solid curve. In this case, the material loss of As_2S_3 chalcogenide glass is in the region I and does not contribute much to the total fiber loss. The imaginary part

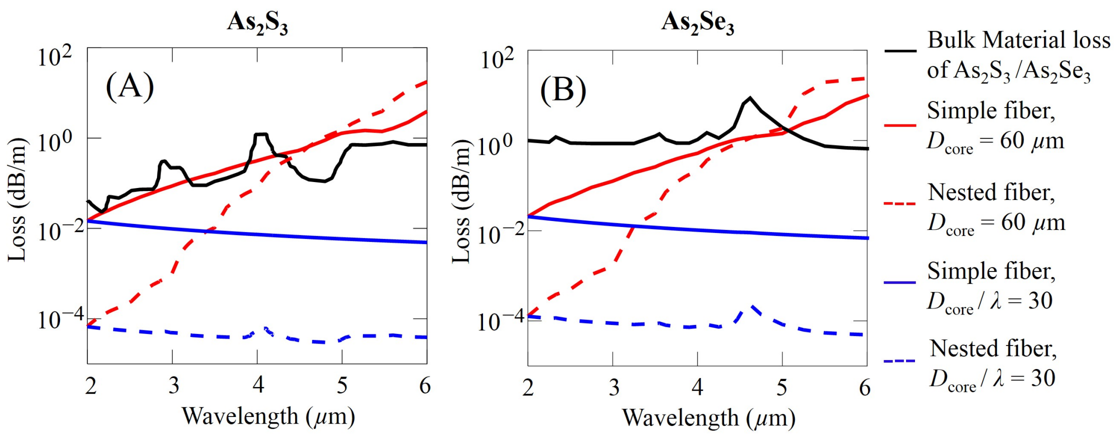

Figure 3.9: Fiber loss of simple and nested negative curvature fibers made with (A) As_2S_3 chalcogenide, and (B) As_2Se_3 chalcogenide glasses.

of the effective index remains almost the same at different wavelengths due to the scale invariance of Maxwell's equations [3]. The total fiber loss is then slightly lower for a longer wavelength according to Eq. 3.1. On the other hand, the blue dashed curve is two orders of magnitude lower than the blue solid curve, which shows that the nested fiber has a much lower confinement loss due to the additional antiresonant layers. In Fig. 3.9(B), we show the figure for As_2Se_3 that corresponds to Fig. 3.9(A). The results are similar to what we observe for As_2S_3 fibers. With $D_{\mathrm{core}} = 60$ μm, the total loss is dominated by confinement loss, and nested fibers have a slightly higher loss than simple fibers beyond 5 μm. When D_{core} / $\lambda = 30$, total fiber loss decreases slightly as wavelength increases, and the material loss does not contribute much to the total fiber loss.

3.5 Comparison and Analysis

In this section, we will compare the performance of negative curvature fibers made with silica and chalcogenide glasses. Figures 3.10(A) and 3.10(B) show a comparison of simple and nested negative curvature fibers made with silica, As_2S_3 chalcogenide, and As_2Se_3 chalcogenide glasses between a wavelength range of 2 μm and 6 μm.

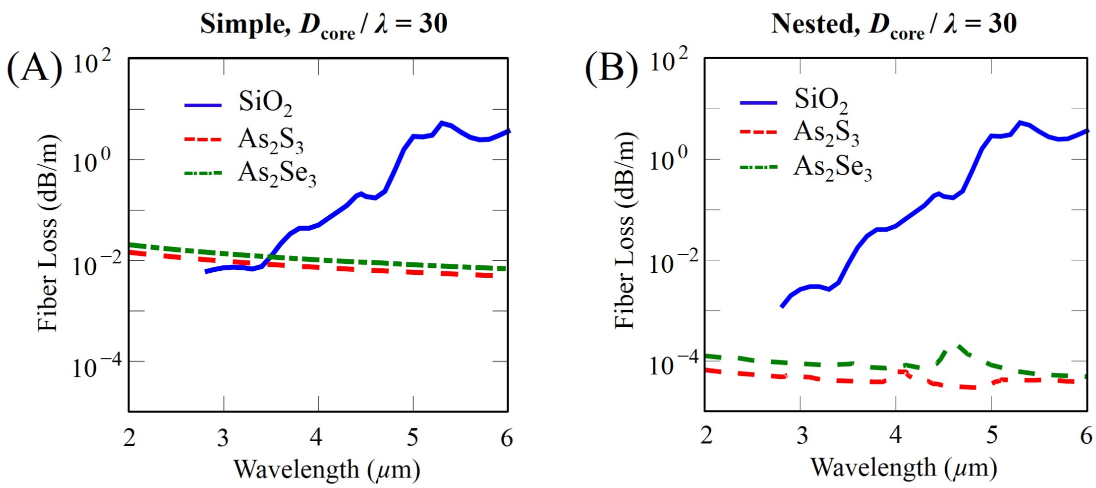

Figure 3.10: Fiber loss of (A) simple and (B) nested negative curvature fibers made with silica, As_2S_3 chalcogenide, and As_2Se_3 chalcogenide glasses with D_{core} / $\lambda = 30$.

The ratio of the core diameter to the wavelength is fixed at D_{core} / $\lambda = 30$. In simple negative curvature fibers made with silica, the fiber loss increases after 3.5 μm due to the material loss. For wavelengths shorter than 4.5 μm, the loss of silica negative curvature fiber is around or less than 10^{-1} dB/m. These fibers are easier to fabricate than chalcogenide fibers and should be used at wavelengths below 4.5 μm. At wavelengths that are longer than 4.5 μm, As_2S_3 chalcogenide or As_2Se_3 chalcogenide fibers are preferred because their loss is at least one order of magnitude less than that of silica fibers. In nested negative curvature fibers, fibers made with chalcogenide glasses have a loss much lower than that of fibers made with silica. However, due to the fabrication advantages, it is still preferable to use silica fibers at wavelengths below 4.5 μm.

Figures 3.11(A) and 3.11(B) show a comparison of simple and nested negative curvature fibers made with silica, and chalcogenide glasses with a fixed core diameter of 60 μm between a wavelength range of 2 μm and 6 μm. We arrive again at the same conclusion as when we fixed D_{core} / $\lambda = 30$. It is preferable to use silica glass below 4.5 μm, and it is preferable to use chalcogenide glasses above this wavelength.

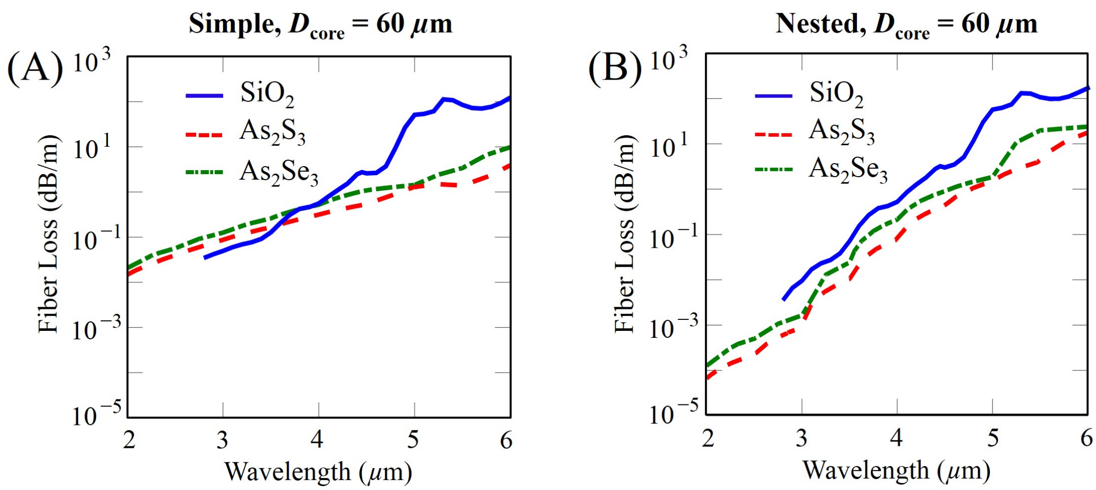

Figure 3.11: Fiber loss of (A) simple and (B) nested negative curvature fibers made with silica, As_2S_3 chalcogenide, and As_2Se_3 chalcogenide glasses with a fixed core diameter of $D_{\text{core}} = 60$ μm.

3.6 Conclusion

We computationally study the fiber loss in simple and nested negative curvature fibers made with silica, As_2S_3 chalcogenide, and As_2Se_3 chalcogenide glasses. There is no significant difference in loss for fibers using materials with different refractive indices if no material loss is considered. With a fixed core diameter to wavelength ratio of D_{core} / λ = 30 or a fixed core diameter D_{core} = 60 μm, silica negative curvature fibers should be used for either simple or nested negative curvature fibers at wavelengths that are shorter than 4.5 μm. The achievable total fiber loss is around 10^{-1} dB/m or less in this wavelength range, and silica fibers are easier to fabricate. For wavelengths that are longer than 4.5 μm, As_2S_3 or As_2Se_3 chalcogenide negative curvature fibers should be used because their total fiber loss is one or more orders of magnitude lower than the total fiber loss in silica fibers. In nested negative curvature fibers, fibers made with chalcogenide glasses have losses that are lower than the losses in fibers made with silica at wavelengths that are longer than 2 μm. However, silica fibers should still be used at wavelengths less than 4.5 μm since their total fiber loss is still around or less than 10^{-1} dB/m, and they are easier to fabricate. Nested tubes do not decrease the total fiber loss when the diameters of the nested tubes are less than 4–5 times the wavelength because the nested tubes no longer act as an antiresonant layer. This comparative study for negative curvature fibers shows that it is advantageous to use silica glass in negative curvature fibers below 4.5 μm, and it is advantageous to use chalcogenide glasses at longer wavelengths.

CHAPTER FOUR

Impact of Cladding Tubes in Chalcogenide Negative Curvature Fibers

This chapter published as [141]: C. Wei, C. R. Menyuk, and J. Hu, "Impact of cladding tubes in chalcogenide negative curvature fibers," IEEE Photon. J. **8**, 2200509 (2016).

In this chapter, we computationally study the leakage loss and bandwidth in chalcogenide negative curvature fibers. The leakage loss is decreased by a factor of 19 and the operating bandwidth is almost doubled when the optimal gap between cladding tubes is used in negative curvature fibers with 6 tubes. There is a wide range of the gaps between 5 μm and 40 μm, which gives a leakage loss lower than 0.04 dB/m and a wide transmission bandwidth of 1.1 μm. The optimal gap in a fiber with 6 cladding tubes is 3 times as large as the optimal gap in fibers with 8 or 10 cladding tubes. A larger gap is needed in a fiber with 6 cladding tubes to remove the weak coupling between the central core mode and the tube modes. This design of the chalcogenide negative curvature fibers using a wide range of gaps will lead to successful fiber devices with a low loss and a wide bandwidth for mid-IR transmission.

4.1 Introduction

Negative curvature fibers consisting of a ring of tubes, have yielded promising results with low transmission loss [49,50,64–66,70,80,83,114,150,177–179]. It is found that a gap between cladding tubes can effectively decrease the leakage loss in negative curvature fibers [43, 51, 69]. When the tubes touch, localized nodes are created, and modes exist in the localized node area. A separation between the cladding tubes removes the additional resonances in the transmission bands [43,51]. However, further increase in the separation between the cladding tubes decreases the mode confinement in the air core. There is an optimal gap range between these two limits. In addition, the surface tension forces straighten the tube walls in the fiber drawing process [43]. Hence, it is difficult to obtain touching circular tubes to produce a negative curvature core boundary. In a negative curvature fiber whose cladding tubes do not touch, it is possible to maintain the circular shape of the tubes even at a high drawing temperature [43]. Hence, fibers with a gap between tubes are expected easier to fabricate, since surface tension would naturally assist in maintaining the circular shape of the tubes.

Sources and transmission of mid-infrared light are important for applications in biosensing, environmental monitoring, homeland security, and medical diagnostics [180]. In this chapter, we computationally study the leakage loss [135] and bandwidth in chalcogenide negative curvature fibers with 6 cladding tubes at a wavelength of 5 μm. We focus on 5 μm because development of quantum cascade lasers has shown great potential for the generation of mid-infrared emission around 5 μm with a wall-plug efficiency of 50% and a watt-level power output [181]. We show that the leakage loss decreases and bandwidth increases with an appropriate gap between cladding tubes. Using a fiber with a tube wall thickness of 1.8 μm and a gap range between 5 μm and 40 μm, a low transmission loss of under 0.04 dB/m and a bandwidth of 1.1 μm can be achieved simultaneously for chalcogenide negative curvature fibers with 6 cladding tubes. We also compare the optimal gaps for fibers with 6, 8, and 10 cladding tubes. We find that the optimal gap in a fiber with 6 cladding tubes is 3 times as large as the optimal gap in fibers with 8 or 10 cladding tubes. The reason is that there is a weak coupling between the central core mode and the tube modes in a fiber with 6 cladding tubes. A larger gap is needed to remove the weak coupling.

4.2 Leakage Loss

Figure 4.1 shows the full hollow-core fiber geometry with 6 tubes in the cladding. Only a quarter of the geometry is used in modeling hollow-core negative curvature

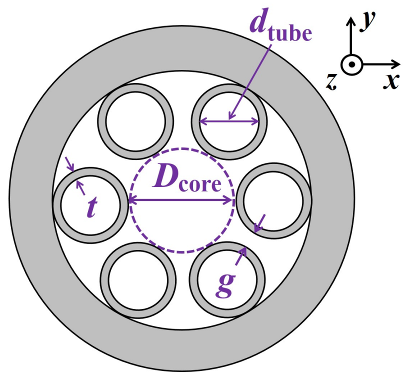

Figure 4.1: Cross section of the chalcogenide negative curvature fiber with 6 cladding tubes.

fibers because of the symmetry of the modes [139,151,182]. The gray regions represent glass, and the white regions represent air. The inner tube diameter, d_{tube}, the core diameter, D_{core}, the tube wall thickness, t, the number of tubes, k, and the minimum gap between the cladding tubes, g, have the following relationship: $D_{\text{core}} = (d_{\text{tube}} + 2t + g)/\sin(\pi/\text{k}) - (d_{\text{tube}} + 2t)$ [58,150]. The core diameter, D_{core}, is fixed at 150 μm, and the ratio of the core diameter to the wavelength is $D_{\text{core}}/\lambda = 30$. Different negative curvature fibers were fabricated using a ratio of the core diameter to the wavelength that varies from 31 to 36 [49–51, 69]. We simulate As_2S_3 chalcogenide glass with a refractive index whose real part equals 2.4 and whose imaginary part equals 3.4×10^{-8} at a wavelength $\lambda = 5$ μm [183].

Now, we study the leakage loss in chalcogenide fibers with different tube wall thicknesses and different gaps between the cladding tubes. Figure 4.2 shows the leakage loss as a function of tube wall thickness for a fiber with different gaps when the tube wall thickness increases from 0.5 μm to 3.5 μm. There are three thicknesses at $t = 1.2$ μm, 2.4 μm, and 3.5 μm, near which high loss occurs. These tube wall thicknesses match the resonance condition, $t = m\lambda/[2(n_1^2 - n_0^2)^{1/2}]$, where m equals any positive integer, λ is the light wavelength, and $n_1 = 2.4$ and $n_0 = 1.0$ are the refractive indices of chalcogenide glass and air, respectively [32,34]. We show the first three transmission bands, labeled I, II, and III, that occur between the three tube wall thicknesses, at which high loss is present. The tube wall thicknesses corresponding to the minimum loss for these three transmission bands are located at 0.7 μm, 1.8 μm, and 2.9 μm. These values are consistent with the antiresonance condition, $t = (m - 0.5)\lambda/[2(n_1^2 - n_0^2)^{1/2}]$, where m equals any positive integer [32, 34]. The tube wall thickness corresponding to the minimum loss only changes slightly when the gap increases from 10 μm to 40 μm.

In Fig. 4.3(a), we plot the leakage loss as a function of the gap with tube wall thicknesses of 0.7 μm, 1.8 μm, and 2.9 μm. The leakage loss decreases when the gap is first introduced, and the leakage loss increases as the gap increases. When there is no gap, two nearby tubes create nodes where the mode field can reside [43, 51]. However, when the gap is too large, the field leaks through the gap, and the leakage loss increases. Figure 4.3(b) shows the normalized mode intensity in the fiber with a gap of 30 μm, a tube thickness of 1.8 μm, and a wavelength of 5 μm.

We also studied the leakage loss as a function of wavelength with different gaps. Figures 4.4(a) ands 4.4(b) show the results with tube wall thicknesses of 1.8 μm

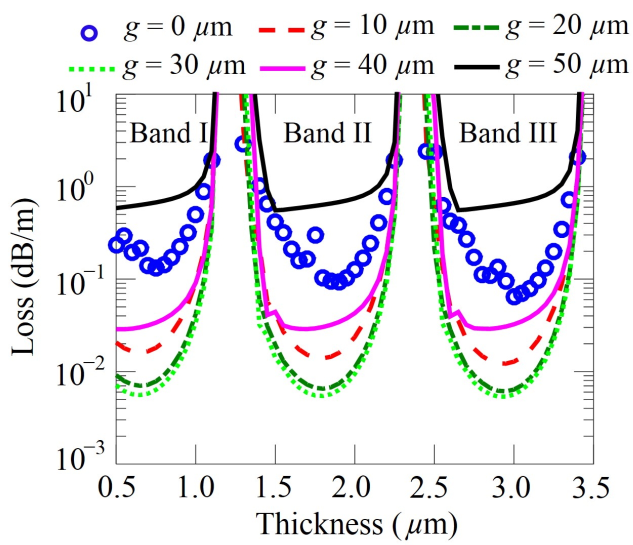

Figure 4.2: Leakage loss as a function of tube wall thickness with different gaps. The wavelength is 5 μm.

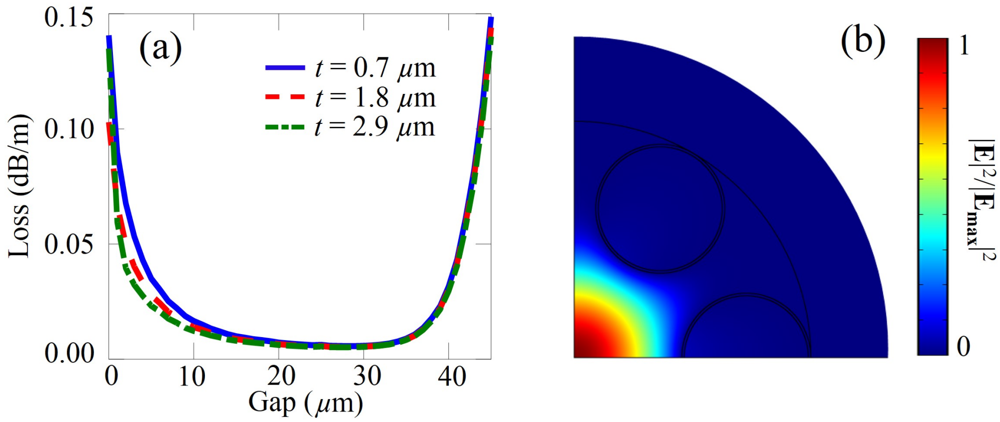

Figure 4.3: (a) Leakage loss as a function of the gap with different tube wall thicknesses of 0.7 μm, 1.8 μm, and 2.9 μm and with a wavelength of 5 μm. (b) Normalized mode intensity in the fiber with a gap of 30 μm and a tube thickness of 1.8 μm.

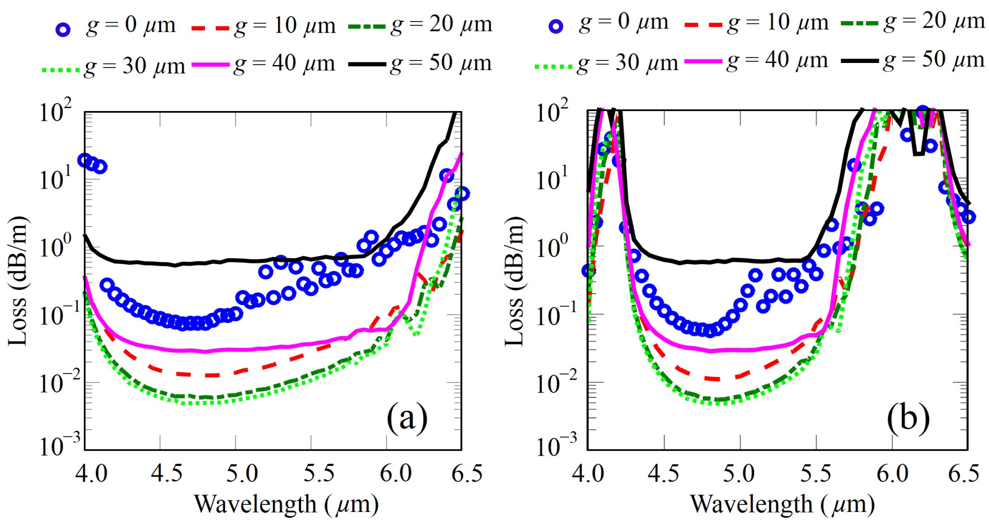

Figure 4.4: Leakage loss as a function of wavelength with different gaps for tube thicknesses of (a) 1.8 μm and (b) 2.9 μm.

and 2.9 μm, respectively, corresponding to the tube wall thicknesses of transmission bands II and III in Fig. 4.2. The material dispersion is also included in the simulation [184, 185]. Again, the leakage loss can be decreased when an appropriate gap is used. The minimum loss occurs at a wavelength slightly lower than 5 μm because the core size is effectively larger at a smaller wavelength. The differences between the losses at a wavelength of 5 μm and at the wavelengths corresponding to the minimum loss,

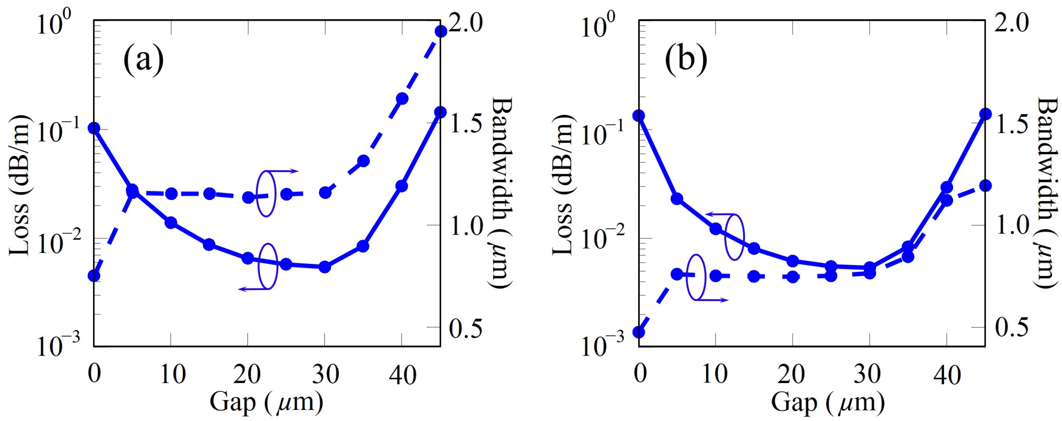

Figure 4.5: The loss at a wavelength of 5 μm and bandwidth as a function of the gap for tube wall thicknesses of (a) 1.8 μm and (b) 2.9 μm.

which is near 4.8 μm, is only 11% and 12% for thicknesses of 1.8 μm and 2.9 μm, respectively, between gaps of 10 μm and 40 μm. We also confirmed that the minimum loss occurs at a wavelength slightly lower than 5 μm even when the material dispersion is neglected.

We also plot the leakage loss at 5 μm as a function of the gap for thicknesses of 1.8 μm and 2.9 μm using the blue solid curves in Figs. 4.5(a) and 4.5(b), respectively. The leakage loss can be decreased by factors of 19 and 25 for thicknesses of 1.8 μm and 2.9 μm, respectively, when an appropriate gap is used.

4.3 Bandwidth

Bandwidth is another important parameter. Here, we define the bandwidth as the transmission window where the leakage loss is less than twice the minimum leakage loss. The bandwidth as a function of the gap for both thicknesses of 1.8 μm and 2.9 μm is shown using the blue dashed curves in Figs. 4.5(a) and 4.5(b), respectively. When the gap increases from $g = 0$ to $g = 5$ μm, the bandwidth increases sharply. When the gap increases from $g = 5$ μm to $g = 30$ μm, the bandwidth stays almost the same. When the gap increases from $g = 30$ μm to $g = 42.5$ μm, the bandwidth further increases with the tradeoff that the minimum loss at the center of the transmission band increases, as shown in Fig. 4.5. The bandwidth for a tube wall thickness of 1.8 μm in Band II is wider than the bandwidth for a tube wall thickness of 2.9 μm in Band III, as shown in both Figs. 4.4 and 4.5. In negative curvature fibers, the operating wavelength sits between the nearby resonance wavelengths at $\lambda = 2t(n_1^2 - n_0^2)^{1/2}/m$, where m equals any positive integer and t is the tube wall thickness. Hence, a lower-order transmission band with a smaller m will yield a wider bandwidth.

Comparing the leakage loss and bandwidth in Fig. 4.5, the gap should be chosen in the range between 5 μm and 40 μm, depending on the tradeoff between loss and bandwidth in specific applications. When the gap is between 5 μm and 40 μm, the bandwidth can be 1.1 μm and 0.75 μm in the fibers with tube wall thicknesses of 1.8 μm and 2.9 μm, respectively. The corresponding ratios of the bandwidth to the central wavelength are 22% and 15%. Meanwhile, the losses at 5 μm can be lower than 0.04 dB/m in both fibers. The broad range of gaps that have nearly minimum loss allows successful fiber devices as it might be hard to exactly control the size of the gap in the fiber drawing process.

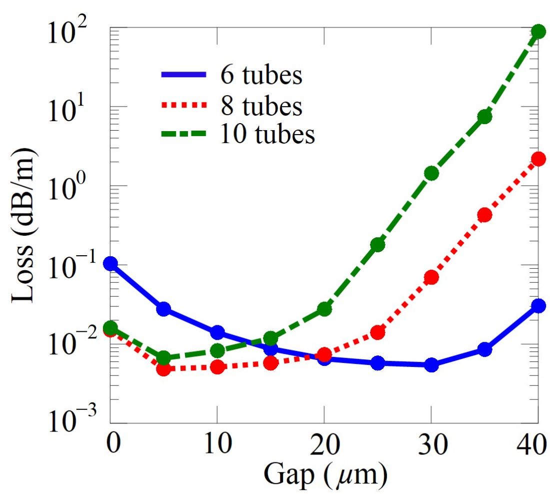

Figure 4.6: Leakage loss as a function of gap in fibers with 6, 8, and 10 cladding tubes. The tube wall thickness is 1.8 μm and the wavelength is 5 μm.

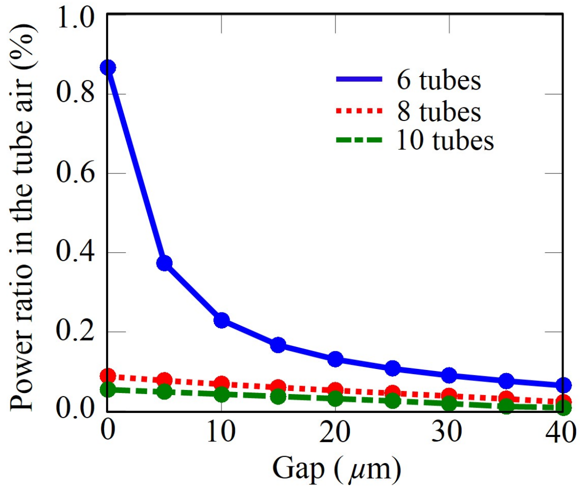

Figure 4.7: Power ratio inside the tubes as a function of the gap in fibers with 6, 8, and 10 cladding tubes. The tube wall thickness is 1.8 μm and the wavelength is 5 μm.

4.4 Number of Tubes

In previous sections, we studied the leakage loss and the bandwidth in negative curvature fibers with 6 cladding tubes. In this section, we study the effect of the gap on the leakage loss and the bandwidth in fibers with 8 and 10 cladding tubes. The core diameter, the tube wall thickness, and the wavelength are fixed at 150 μm, 1.8 μm, and 5 μm, respectively. We only study the transmission Band II at a tube wall thickness of 1.8 μm in this section, because we find no significant difference in leakage loss between Band II and Band III, as shown in Figs. 4.3, 4.4, and 4.5. Figure 4.6 shows the leakage loss as a function of the gap for fibers with 6, 8, and 10 cladding tubes. The blue solid curve shows the leakage loss of a fiber with 6 cladding tubes, which is the same as the blue solid curve in Fig. 4.5(a). For a fiber with 6 cladding tubes, the leakage loss decreases by a factor of 19 when an appropriate gap is used. For fibers with 8 and 10 cladding tubes, the leakage losses only decrease by 66% and 49% when the gap increases from 0 to 10 μm, respectively. The optimal gap in a fiber with 6 cladding tubes is 3 times as large as the optimal gap in fibers with 8 or 10 cladding tubes.

In order to find the reason for the difference between the behavior with 6, 8, and 10 cladding tubes, we plot the power ratio inside the tubes for fibers with 6, 8, and 10 cladding tubes in Fig. 4.7. The power ratio inside the tubes is defined as the ratio of the power inside all the cladding tubes to the total power in the fiber geometry. For a fiber with 6 cladding tubes, the power ratio inside the tubes decreases by a factor of 3.8, when the gap increases from 0 to 10 μm. For fibers with 8 and 10 cladding tubes, the power ratios inside the tubes only decrease by 22% and 21% when the gap increases from 0 to 10 μm, respectively. This study shows that the gap has more impact on the power ratio inside the tubes for a fiber with 6 cladding tubes.

We further study the normalized electric field intensity at $g = 0$ and $g = 10$ μm in fibers with 6 and 8 cladding tubes. Figure 4.8(a) shows one quarter of the fiber geometry with 6 cladding tubes. Figure 4.8(c) shows the normalized electric field intensity in a fiber with 6 cladding tubes along x-axis at $y = 0$. We can see the mode is confined inside the core radius of 75 μm for both $g = 0$ and $g = 10$ μm. The thin gray vertical bar indicates the location of the glass tube at $x = 75$ μm with a thickness of 1.8 μm. The field between $x = 76.8$ μm and $x = 203$ μm is inside the cladding tube for the fiber with $g = 10$ μm indicated by the red dashed curve, which shows exponential decay inside the cladding tubes. For the fiber with $g = 0$, the field between $x = 76.8$ μm and $x = 223$ μm is inside the cladding tube indicated by the blue solid curve, which shows noticeable field due to the weak coupling between the core mode and the tube modes. Note that the fiber with $g = 0$ has a cladding tube diameter of 146 μm that is close to the core diameter of 150 μm. On the other hand, the fiber with $g = 10$ μm has a cladding tube diameter of 126 μm that is much smaller than the core diameter. Hence, the gap effectively decreases the diameter of tube, which reduces the coupling between the core mode and the tube modes. The gap also induces an abrupt decrease in the power ratio inside the tubes, as shown in Fig. 4.7.

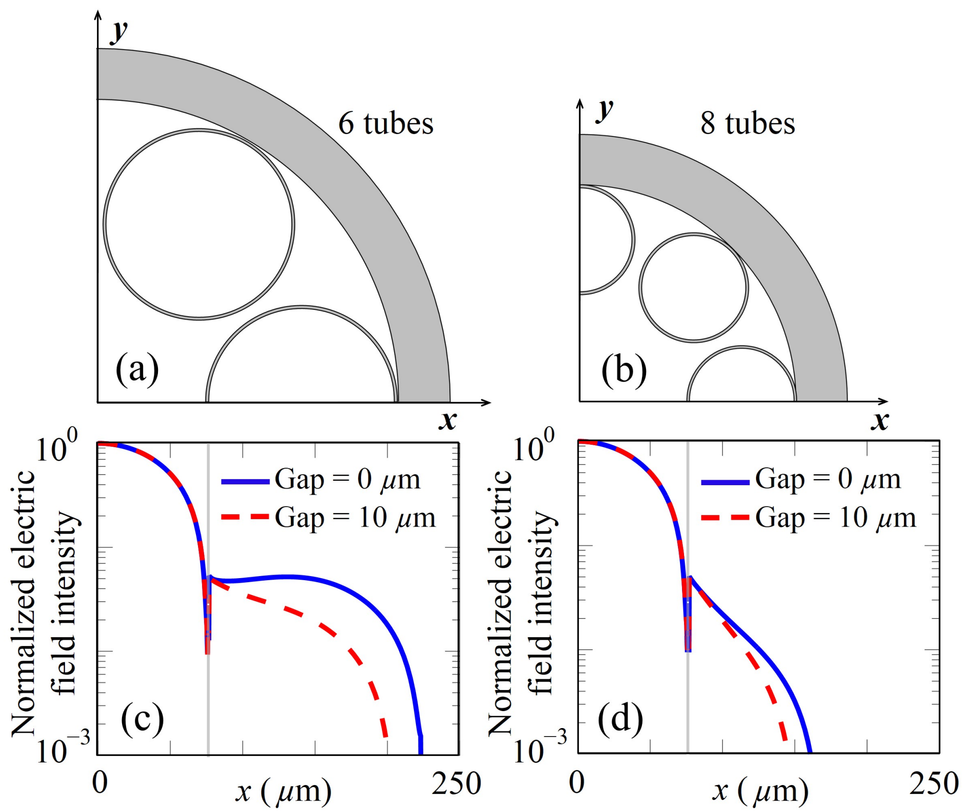

Figure 4.8: Normalized electric field intensity at $g = 0$ and $g = 10$ μm in fibers with (a) 6 and (b) 8 cladding tubes. The tube wall thickness is 1.8 μm and the wavelength is 5 μm. The thin gray vertical bars indicate the location of the glass tube at $x = 75$ μm with a thickness of 1.8 μm.

A quarter of the fiber geometry with 8 cladding tubes is shown in Fig. 4.8(b). In this case, the diameter of tube is much smaller than the diameter of the central air core. There is almost no coupling between the central air-core mode and the cladding-tube modes, and the electric field intensities decay exponentially along the x-axis in the cladding tubes for both $g = 0$ and $g = 10$ μm, as shown in Fig. 4.8(d). Hence, for a fiber with 8 or 10 cladding tubes, there is no sharp decrease in the power ratio inside the tubes when the gap first becomes non-zero, as shown in Fig. 4.7. The power ratio inside the tubes decreases almost linearly when the gap increases from 0 to 40 μm. The optimal gap of 5 μm to 10 μm for the fiber with 8 or 10 cladding tubes is much smaller than the optimal gap of 30 μm for a fiber with 6 cladding tubes, which is needed to remove the weak coupling between the core mode and the tube modes. In Fig. 4.7, we show the light intensity with the electric field polarized in the x-direction. The other polarization yields similar results.

In nested negative curvature fibers, where another nested tube is inside each major lattice tube, a small gap should be used to minimize the loss [43]. A much larger gap should be used in standard negative curvature fibers with six cladding tubes, as shown in Fig. 4.1, because a weak coupling between the core mode and tube modes plays an important role in this case and must be minimized.

Figure 4.9 shows a bandwidth comparison among fibers with 6, 8, and 10 cladding tubes. The blue dashed curve is the same as the blue dashed curve in Fig. 4.5(a). When the gap increases from 0 to 5 μm, the bandwidth increases sharply due to the removal of the nodes from the connecting tubes. The bandwidths for fibers with 6 and 8 cladding tubes further increase as the gap increases from 25 μm to 40 μm, with the tradeoff of increased leakage loss at the central wavelength. For a fiber with 10 tubes, the tube diameter is too small to confine the mode in the core when the gap is

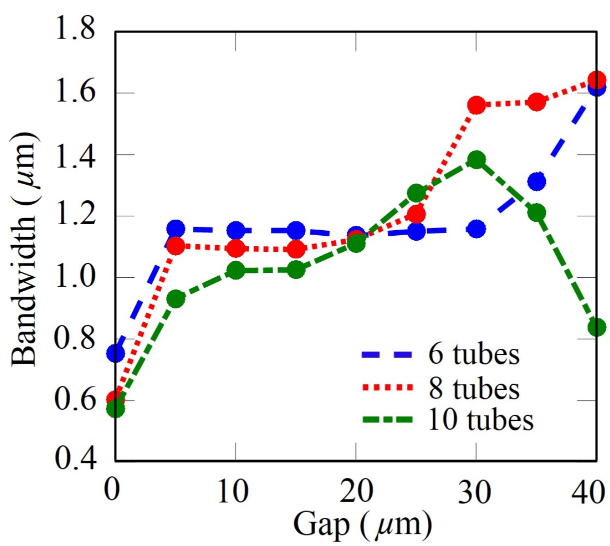

Figure 4.9: Bandwidth as a function of the gap in fibers with 6, 8, and 10 cladding tubes. The tube wall thickness is 1.8 μm.

40 μm, as shown in Fig. 4.6. The bandwidth for a fiber with 10 tubes also decreases accordingly when the gap is 40 μm, as shown in Fig. 4.9.

4.5 Conclusion

In this chapter, we design tube structure in chalcogenide negative curvature fibers. Fibers with tube wall thicknesses of 0.7 μm, 1.8 μm, and 2.9 μm satisfy an antiresonance condition and have the minimum leakage loss at a wavelength of 5 μm. The gap can effectively decrease the transmission loss by a factor of 19 in the negative curvature fiber with 6 cladding tubes. We find that there is a range of the gaps, which correspond to a low leakage loss and a wide transmission bandwidth. Using a fiber with a tube wall thickness of 1.8 μm and a gap range between 5 μm and 40 μm, a low transmission loss of under 0.04 dB/m and a bandwidth of 1.1 μm can be achieved simultaneously in chalcogenide negative curvature fibers. It is found that a lower-order transmission band yields a wider bandwidth than the bandwidth from a higher-order transmission band. The optimal gap corresponding to the minimum loss in a fiber with 6 cladding tubes is 3 times as large as the optimal gap in fibers with 8 or 10 cladding tubes. A larger gap is required to remove the weak coupling between the core mode and tube modes in a fiber with 6 cladding tubes. In summary, a fiber design with low sensitivity to exact gaps allows low-loss and broadband chalcogenide fiber devices even with some uncertainties in the fiber drawing process.

CHAPTER FIVE

Higher-Order Mode Suppression in Chalcogenide Negative Curvature Fibers

This chapter published as [70]: C. Wei, R. A. Kuis, F. Chenard, C. R. Menyuk, and J. Hu, "Higher-order mode suppression in chalcogenide negative curvature fibers," Opt. Express **23**, 15824–15832 (2015).

In this chapter, we find conditions for suppression of higher-order core modes in chalcogenide negative curvature fibers with an air core. An avoided crossing between the higher-order core modes and the fundamental modes in the tubes surrounding the core can be used to resonantly couple these modes, so that the higher-order core modes become lossy. In the parameter range of the avoided crossing, the higher-order core modes become hybrid modes that reside partly in the core and partly in the tubes. The loss ratio of the higher-order core modes to the fundamental core mode can be more than 50, while the leakage loss of the fundamental core mode is under 0.4 dB/m. We show that this loss ratio is almost unchanged when the core diameter changes and so will remain large in the presence of fluctuations that are due to the fiber drawing process.

5.1 Introduction

Negative curvature fibers have been simulated and fabricated in silica with core diameters ranging from 30 μm to 110 μm for transmission wavelengths between 1 μm and 4 μm [43, 49, 50, 52, 54, 64, 65, 69]. A chalcogenide negative curvature fiber has been fabricated with a large core size of 380 μm to transmit light from a CO_2 laser at 10.6 μm [55]. Fibers with a large core diameter like this one have low-loss transmission with low nonlinearity. On the other hand, fibers with a large core diameter have higher-order core modes. It is desirable for many applications to suppress the higher-order modes, which would decrease the coupling between the fundamental and higher-order core modes due to small perturbations like microbending [37, 186].

In this chapter, we show computationally that it is possible to suppress higher-order core modes in a chalcogenide negative curvature fiber while preserving low leakage loss for the fundamental core mode. The mechanism is resonant coupling between the higher-order core modes and the fundamental tube modes. This approach is analogous to using defect modes in a photonic bandgap fiber [186–189]; however, there is no need to create defects in this case, since the tubes that create the negative curvature can also provide the resonant coupling. Avoided crossings lead to high loss for fiber modes [190, 191]. It is possible to design negative curvature fiber so that an avoided crossing between the higher-order core modes and the fundamental tube modes leads to an increase in the loss of the higher-order core modes. The higher-order core modes in the parameter range of the avoided crossing are really hybrid modes that reside partly in the core and partly in the tubes. The loss ratio of the higher-order core modes to the fundamental core mode can be greater than 50, while the leakage loss for the fundamental core mode is still under 0.3 dB/m.

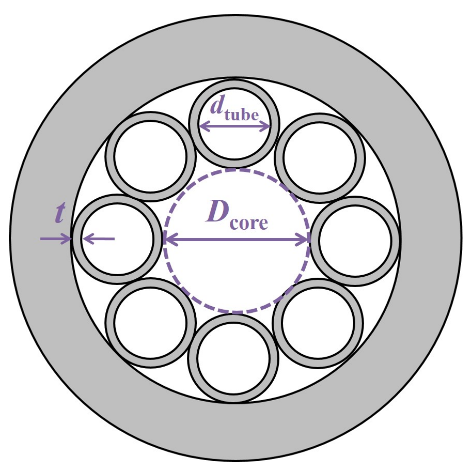

Figure 5.1. Cross-section of the chalcogenide negative curvature fiber.

5.2 *Avoided Crossing Between Higher-Order Core Modes and Tube Modes*

Figure 5.1 shows the full hollow-core PCF geometry. The gray regions represent glass, and the white regions represent air. Only a quarter of the geometry is used in modeling hollow-core PCFs because of the symmetry of the modes [139, 151]. We model a hollow-core PCF with eight cladding tubes. The inner tube diameter, d_{tube}, and the inner core diameter D_{core}, are related by the expression $D_{\mathrm{core}} = (d_{\mathrm{tube}} + 2t)/\sin(\pi/8) - (d_{\mathrm{tube}} + 2t)$. We use t to denote the thickness of the tube walls. We use a core diameter, $D_{\mathrm{core}} = 60$ μm, and a wavelength, $\lambda = 2$ μm. We vary the tube wall thickness t to obtain an avoided crossing. We simulate As_2S_3 chalcogenide glass with a refractive index whose real part equals 2.4 and whose imaginary part equals 1.1×10^{-8} [183].

In order to confine light in the core of the negative curvature fiber, the wall thickness of the tubes must not be resonant with the wavelength of the light. Resonance occurs when $t = m\lambda/2/(n_1^2 - n_0^2)^{1/2}$, where m is any positive integer, λ is the light wavelength, and where $n_1 = 2.4$ and $n_0 = 1.0$ are the real parts of the refractive indices of chalcogenide glass and air, respectively. At resonance, the phase of the electric field changes by a multiple of 2π from one side of the tube wall to the other [34, 35, 42, 192]. The values of t that correspond to $m = 1$, 2, and 3 are 0.46, 0.92, and 1.38 μm, respectively. We study the first transmission band, so that $t < 0.46$ μm. Figure 5.2(a) shows the real part of the effective indices of the core modes and the tube modes as a function of t. Figure 5.2(b) shows the loss of the core modes, and Fig. 5.2(c) shows the ratio of the loss of the TE_{01} to the loss of the HE_{11} core mode. The TE_{01} mode is the higher-order core mode that has the lowest loss, and the HE_{11} mode is the fundamental core mode. The loss ratio of these two modes reaches a maximum of 58 when $t = 0.42$ μm; at this wall thickness, the loss of the fundamental core mode is 0.32 dB/m. Hence, higher-order core modes can be suppressed in combination with low transmission loss for the fundamental core mode.

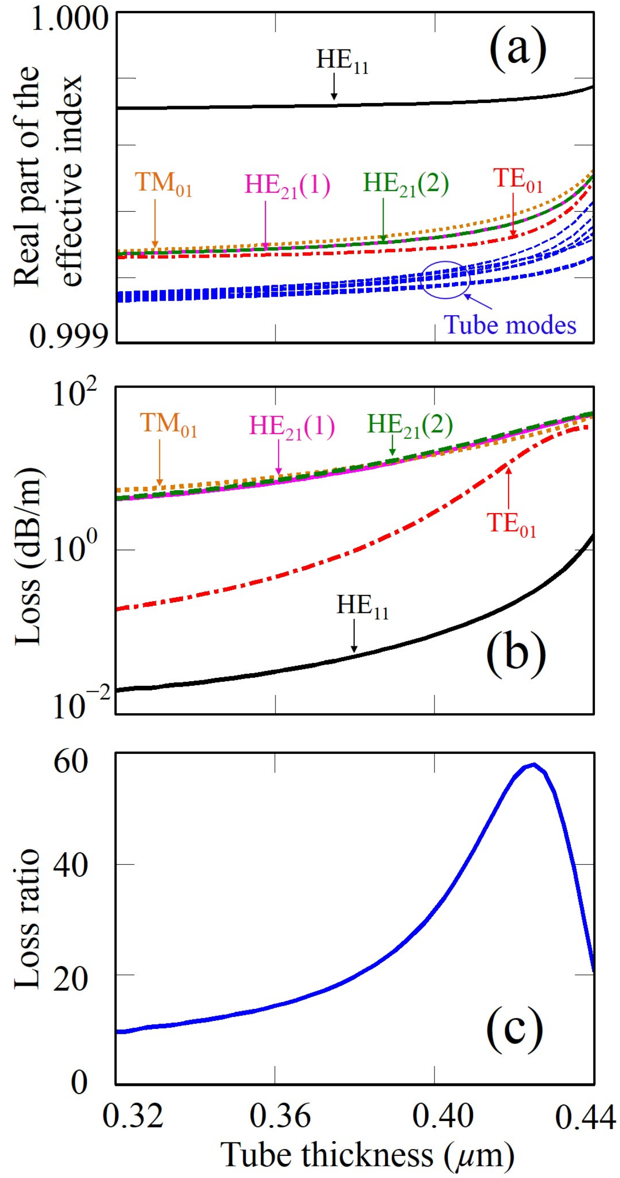

Figure 5.2: Real part of (a) the effective index and (b) the leakage loss of the fundamental HE_{11} core mode, the TE_{01} core mode, the TM_{01} core mode, and the two degenerate HE_{21} core modes in the chalcogenide negative curvature fiber. The blue dashed curves correspond to the tube modes. (c) Loss ratio of the TE_{01}core mode to the fundamental HE_{11} core mode.

We repeated the same analysis for the second and third transmission bands. The maximum loss ratio of the higher-order core modes to the fundamental core mode reaches 39 and 28 when $t = 0.88$ and 1.33 μm, respectively. The corresponding losses of the fundamental core modes are 0.4 and 0.55 dB/m.

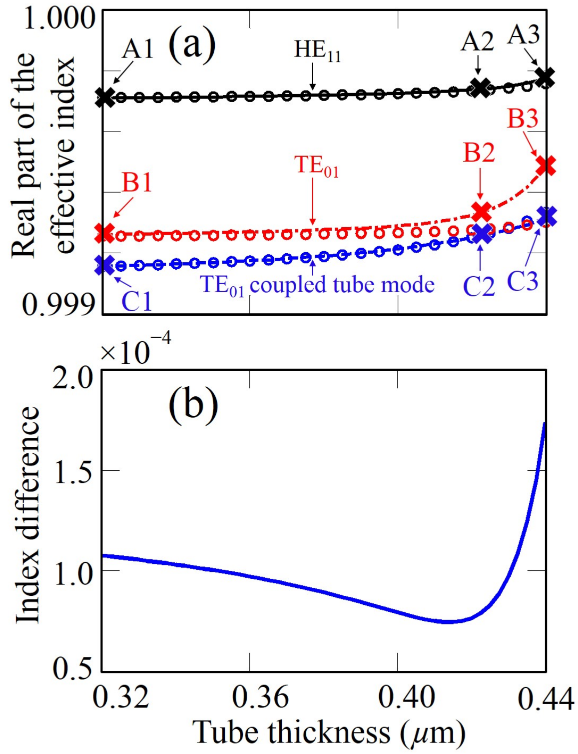

Figure 5.3: (a) Real part of the effective index of the HE_{11} core mode, the TE_{01} core mode and corresponding tube mode that couples to the TE_{01} core mode. The open circles represent the real part of the effective index of the corresponding modes using the annular core fiber model. (b) Effective index difference between the TE_{01} core mode and tube mode that is coupled to the TE_{01} core mode.

In order to study the coupling mechanism, we show the avoided crossing between the TE_{01} core mode and the corresponding tube mode that couples to it at the avoided crossing. In Figs. 5.3, 5.4, and 5.5, we use A1, A2, and A3 to label the fundamental core mode (HE_{11} mode) when $t = 0.32$, 0.42, and 0.44 μm, respectively. We use B1, B2, and B3 to label the TE_{01} core mode and C1, C2, and C3 to label the corresponding tube mode at the same three thicknesses. Figure 5.3(a) shows the real part of the effective index for the TE_{01} core mode and the corresponding tube mode as the tube thickness increases from 0.32 to 0.44 μm. For reference, we also show the real part of the effective index of the fundamental core mode. Since both the TE_{01} core mode and the corresponding tube mode reside in air and interact with the same tube wall, they vary in a similar way as the wall thickness increases. As a consequence, the avoided crossing happens slowly as the tube thickness changes from 0.40 to 0.44 μm. Nonetheless, the avoided crossing is clearly visible in the effective index and in the mode fields. The difference of the effective indices between the TE_{01} core mode and the corresponding tube mode, as shown in Fig. 5.3(b), reaches a minimum at $t = 0.42$ μm, which is also the tube thickness at which the loss ratio of the TE_{01}core mode to the fundamental HE_{11} core mode reaches its maximum, as shown in Fig. 5.2(c).

We show the mode fields in Fig. 5.4. The color indicates the electric field, normalized to its maximum, while the arrows indicate the direction of the transverse electric field and the lengths of the arrows are proportional to the amplitude of the transverse electric field. When $t = 0.32$ μm, both the TE_{01} core mode and the corre-

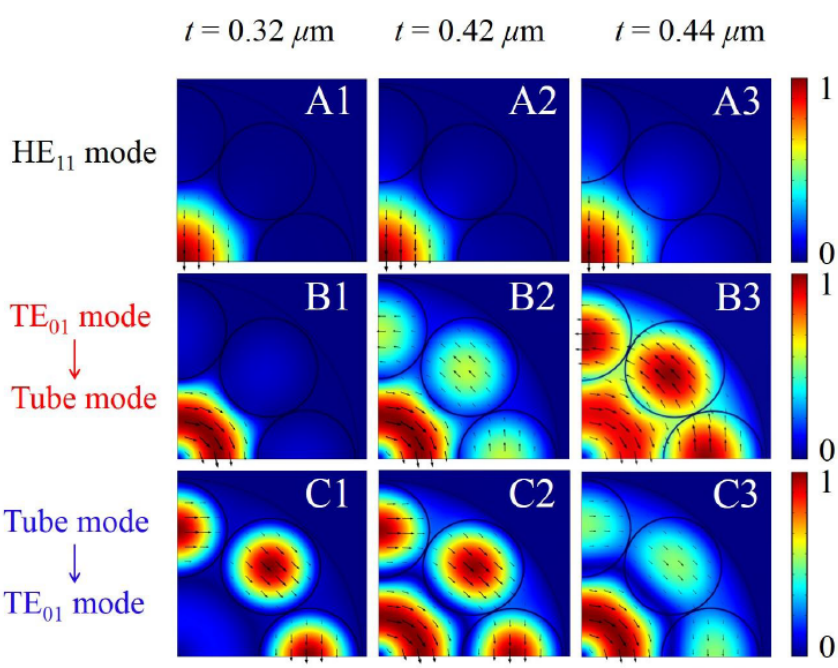

Figure 5.4: Mode fields of the HE_{11} core mode, the TE_{01} core mode, and the tube mode that couples with the TE_{01} core mode at tube thicknesses of 0.32 μm, 0.42 μm and 0.44 μm, respectively, corresponding to the same labeled crosses in Fig. 5.3(a) and Fig. 5.5. The contour plots represent the normalized electric field intensity and the arrows represent the amplitude and direction of the transverse electric field.

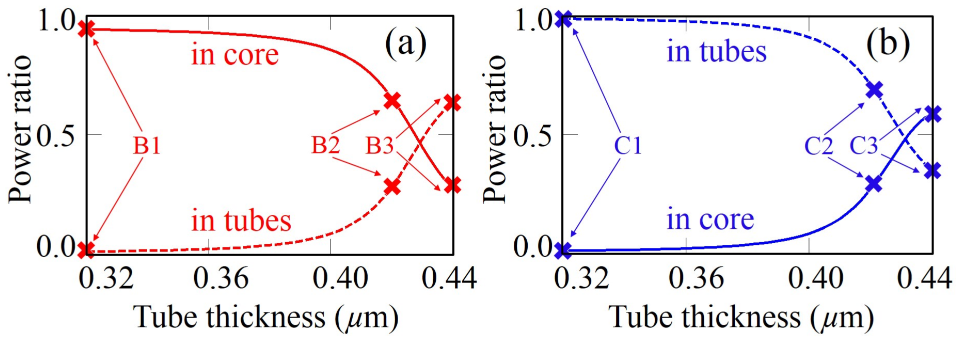

Figure 5.5: (a) The power ratio in the core and the power ratio in the tubes for the TE_{01} core mode. (b) The power ratio in the core and the power ratio in the tubes for the corresponding tube mode that couples with the TE_{01} core mode.

sponding tube mode are well-confined to the core and the tubes, respectively. When $t = 0.42$ μm, in the center of the parameter range in which the avoided crossing occurs, both the original TE_{01} core mode and corresponding tube mode reside partly in the core and partly in the cladding tubes. Both have effectively become hybrid modes. When $t = 0.44$ μm, most of the original TE_{01} core mode resides in the tubes and vice versa. In Fig. 5.5, we show the ratios of the power in the core and the power in the tubes to the total power in the fiber for both modes as a function of t. The crossing point, which occurs at $t = 0.43$ μm, is clearly visible. By contrast, the fundamental core mode is almost unaffected by the avoided crossing, and the fraction of its power that is in the core falls gradually from 0.98 to 0.88 as t increases from 0.32 μm to 0.44 μm. Note that other higher-order core modes, the TM_{01} and HE_{21} modes also have avoided crossings at $t = 0.42$ μm, although the effect of the avoided crossing is not as strong as the effect on the TE_{01} core mode, as shown in Fig. 5.2(b).

5.3 Comparison Between Negative Curvature and Annular Core Fibers

Here, we analyze the higher-order core modes and fundamental tube modes in a negative curvature fiber when they are effectively decoupled, which allows us to predict when an avoided crossing will occur. We use annular core fibers to predict the effective indices of the modes in the air core and a cladding tube of a negative curvature fiber. The annular core fiber is just a glass ring suspended in air [145, 146, 177]. Figure 5.6 shows two different annular core fibers used to study the modes in the core and a cladding tube of the negative curvature fiber. To study the modes in the tube, we use an annular core fiber with the same glass thickness and core diameter as the tubes in the negative curvature fiber. To study the modes in the air core, we use an annular core fiber with the same glass thickness as the glass thickness in the negative curvature fiber. We increase the core diameter in the annular core fiber by 5% to account for the effective increase in the core diameter that occurs in a negative curvature fiber. With this increase in the core diameter, we have found that the effective indices of the core modes in the negative curvature fiber match the effective indices of the modes in the corresponding annular core fiber within 0.001% for the tube thicknesses between 0.32 and 0.37 μm, as shown in Fig. 5.3(a). We solve for the modes in the air core of the annular core fiber and plot the real part of the effective indices of different modes as open circles in Fig. 5.3(a). The blue circles represent the effective index of the tube mode using an annular core fiber with the same diameter as a single tube in the negative curvature fiber. The black and red circles represent the effective indices of the fundamental core mode and the TE_{01}

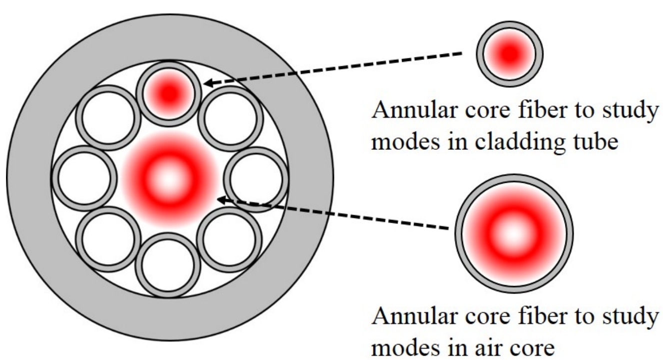

Figure 5.6: Annular core fibers are used to study the modes in the tube and the core of a negative curvature fiber.

core mode, respectively. We can see that corresponding solid curves and circles agree very well for tube thicknesses between 0.32 and 0.37 μm. At a larger tube thickness region, the blue circles and red circles cross each other at the tube thickness of the 0.42 μm. Hence, the crossing point of the decoupled modes in the annular core fibers is consistent with the avoided-crossing point of the coupled modes in the negative curvature fiber, as shown in section 5.2. Annular core fibers can thus be used to provide a simple prediction of the avoided crossing between the higher-order core modes and the tube modes.

5.4 Higher-Order Mode Suppression with Different Core Diameters

We also studied the possibility of suppressing higher-order core modes by using different core diameters or a different number of tubes. When we increase the core diameter, we increase the tube diameter proportionally. The effective indices of the modes in the core and tubes change by nearly the same amount. We find that the index difference between the higher-order (TE_{01}) core mode and the corresponding coupled tube modes only changes by 2×10^{-5} when the core diameter changes from

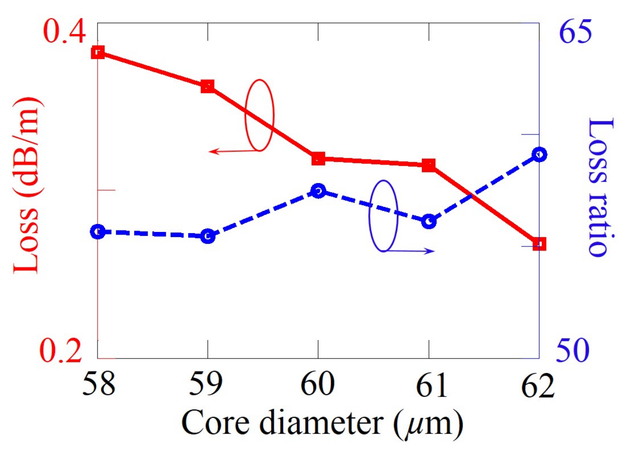

Figure 5.7: Loss of the fundamental core mode and loss ratio of the lowest-loss, higer-order (TE_{01}) core mode to the fundamental core mode as a function of core diameter. The tube thickness is fixed at 0.42 μm.

50 μm to 60 μm. Hence, changing the core diameter does not significantly change the resonant coupling condition. On the other hand, one can benefit from this property because as one varies the core diameter, the avoided crossing condition and the higher-order mode suppression still occur. In addition, the loss of the fundamental core mode decreases as the core diameter increases. Figure 5.7 shows the loss coefficient of the fundamental core mode as a red solid curve, and it shows the loss ratio of the lowest-loss, higher-order (TE_{01}) core mode relative to the fundamental core mode as a blue dashed curve, as one changes core diameter. The tube thickness is fixed at 0.42 μm. The loss of the fundamental core mode decreases from 0.38 to 0.27 dB/m, while the loss ratio varies between 55 and 59 when we increase the core diameter from 58 to 62 μm. Hence, the higher-order mode suppression will be robust in the presence of core diameter fluctuations due to the fiber drawing process.

Instead of increasing the diameter of the tubes, one might increase the number of tubes, in which case the core diameter does not change and the tube diameter decreases. At the end, the effective index for the core mode does not change much and the effective index for the cladding tube mode decreases. The increasing index difference between the higher-order core modes and cladding tube modes will not enable the resonant coupling between the higher-order core modes and cladding tube modes. On the other hand, if we decrease the number of tubes from eight to six, the hexagonal fiber structure would effectively have the same core diameter and tube diameter. In this case, the fundamental core mode would easily couple to the tube modes, which should be avoided.

5.5 Conclusion

In this chapter, we study higher-order core mode suppression in chalcogenide negative curvature fibers. In a negative curvature fiber, there is no need to create additional defect cores in the cladding region. The cladding tubes automatically serve as outer defect cores. The higher-order core modes can be suppressed using the avoided crossing between the higher-order core modes and the corresponding cladding tube modes. When the core diameter is 60 μm and the tube thickness is 0.42 μm, the loss ratio of the higher-order core modes to the fundamental core mode can be more than 50, while the leakage loss of the fundamental core mode is still under 0.4 dB/m. The higher-order core mode suppression is robust even with fluctuations of the core diameter that are induced by the fiber drawing process.

CHAPTER SIX

Bending-Induced Coupling in Chalcogenide Negative Curvature Fibers

This chapter published as [150]: C. Wei, C. Menyuk, and J. Hu, "Bending-induced mode non-degeneracy and coupling in chalcogenide negative curvature fibers," Opt. Express **24**, 12228–12239 (2016).

In this chapter, we study bend loss in chalcogenide negative curvature fibers with different polarizations, different tube wall thicknesses, and different bend directions relative to the mode polarization. The coupling between the core mode and tube modes induces bend loss peaks in the two non-degenerate modes at the same bend radius. There is as much as a factor of 28 difference between the losses of the two polarization modes. The fiber with a larger tube wall thickness, corresponding to a smaller inner tube diameter, can sustain a smaller bend radius. The bend loss is sensitive to the bend direction when coupling occurs between the core mode and tube modes. A bend loss of 0.2 dB/m at a bend radius of 16 cm, corresponding to 0.2 dB/turn, can be achieved in a chalcogenide negative curvature fiber.

6.1 Introduction

The relative simplicity of the negative curvature structure could enable the fabrication of fiber devices for mid-IR applications using non-silica glasses, such as chalcogenide. Using chalcogenide negative curvature fibers, the delivery of mid-infrared radiation has been successfully demonstrated for a CO_2 laser at a wavelength of 10.6 μm [55]. Mid-infrared light sources and transmission are important for applications to biosensing, environmental monitoring, homeland security, and medical diagnostics [180, 193]. The development of quantum cascade lasers has shown great potential for the generation of mid-infrared emission around 5 μm with a wall plug efficiency of 50% [181, 194, 195] and a watt-level power output [196]. While transmission of light in silica negative curvature fibers has been demonstrated at wavelengths up to 4 μm [52], the material loss of chalcogenide glass is four orders of magnitude or more lower than silica glass at wavelengths at or above 5 μm [51, 183]. So, it is preferable to use chalcogenide glass at these wavelengths.

In negative curvature fibers, core sizes from 20 μm to 380 μm have been used [47–55, 64, 65, 114, 161]. Fibers with a large core size have a low leakage loss [135]. At the same time, fibers with a large core size have many higher-order modes [70]. Several structures have been suggested to suppress higher-order modes using the resonant coupling between the higher-order core modes and cladding modes [43, 66, 70, 80, 197, 198]. Another important limiting factor in fiber devices is the bend loss. Bend effectively introduces structure distortion, especially for fibers with a large core cross section [69, 83, 179, 199]. It is preferable for a fiber to insensitive to bends when it is used for light delivery. Conversely, however, bend sensitivity can be useful for sensing. In bandgap fibers, since the cladding air holes are much smaller than the central air core, there is not much loss due to the mode coupling between the core modes and the cladding modes. The bend loss for a bandgap fiber is mainly due to distortion of the fiber structure. In negative curvature fibers, besides the structure's distortion, the mode coupling between the core mode and tube modes leads to an increase in the loss of the core modes. Bending-induced higher-order mode suppression has been obtained using the resonant coupling between the higher-order core modes and the tube modes in negative curvature fibers [58]. Structures that include nested cladding tubes or smaller cladding tubes have also been proposed to decrease the bend loss [43, 69]. To date, there is no detailed study on two polarization modes in bent negative curvature fibers [38, 43, 68, 69, 83, 179, 197, 199]. In this chapter, we study the bending-induced mode coupling for the non-degenerate core modes in chalcogenide negative curvature fibers. Fiber bends break the symmetry of the fiber geometry, and the fundamental core modes become non-degenerate modes in bent negative curvature fibers. It is thus necessary to take into account the mode polarization when calculating the loss in bent fibers. We find that the loss in the two polarization modes can differ by up to a factor of 28.

The rest of the chapter is organized as follows: In section 6.2, we show the fiber geometry. We also present the bend loss for both parallel-polarized and perpendicular-polarized modes with respect to the bend direction in the chalcogenide negative curvature fiber. In section 6.3, we study the avoided crossing during the resonant coupling between the core mode and the tube modes. Two non-degenerate core modes can be coupled to tube modes at the same bend radius. In section 6.4, we study the influence from the tube wall thickness on the resonant coupling. We find that a fiber with a larger tube wall thickness, corresponding to a smaller inner tube diameter, can sustain a smaller bend radius. In section 6.5, we study the bend loss when the relative angle between the bend direction and fiber orientation varies, since the bend direction is not always aligned with the fiber geometry in practice. The bend loss is sensitive to the bend direction when coupling occurs between the core mode and a tube mode. We summarize our results in section 6.6.

6.2 Geometry and Bend Loss

In this section, we introduce the geometric parameters of the negative curvature fiber. Figure 6.1 shows the full hollow-core negative curvature fiber geometry. The gray regions represent glass, and the white regions represent air. The inner tube diameter, d_{tube}, the core diameter, D_{core}, the tube wall thickness, t, and the minimum gap between the cladding tubes, g, are related by the expression: $D_{\mathrm{core}} = (d_{\mathrm{tube}} + 2t + g)/\sin(\pi/8) - (d_{\mathrm{tube}} + 2t)$. The core diameter, D_{core}, and the gap, g, are fixed at 150 μm and 10 μm, respectively. The wavelength is 5 μm in our simulation. We simulate As_2S_3 chalcogenide glass with a refractive index whose real part equals 2.4 and whose imaginary part equals 3.4×10^{-8} [183]. Negative curvature fibers have

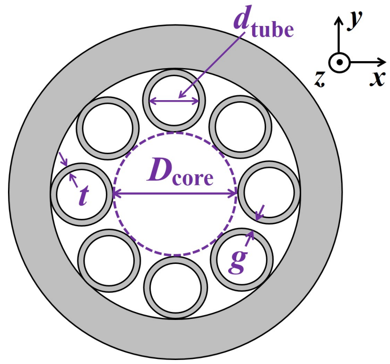

Figure 6.1. Cross section of a chalcogenide negative curvature fiber.

been drawn using 6 or 8 cladding tubes [49, 51, 55, 68, 78–80]. We use 8 cladding tubes in this chapter because negative curvature fibers with a smaller cladding tube diameter yield a lower bend loss [69].

We studied the bend loss using the above negative curvature fiber geometry. We assume that the bend is along the x-axis, and we take advantage of the reflection symmetry with respect to the $y = 0$ plane to only keep values for which $y > 0$ in the simulation [151]. A conformal transformation is used to replace the bent fiber with a straight fiber that has an equivalent index distribution: $n'(x, y) = n(x, y) \cdot \exp(x/R)$, where R is the bend radius [199, 200]. Figures 6.2(a) and 6.2(b) show the contour plot of the bend loss as a function of bend radius and tube wall thickness for the fundamental core modes that are polarized parallel and perpendicular to the bend direction, respectively. We observe that losses are consistently high for the tube wall thicknesses, t = 1.15 μm, 2.29 μm, and 3.44 μm, that satisfy the resonance condition, $t = m\lambda/[2(n_1^2 - n_0^2)^{1/2}]$, where n_1 and n_0 are respectively the real parts of the refractive indices of the glass and air [32, 34, 177]. We observe three transmission bands, I, II, and III, which are separated by the above tube wall thicknesses in both Figs. 6.2(a) and 6.2(b). In the following sections, we will study the bend loss with different polarizations, different tube wall thicknesses, and different bend directions.

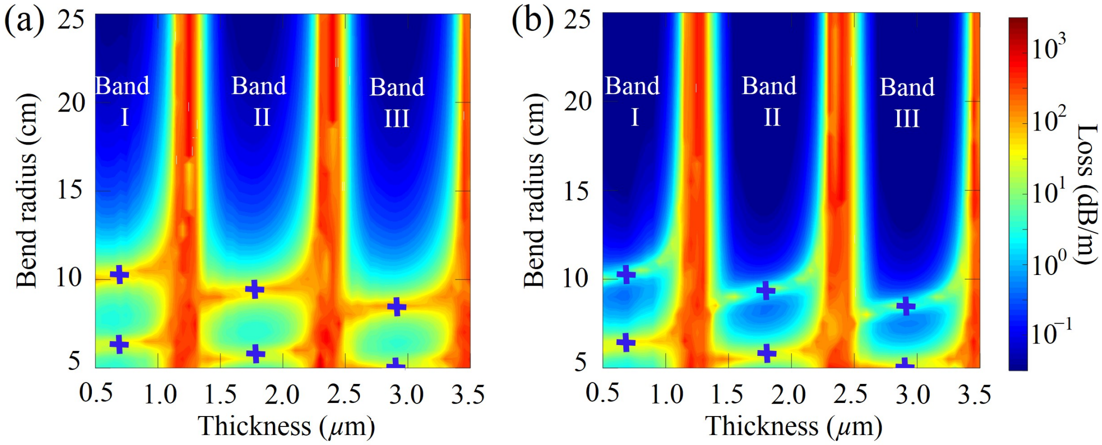

Figure 6.2: Bend loss of the fundamental mode that is polarized (a) parallel and (b) perpendicular to the bend direction as a function of the tube wall thickness and the bend radius. The plus signs denote points at which the loss becomes high relative to the bend-free loss even though the thickness is antiresonant.

6.3 Modes in Two Polarizations

In this section, we will compare the bend loss in two fundamental modes whose polarization directions are parallel or perpendicular to the bend direction. The tube wall thickness is fixed at 1.8 μm. Figure 6.3(a) shows the real parts of the effective indices of the parallel-polarized and perpendicular-polarized core modes, as the blue dashed curve and red solid curve, respectively. We can see that there are two avoided crossings at bend radii of 5.7 cm and 9.4 cm, and the index difference between the two polarized core modes is very small. Figure 6.3(b) shows the bend losses for core modes at different bend radii. There are two high loss peaks in the bend loss curves for both the parallel-polarized and perpendicular-polarized modes, which are consistent with the two avoided crossings shown in Fig. 6.3(a).

The mode structure at the two bend-loss peaks is different. Figure 6.4 shows both the parallel-polarized and perpendicular-polarized modes at bend radii of 5.7 cm and 9.4 cm, corresponding to the avoided crossings and the loss peaks in Fig. 6.3. We only show the mode in the middle of the avoided crossing; the evolution of the mode during the avoided crossing has been described in negative curvature fibers with 8 cladding tubes [70]. The color indicates the electric field intensity, normalized to its maximum. The arrows indicate the direction of the transverse electric field and the lengths of the arrows are proportional to the amplitude of the transverse electric field. We can see that, at a bend radius of 9.4 cm, coupling occurs between the core mode and the tube mode, which is located along the bend direction, as indicated by Figs. 6.4(b) and 6.4(d). The bend loss of the parallel-polarized mode is higher than the bend loss of the perpendicular-polarized mode as shown in Fig. 6.3(b). The

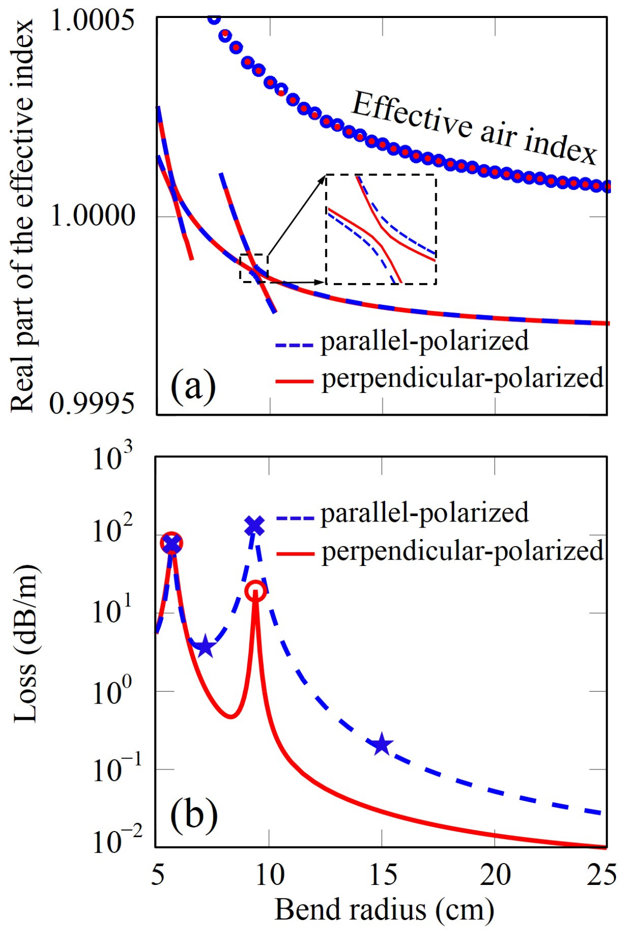

Figure 6.3: (a) Real parts of the effective indices and (b) bend losses for both parallel-polarized and perpendicular-polarized modes in the negative curvature fiber with a tube wall thickness of 1.8 μm. The inset shows the avoided crossing close to a bend radius of 9.4 cm. The effective air index is defined as the index after conformal transformation at the peak of the core mode intensity.

alignment of the core mode and the coupled tube mode is the same as the polarization direction for the parallel-polarized mode. Therefore, the coupling is stronger for the parallel-polarized mode and leads to a loss that is up to a factor of 6 higher than the loss of the perpendicular-polarized mode when the bend radius is 15 cm and is up to a factor of 28 higher when the bend radius is 10 cm. Since both parallel-polarized and perpendicular-polarized core modes are coupled to the same tube modes, avoided crossings and loss peaks occur at the same bend radius, as indicated by Fig. 6.3. At a smaller bend radius of 5.7 cm, the index in the tube along the bend direction is higher than the core index. Index matching occurs between the core mode and the tube mode in the tube at 45 degree with respect to bend direction or x-axis [83], as indicated by Figs. 6.4(a) and 6.4(c). In addition, since both the core modes in the two polarizations are coupled to the tube mode at 45 degree with respect to their polarization directions, those two non-degenerate modes have almost the same loss at the bend radius of 5.7 cm, as shown in Fig. 6.3(b).

In Fig. 6.5, we show the parallel-polarized modes at bend radii of 7.0 cm and 15.0 cm, corresponding to the two stars in Fig. 3(b). The modes are well-confined in the

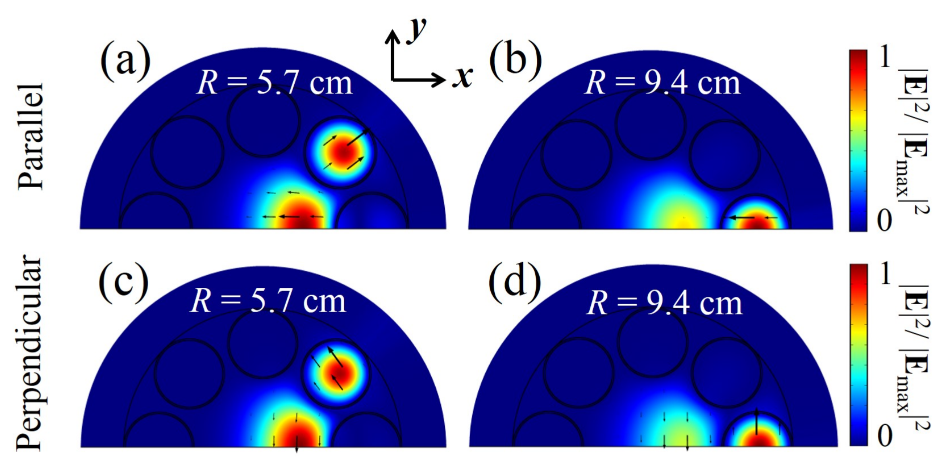

Figure 6.4: The parallel-polarized and perpendicular-polarized modes at bend radii of 5.7 cm and 9.4 cm. The contour plots represent the normalized electric field intensity, and the arrows represent the amplitude and direction of the transverse electric field.

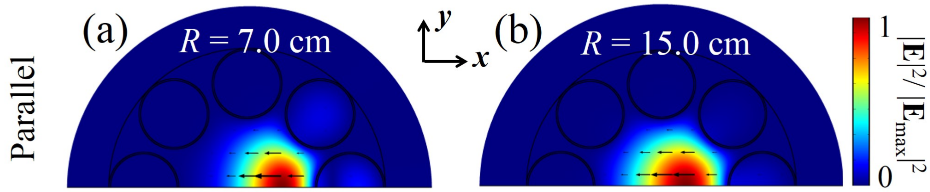

Figure 6.5: The parallel-polarized fundamental core modes at bend radii of (a) 7.0 cm and (b) 15.0 cm.

core. Conversely, coupling between the core and tube mode at the bend radius of 9.4 cm is visible in Fig. 6.4(b). Hence, the bend loss peaks in Fig. 6.3(b) are indeed induced by the mode coupling between the core and tube modes in the negative curvature fiber [69, 70].

We also note that some of the mode effective indices are higher than the refractive index ($n = 1.0$), which is due to the fiber bend. Figure 6.3(a) shows the effective air indices for the parallel-polarized and perpendicular-polarized modes as blue open circles and red dots, respectively. The effective air index is defined as the index after conformal transformation at the peak of the core mode intensity. The peak of the core mode intensity is not at the center of the core in the bent fiber, as shown in Fig. 6.5. Hence, the modes indicated by the blue dashed curve and the red solid curve in Fig. 6.3(a) have effective indices that are below the effective air index and are the fundamental core modes confined in the air core of the negative curvature fiber.

6.4 *Different Tube Thicknesses*

In Figs. 6.2(a) and 6.2(b), we see that besides the high loss that occurs at resonant tube thicknesses, there are in addition bend radii that lead to high loss, which are denoted by plus signs. In this section, we study these bend loss peaks for a fiber with different tube thicknesses [199]. In order to analyze the source of these high loss ranges, Figs. 6.6(a) and 6.6(b) show the real parts of the effective indices and bend

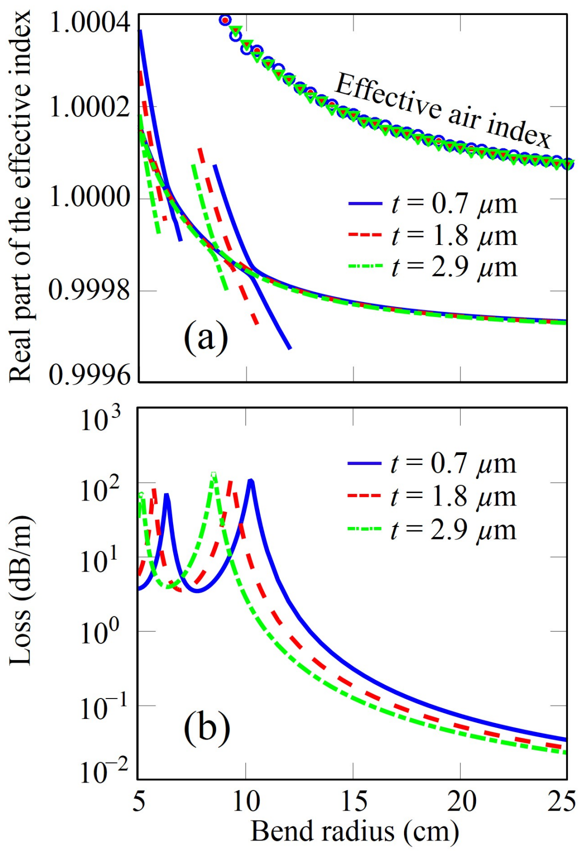

Figure 6.6: (a) Real parts of the effective indices and (b) bend losses for the parallel-polarized mode with tube wall thicknesses of 0.7 μm, 1.8 μm, and 2.9 μm.

losses, respectively, for the parallel-polarized mode with fixed tube wall thicknesses of 0.7 μm, 1.8 μm, and 2.9 μm. We present results for the parallel-polarized mode because it has a larger leakage loss than does the perpendicular-polarized mode. The real part of the effective index for the perpendicular-polarized mode is essentially the same as that for the parallel-polarized mode, and the bend loss exhibits peaks at the same bend radii as the parallel-polarized mode, although the loss peaks are lower. The avoided crossings are visible in Fig. 6.6(a). The loss peaks in Fig. 6.6(b) correspond to the high loss ranges in Fig. 6.2(a) that are marked by the plus signs. Note that the peak of the bend loss for fibers with a larger tube wall thickness occurs at a smaller bend radius, as shown in Fig. 6.6(b).

Mode coupling occurs when the effective indices of the core and tube modes match. In order to explain the results in Fig. 6.6, we study both the core mode and the tube modes when the tube wall thickness increases. The effective indices of the core modes with the same core diameter are almost the same even with different tube wall thicknesses. To predict the effective index of the tube mode, we ran additional simulations to find the mode in an annular core fiber [70], which contains just one ring of glass, as shown in Fig. 6.7. We study annular core fibers in two cases. For the first case, we use tube wall thicknesses of 0.7 μm, 1.8 μm, and 2.9 μm with a fixed inner tube diameter d_{in} of 75 μm. For the second case, we use tube wall thicknesses of 0.7 μm, 1.8 μm, and 2.9 μm with a fixed outer tube diameter d_{out} of 76.4 μm. The tube parameters of an inner tube diameter d_{in} of 75 μm and an outer tube diameter d_{out} of 76.4 μm correspond to the tube parameters in a straight negative curvature fiber using a core diameter of 150 μm, a tube wall thickness of 0.7 μm, and a minimum gap between the cladding tubes of 10 μm. In a fiber with a fixed inner tube diameter of 75 μm, the effective index increases slightly when the tube wall thickness increases

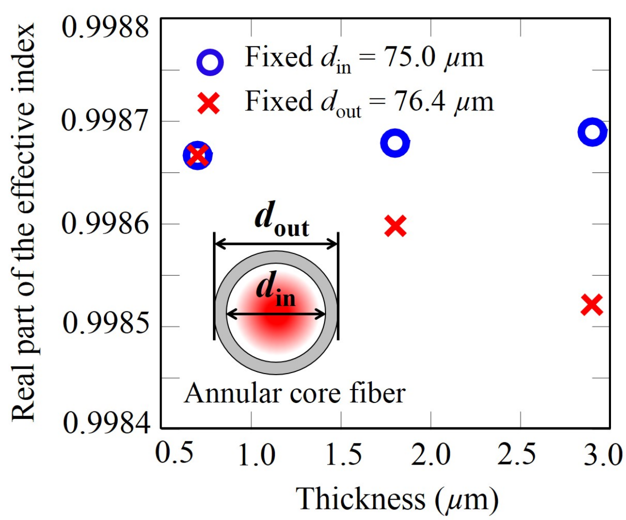

Figure 6.7: Real parts of the effective indices in annular core fibers with a fixed inner tube diameter or a fixed outer tube diameter. The inset shows the geometry of an annular core fiber.

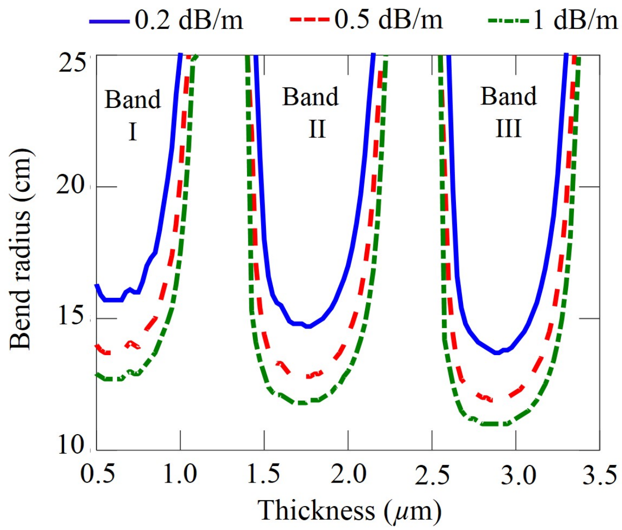

Figure 6.8: Minimum bend radius for the parallel-polarized mode as a function of tube wall thickness for given bend losses of 0.2 dB/m, 0.5 dB/m and 1.0 dB/m.

from 0.7 μm to 2.9 μm. In a fiber with a fixed outer tube diameter of 76.4 μm, the effective index decreases when the tube wall thickness increases from 0.7 μm to 2.9 μm. Hence, if one increases the tube wall thickness while the outer diameter of the tubes is fixed in a negative curvature fiber, the effective index of the tube mode decreases because the inner diameter of the tubes decreases. Bending effectively increases the effective index of certain tube modes. Hence, the avoided crossing and mode coupling occur at a smaller bend radius for the fiber with a larger tube wall thickness, corresponding to a smaller inner tube diameter, as shown in Figs. 6.6(a) and 6.6(b). This finding is consistent with research on negative curvature fibers in which more tubes are used [69]. The corresponding effective air indices in the fibers with tube wall thicknesses of 0.7 μm, 1.8 μm, and 2.9 μm are shown in Fig. 6.6(a) by blue circles, red dots and green triangles, respectively.

From Fig. 6.2(a), we can infer the minimum bend radius for a given loss. We then plot the minimum bend radius with respect to the tube wall thickness for given bend losses of 0.2 dB/m, 0.5 dB/m, and 1 dB/m for the parallel-polarized mode in Fig. 6.8. We again observe three transmission bands. As expected, a smaller loss requires a larger bend radius. The minimum bend radius for any given bend loss decreases as the transmission-band order increases in the parameter range we study here. Hence, a negative curvature fiber with a larger tube wall thickness can sustain a smaller bend radius. The reason is that the mode coupling in the fiber with a larger tube wall thickness, corresponding to a smaller inner tube diameter, occurs at a smaller bend radius, as we explained earlier. The bend loss is less than 0.2 dB/m in the transmission bands I, II, and III, corresponding to a loss value of 0.2 dB/turn if the fiber has a bend radius of 16 cm.

6.5 Different Bend Directions

Our previous simulations assumed that the bend direction is aligned with x-direction, as shown in Fig. 6.1 [65, 69, 199]. In practice, the bend can be in any direction. In this section, we will consider a bend direction with a relative angle, $\Delta\theta$, with respect to the x-direction. Since symmetry is broken, a full fiber geometry model has to be used in the simulation. The tube wall thickness is 1.8 μm. Figure 6.9(a) shows the bend losses for the two fundamental core modes as a function of the relative angle with respect to the x-axis at a bend radius of 9.4 cm, where the resonant coupling occurs. The loss is symmetrical about a bend relative angle of $\pi/8$ due to the fiber symmetry. When the bend relative angle changes from 0 to $\pi/8$, the leakage loss of the parallel-polarized mode, indicated by the blue dashed curve, and the perpendicular-polarized mode, indicated by the red solid curve, decrease by factors of 12 and 10, respectively. When the bend relative angle changes from 0 to $\pi/8$, the mode changes from being resonantly coupled to being slightly off resonance. Hence, the index matching condition is strongly affected by the relative angle, which leads to a large variation in the loss as the bend relative angle varies. The parallel-polarized mode profiles at relative angles of 0 and $\pi/8$ are shown in Figs. 6.10(a) and 6.10(c), respectively, at a bend radius of 9.4 cm. We see that the coupling between the core

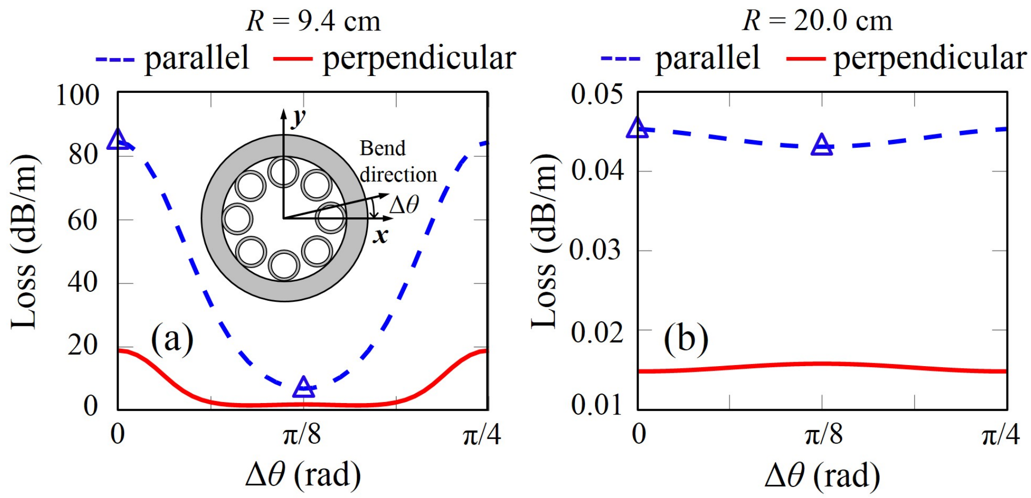

Figure 6.9: Bend losses of the parallel-polarized and perpendicular-polarized modes as a function of bend relative angle for the fibers with a tube wall thickness of 1.8 μm at bend radii of (a) 9.4 cm and (b) 20.0 cm. The inset shows the relative angle, $\Delta\theta$, between the bend direction and x-axis in the negative curvature fiber. The blue triangles mark the relative angles for the mode fields that are shown in Fig. 6.10.

mode and tube mode is strong at $\Delta\theta = 0$, and the coupling between the core mode and tube mode is weak at $\Delta\theta = \pi/8$.

Figure 6.9(b) shows the bend losses at different bend relative angles when the bend radius is 20.0 cm. The leakage losses of the two fundamental core modes only change within 7%, as the relative angle increases from 0 to $\pi/8$. It is because the fiber geometry is far from the coupling range between the core mode and tube modes at a bend radius of 20.0 cm. Changing the bend relative angle has almost no effect on the coupling condition. The corresponding mode profiles at relative angles of 0 and $\pi/8$ are shown in Figs. 6.10(b) and 6.10(d), respectively. The modes are well confined in the core, and there is not much difference in the mode profile except a rotational shift of $\pi/8$.

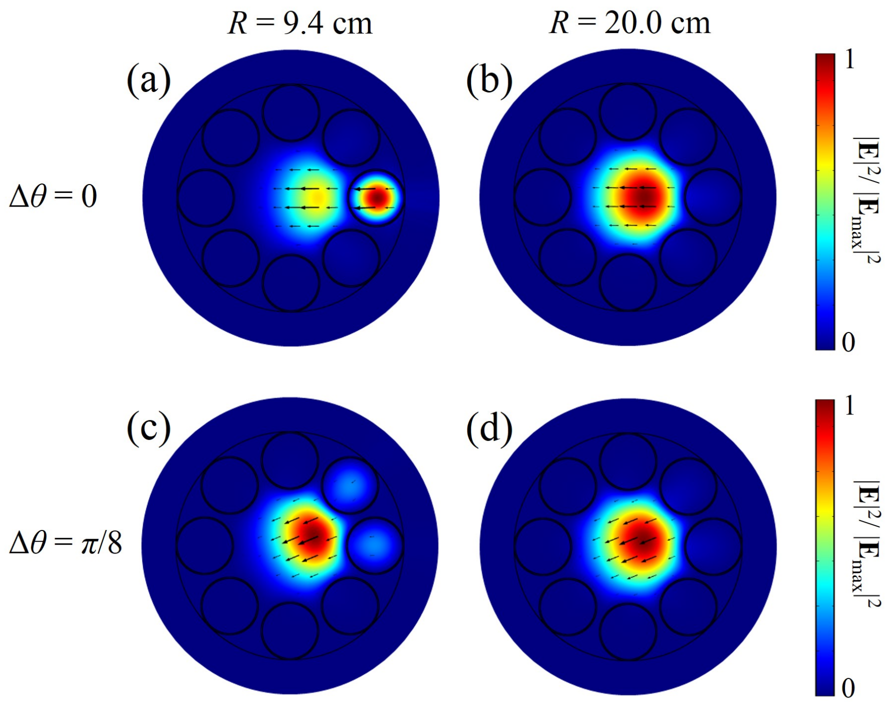

Figure 6.10: Parallel-polarized core mode at (a) $\Delta\theta = 0$ and (c) $\Delta\theta = \pi/8$ corresponds to the two triangles in Fig. 6.9(a) at a bend radius of 9.4 cm. The parallel-polarized core mode at (b) $\Delta\theta = 0$ and (d) $\Delta\theta = \pi/8$ corresponds to the two triangles in Fig. 6.9(b) at a bend radius of 20.0 cm.

6.6 Conclusion

In this chapter, we investigate the bending-induced loss for the two non-degenerate modes in chalcogenide glass negative curvature fibers. The bend loss peaks are induced by the resonant coupling between the core mode and tube modes. It is found that the parallel-polarized mode with respect to the bend direction experiences a higher bend loss than the perpendicular-polarized mode when the coupling occurs between the core mode and the tube mode along the bend direction. The difference between the losses of the two polarization modes is up to a factor of 28 with bend radii down to 10 cm. When coupling occurs between the core mode and the tube mode at 45 degree with respect to the bend direction, the bend losses in the parallel-polarized mode and perpendicular-polarized mode are almost the same. A fiber with a larger tube wall thickness, corresponding to a smaller inner tube diameter, can sustain a smaller bend radius due to the larger index difference between the core mode and tube mode. The bend loss changes by a maximum factor of 12 as the bend direction changes when the bend radius is 9.4 cm. The bend loss only changes by 7% as the bend direction changes when the bend radius is 20.0 cm. Hence, the bend loss is sensitive to the bend direction when coupling occurs between the core mode and tube modes. Overall, a bend loss of 0.2 dB/m at a bend radius of 16 cm, corresponding to 0.2 dB/turn, can be achieved in a chalcogenide negative curvature fiber at a wavelength of 5 μm. We conclude that polarization effects should be considered when designing fibers to withstand bend loss and polarization effect on bend loss.

Our study shows that the bend loss of the two polarization modes in negative curvature fibers can differ significantly. This differential bend loss could be used to make bending sensors [201, 202], in which the bend in the transverse direction is quantified by monitoring the losses in the two polarizations. Hence, negative curvature fibers are a good candidate for use in highly sensitive optical bending sensor systems.

CHAPTER SEVEN

Polarization-Filtering and Polarization-Maintaining Negative Curvature Fibers

This chapter published as [203]: C. Wei, C. Menyuk, and J. Hu, "Polarization-filtering and polarization-maintaining low-loss negative curvature fibers," Opt. Express **26**, 9528–9540 (2018).

In this chapter, we propose a polarization-filtering and polarization-maintaining negative curvature fiber in which two nested resonant tubes are added to a standard negative curvature fiber with one ring of tubes. The coupling between the glass modes in the nested resonant tubes and the fundamental core modes is used to increase the birefringence and differential loss for the fundamental core modes in the two polarizations. We show computationally that the birefringence and the loss ratio between the modes in the two polarizations can reach 10^{-5} and 850, respectively. Meanwhile, the low-loss mode has a loss that is lower than 0.02 dB/m. The relatively simple design of this polarization-maintaining negative curvature fiber will be useful in hollow-core fiber devices that are sensitive to polarization effects, such as fiber lasers, fiber interferometers, and fiber sensors.

7.1 Introduction

Polarization effects play an important role in many applications, such as optical communication networks, fiber lasers, fiber gyroscopes, and interferometric devices [204–208]. In optical fibers, fabrication imperfections and environmental perturbations, such as bending and twisting will introduce a random birefringence and lead to an unpredictable output [206, 209]. In fiber devices, unwanted birefringence will lead to different behavior in the two polarization eigenmodes [206], and mode competition between the two modes can lead to polarization instability [206]. To mitigate this effect, one can use polarization-maintaining fibers, in which the unpredictable polarization evolution is eliminated. These fibers have high birefringence, so that light propagates in only one polarization [208, 210]. Polarization effects are also used to make fast saturable absorbers in passively mode-locked fiber lasers [211–213]. When an intense optical pulse propagates in an optical fiber, the polarization state in the high-intensity peak will be different from the low-intensity wings, allowing the low-intensity wings to be attenuated by a polarization filter. Here, we show computationally that fiber devices that both filter and maintain the polarization can be implemented in negative curvature fibers, thereby enabling efficient and compact all-fiber devices.

Several polarization-maintaining negative curvature fiber structures have already been proposed. A straightforward approach by Vincetti and Setti [214] is to use a negative curvature fiber whose cladding is composed of an elliptical arrangement of cladding tubes. The birefringence in this case is always low when the wavelength is close to the center of the transmission windows [214]. Ding *et al.* [161] showed that high birefringence can be achieved in negative curvature fibers by using tubes with slightly different thicknesses in two transverse orthogonal directions. Mousavi *et al.* [215] proposed a structure that uses resonant and antiresonant tubes in two orthogonal directions to induce high birefringence. In this design, doubly-nested antiresonant tubes are required to confine the mode and achieve a low leakage loss.

In this chapter, we aim to design a relatively simple negative curvature fiber with a high birefringence and a high differential loss between the fundamental core modes in the two polarizations. We show two structures in the Fig. 7.1 to illustrate the main idea. Figure 7.1(a) shows a negative curvature fiber with two larger tubes in the y-direction, which are used to increase the birefringence and differential loss by coupling the fundamental core mode in one polarization to the tube mode, as indicated by the red-highlighted profile. Our simulation results show that the fundamental core modes in the x- and y-polarizations have similar effective indices even with an asymmetric core profile, which is consistent with other published results [150, 214, 215]. The tube modes in the x- and y-polarizations also have very similar effective indices. Coupling between the tube modes and the core modes in the two polarizations occurs within the same parameter range. Hence, this design leads to fibers with a small birefringence and a small differential loss between the fundamental core modes in the two polarizations.

Our goal is to find a fiber structure where the coupling between the cladding modes and the fundamental core modes in the two polarizations occurs within different parameter ranges. Figure 7.1(b) shows a negative curvature fiber structure with two nested tubes in the y-direction using a wall thickness close to the resonance condition. Negative curvature fibers with one nested tube in each major tube have been fabricated [62, 85, 216]. With proper design, the effective indices and mode profiles of the glass modes will be different for the x- and y-polarizations. The novelty in our design is the use of the coupling between the glass modes in the nested resonant tubes and the fundamental core mode to increase the birefringence and the differential loss between modes in two polarizations. The physics and mechanism for the proposed fiber design are different from those in previous works on polarization-maintaining negative curvature fibers [161, 215]. As long as all the major tubes are antiresonant, the loss for the other polarization is still low and comparable to the loss of standard negative curvature fibers with one ring of antiresonant tubes.

7.2 Geometry

Three mode types exist in negative curvature fibers: core modes, tube modes, and glass modes. Core modes reside primarily in central air-core of the fiber, while tube modes reside primarily in the air inside the cladding tubes. These modes are antiresonantly guided when the tube glass thickness, t, satisfies the antiresonance condition $t = (m - 0.5)\lambda/[2(n_1^2 - n_0^2)^{1/2}]$, where m equals any positive integer [43, 70].

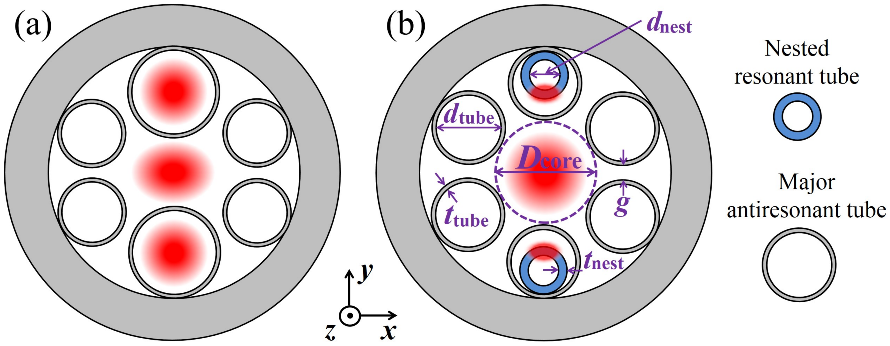

Figure 7.1: Schematic illustration of two negative curvature fibers with asymmetric geometries. Red-highlighted regions indicate locations where the mode intensity is high. (a) Coupling between the fundamental core mode and tube mode. (b) Coupling between the fundamental core mode and glass mode.

The glass modes are guided by glass, although they extend into the air. Because the guidance mechanism for glass and tube modes is different, the variation of their effective indices as the glass thickness changes is different. A slight change in the glass thickness leads to a large change in the effective index of the glass modes, while only slightly affecting the tube modes.

The geometry of the proposed polarization-maintaining negative curvature fiber is shown in Fig. 7.1(b). The two nested resonant tubes in the y-direction are represented by blue rings. The tube diameter, d_{tube}, the core diameter, D_{core}, the wall thickness of the major tube, t, and the minimum gap distance between the cladding tubes, g, are related by the expression: $D_{\text{core}} = d_{\text{tube}} + 2t + 2g$ for fibers with 6 major tubes [58, 141, 142, 150]. We simulate silica glass with a refractive index of 1.444 at a wavelength of 1550 nm for polarization-maintaining fibers [210, 215, 217]. The core diameter, D_{core}, is 50 μm, which is around 30 times larger than the transmission wavelength [49, 50, 58]. A major tube diameter of 30 μm is used throughout this chapter, unless otherwise indicated. The wall thickness of the major tubes, t, is 1.12 μm to satisfy the antiresonance condition, $t = (m - 0.5)\lambda/[2(n_1^2 - n_0^2)^{1/2}]$ where n_1 and n_0 are the refractive indices of the glass and air, λ is the light wavelength, and

m is the order of antiresonance [1,34]. We use the second antiresonance transmission band for which $m = 2$ with a glass thickness of 1.12 μm, corresponding to typical glass thicknesses that have been drawn in the past [82, 85]. A higher-order antiresonance implies a thicker tube wall, especially for shorter wavelengths, which makes fabrication easier. Geometries that use tube thicknesses corresponding to the first, second, or third antiresonance have similar minimum losses in the transmission band [141, 142].

7.3 Loss in the Two Polarization Modes

In standard negative curvature fibers with one ring of antiresonant tubes, the loss due to the surface scattering is two orders of magnitude lower than the confinement loss [43, 60] and is not taken into account in this work. We study the mode loss in the two polarizations for the geometry that is shown in Fig. 7.1(b). Coupling can be induced between the glass modes and the fundamental core modes in each

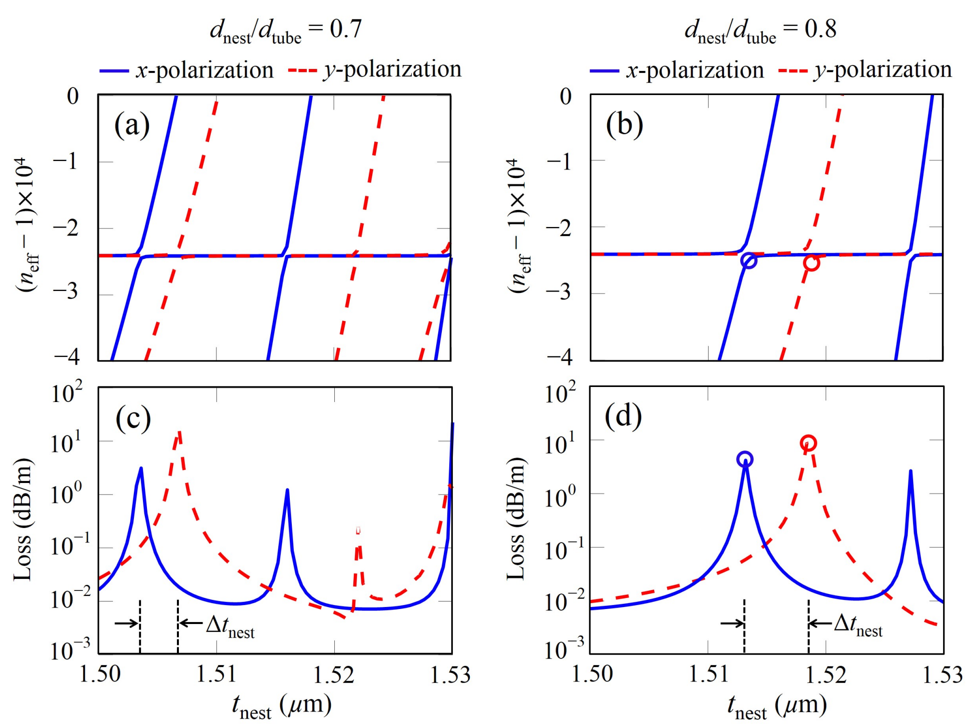

Figure 7.2: (a), (b) Effective index and (c), (d) loss of modes in the x- and y-polarizations as a function of t_{nest}. (a), (c) $d_{\text{nest}}/d_{\text{tube}} = 0.7$. (b), (d) $d_{\text{nest}}/d_{\text{tube}} = 0.8$.

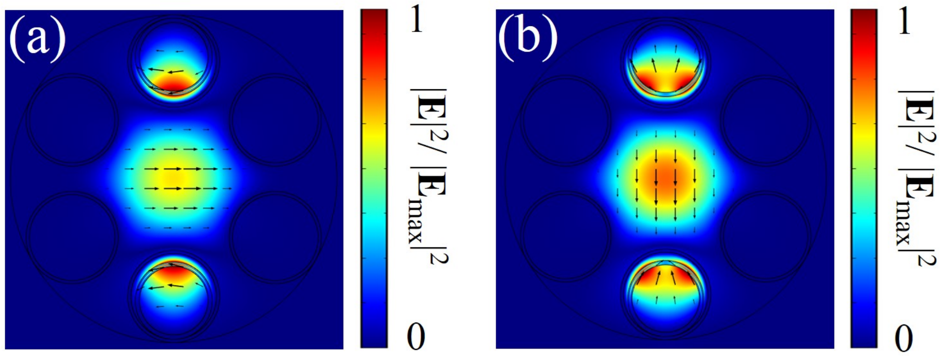

Figure 7.3: (a) Normalized mode intensity in the x-polarization at $t_{\mathrm{nest}} = 1.513$ μm and (b) normalized mode intensity in the y-polarization at $t_{\mathrm{nest}} = 1.519$ μm with $d_{\mathrm{nest}}/d_{\mathrm{tube}} = 0.8$, corresponding to the blue and red circles in Figs. 7.2(b) and 7.2(d).

of the two polarizations by tuning the wall thickness of the nested tubes. This new mechanism to induce high birefringence has not been used in previous designs of polarization-maintaining fibers. Figure 7.2(a) shows the effective index of the fundamental core modes in both the x- and y-polarizations as a function of the thickness of the nested tube, t_{nest}. The ratio of the nested tube diameter to the major tube diameter, $d_{\mathrm{nest}}/d_{\mathrm{tube}}$, is 0.7. There are several avoided crossings when the thickness of the nested tube increases from 1.50 μm to 1.53 μm near the resonance thickness, $t = m\lambda/[2(n_1^2 - n_0^2)^{1/2}]$, where the resonance order $m = 2$ is used. The corresponding losses are shown in Fig. 7.2(c). There are several high-loss peaks in the x- and y-polarizations, corresponding to the avoided crossings in Fig. 7.2(a). The avoided crossings or high-loss peaks of the modes in the x- and y-polarizations occur at different nested tube thicknesses, t_{nest}. The difference between the nested tube thicknesses of the x- and y-polarizations at the first high-loss peaks is denoted by Δt_{nest} in Fig. 7.2(c). We show similar plots of the effective index and loss in Figs. 7.2(b) and 7.2(d), where the ratio of the nested tube diameter to the major tube diameter, $d_{\mathrm{nest}}/d_{\mathrm{tube}}$, is 0.8. The difference between the nested tube thicknesses, Δt_{nest}, in the fiber using $d_{\mathrm{nest}}/d_{\mathrm{tube}} = 0.8$ is larger than that in the fiber using $d_{\mathrm{nest}}/d_{\mathrm{tube}} = 0.7$.

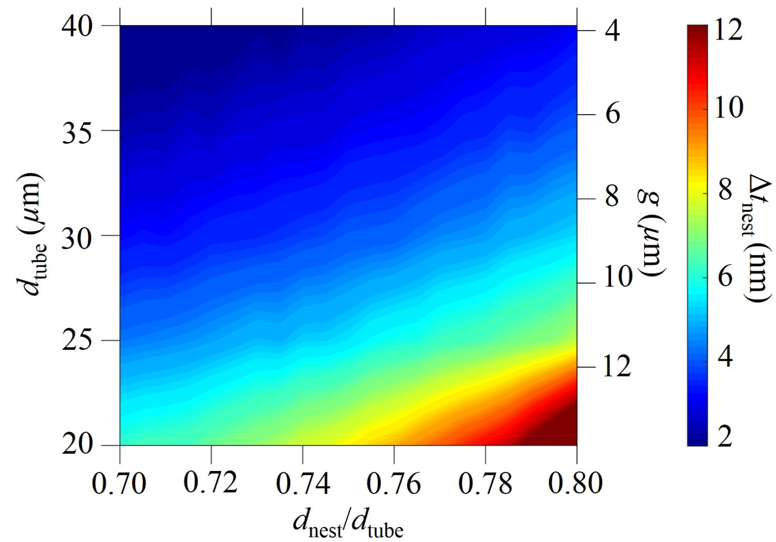

Figure 7.4: Contour plot of Δt_{nest} as a function of d_{tube} and $d_{\text{nest}}/d_{\text{tube}}$. The corresponding gap, g, is also marked on the right side of the contour plot.

The mode fields in the coupling region are shown in Fig. 7.3, corresponding to the high-loss peaks in the x- and y-polarizations, denoted by blue and red circles in Fig. 7.2(d). The wavelength is 1550 nm. The color indicates the electric field intensity, normalized to its maximum. The arrows indicate the direction of the transverse electric field and the lengths of the arrows are proportional to the amplitude of the transverse electric field. For the mode in the x-polarization shown in Fig. 7.3(a), the core mode couples with the glass mode, which has a maximum at one point in both nested tubes. For the mode in the y-polarization shown in Fig. 7.3(b), the core mode couples with the glass mode, which has a maximum at two points in both nested tubes.

7.4 Structure Optimization

Figures 7.2 and 7.3 show coupling between the glass modes and the fundamental core modes. When the coupling is strong, there is a high differential loss between the fundamental core modes in the x- and y-polarizations. Due to uncertainty in the fiber drawing process, it is desirable to design a fiber with the largest possible separation,

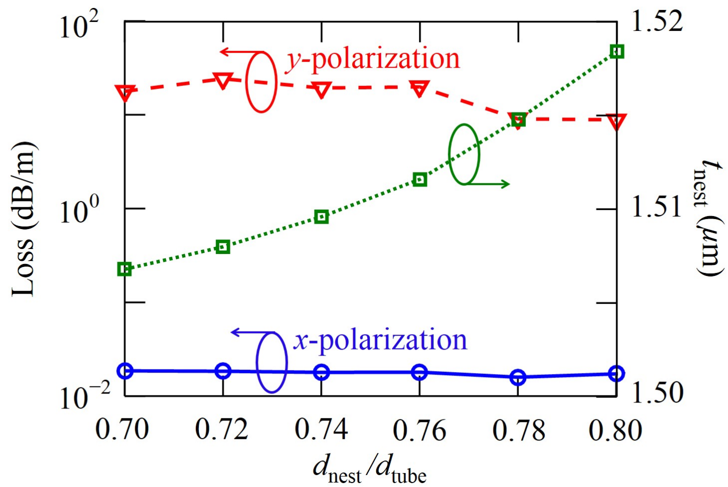

Figure 7.5: Loss of modes in the x- and y-polarizations and the thickness of the nested tube, t_{nest}, when the glass mode and the core mode in the y-polarization are resonantly coupled. The diameter of the major tube, d_{tube}, is 30 μm.

Δt_{nest}, in order to increase the fabrication tolerance. Here, we study the impact on the parameter Δt_{nest} from the major tube diameter, d_{tube}, and the ratio of the nested tube diameter to the major tube diameter, $d_{\text{nest}}/d_{\text{tube}}$. We show a contour plot of the parameter Δt_{nest} in Fig. 7.4. The wavelength is 1550 nm. Each value of Δt_{nest} on the contour plot is obtained from the leakage loss curves of the modes in the x- and y-polarizations as a function of nested tube thickness, t_{nest}, that is shown in Fig. 7.2. Figure 7.4 shows that the parameter Δt_{nest} increases when the tube diameter, d_{tube}, decreases or the ratio of the nested tube diameter to major tube diameter, $d_{\text{nest}}/d_{\text{tube}}$, increases. Hence, a fiber with a smaller major tube diameter and a larger nested tube diameter yields a larger Δt_{nest}. A stronger interaction between nested and major tubes leads to a larger separation Δt_{nest} because the mode intensity in the nested tubes reaches its maximum at different locations for the two polarizations, as shown in Figs. 7.3(a) and 7.3(b). We use a maximum $d_{\text{nest}}/d_{\text{tube}}$ of 0.8 since it may be difficult to fabricate a fiber with $d_{\text{nest}}/d_{\text{tube}} > 0.8$. A small gap between the nested and major tubes may collapse in the fiber drawing process.

Figure 7.5 shows the loss of the fundamental core modes in the x- and y-polarizations as a function of $d_{\text{nest}}/d_{\text{tube}}$ when the glass mode and the fundamental core mode are resonantly coupled in the y-polarization. The corresponding thickness of the nested tube, t_{nest}, is also plotted using a green dotted curve. The diameter of the major tube, d_{tube}, is fixed at 30 μm. Setting $d_{\text{nest}}/d_{\text{tube}} = 0.8$ in order to maximize Δt_{nest}, we find that $t_{\text{nest}} = 1.519$ μm. This value corresponds to the red circles in Figs. 7.2(b) and 7.2(d). When $d_{\text{nest}}/d_{\text{tube}}$ is between 0.7 and 0.8, the loss of the x-polarization is below 0.02 dB/m. The loss ratio of the y-polarization to the x-polarization is more than 500 within the parameter range that we show in Fig. 7.5.

We also carried out additional simulations to compare the results of fibers using six, eight, and ten cladding tubes. For all these fibers, we set the core diameter, tube wall thickness, and wavelength equal to 50 μm, 1.12 μm, and 1.55 μm, respectively. The tube diameters are 30 μm, 25 μm, and 15 μm in the fibers with six, eight, and ten cladding tubes, respectively. Different thicknesses of the nested tube are selected to give the maximum birefringence. Figure 7.6(b) shows the birefringence as a function of the maximum distance, z, between the major antiresonant tube and the nested resonant tube. The birefringence in these three fibers are on the same scale. The birefringence increases when z decreases; when z is smaller, a stronger interaction between nested and major tubes leads to a larger birefringence. Figure 7.6(c) shows the loss in both the x- and y-polarizations. The loss of the x-polarization is between 10^{-2} dB/m and 10^{-1} dB/m, which is more than two orders of magnitude lower than the loss of the y-polarization.

We also ran additional simulations for different structures to compare their performance to the performance of our fiber design, shown in Fig. 7.1(b). Fibers with different tube wall thickness corresponding to the first and the second antiresonance bands have a similar loss ratio and birefringence. Fibers in which antiresonant tubes are added in the four major tubes in the x-direction show a lower minimum loss in

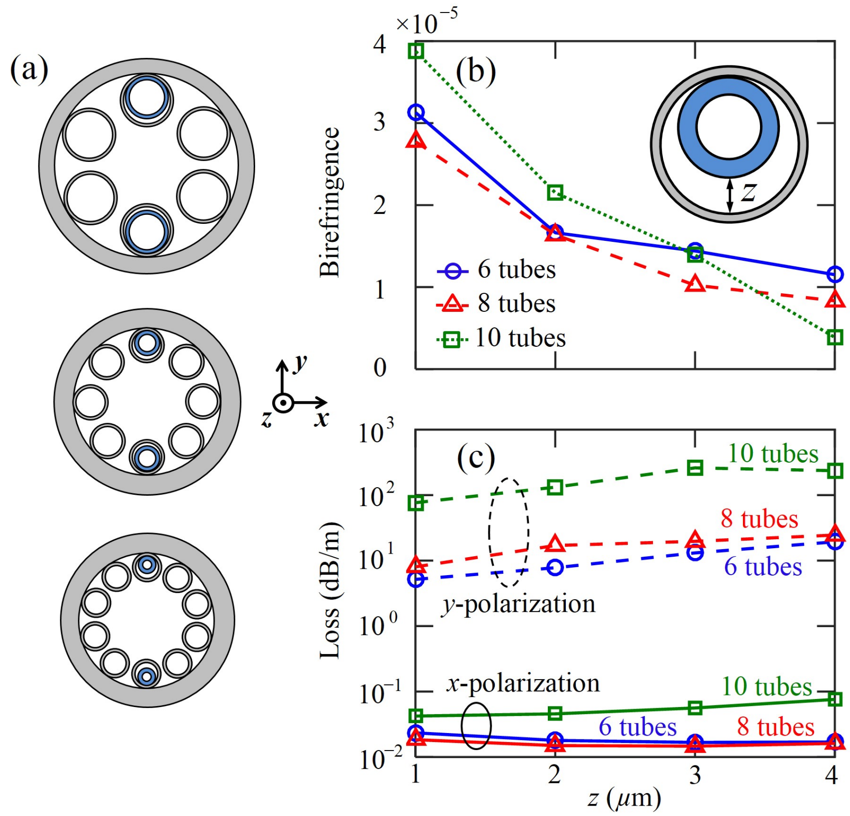

Figure 7.6: (a) Schematics illustration, (b) birefringence, and (c) loss of negative curvature fibers with six, eight, and ten cladding tubes. Inset in (b) shows a schematic illustration of the maximum distance, z, between the major antiresonant tube and the nested resonant tube.

x-polarization and a similar birefringence. Fibers that are modified by removing the nested resonant tubes in the y-direction and adding four nested resonant tubes in the x-direction have a low loss ratio between the two polarization modes.

7.5 Comparison of Polarization-Maintaining Negative Curvature Fibers

In this section, we study the performance of the fiber as a function of wavelength. The ratio of the nested tube diameter to the major tube diameter, $d_{\mathrm{nest}}/d_{\mathrm{tube}}$, is 0.8, and the thickness of the nested tube, t_{nest}, is 1.519 μm, based on Fig. 7.2. Figures 7.7(a) and 7.7(b) show the effective index and the leakage loss of the modes in the x- and y-polarizations as a function of wavelength. There is a high-loss peak in

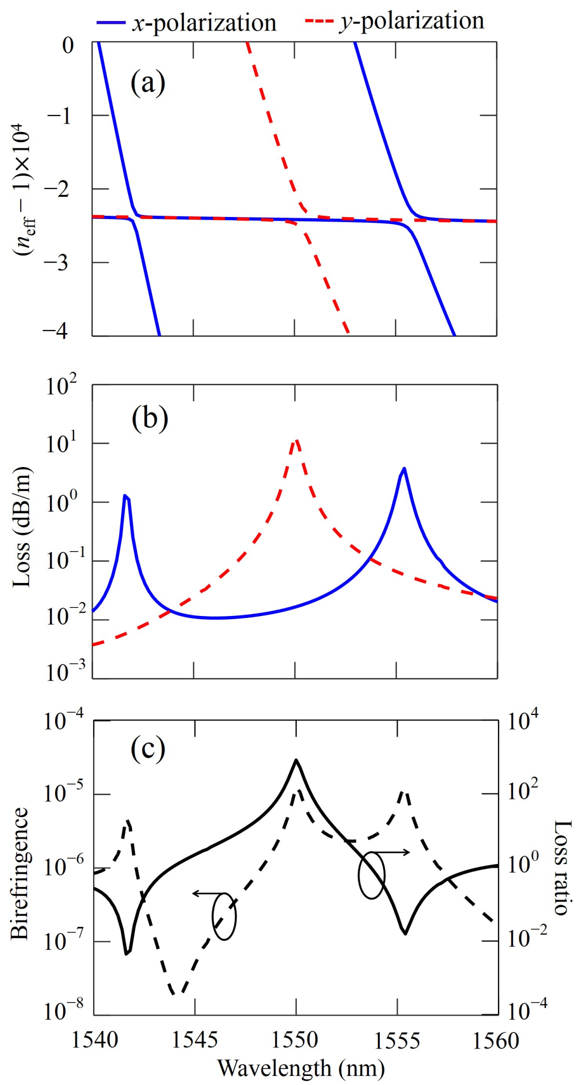

Figure 7.7: (a) Effective index, (b) loss, (c) birefringence, and loss ratio as a function of wavelength.

the y-polarization at the wavelength of 1550 nm between the two high-loss peaks in the x-polarization. The loss of the mode in the x-polarization is less than 0.02 dB/m when the wavelength is 1550 nm. Figure 7.7(c) shows the birefringence and loss ratio of the mode in the y-polarization to the mode in the x-polarization, which can reach 10^{-5} and 850, respectively, at a wavelength of 1550 nm. This fiber has a bandwidth of 1.5 nm for a loss ratio higher than 100 and a bandwidth of 4.7 nm for a loss ratio higher than 10, which can be used for polarization-filtering in a fiber laser [218, 219].

The narrow bandwidth will automatically select the specific wavelength in a fiber laser loop.

In Table 7.1, we show a performance comparison between the results in this chapter and other simulations of polarization-maintaining negative curvature fibers, including loss, the loss ratio between the two polarization modes, the number of cladding tubes, the maximum number of layers in the azimuthal direction, the core shape, and birefringence. In some cases, half tubes are used in the geometry [161]. We write the number of tubes in the format of $p(1) + q(1/2)$, where p represents number of full tubes and q represents number of half tubes. The maximum number of antiresonant or resonant layers in any azimuthal direction is specified since a simple structure with fewer layers is easier to fabricate. Currently, nested negative curvature fibers, which have been fabricated, only have at most two glass layers in any azimuthal direction [62, 85, 216]. The fiber core shape is also compared because a circular core shape is easier to draw due to surface tension in the fiber drawing process. The fiber design that we propose in this chapter only has two glass layers in any azimuthal direction and has a circular core shape. The proposed design has a relatively low leakage loss and a high loss ratio between the two polarization modes. Although the birefringence in our proposed structure is lower than in other fiber designs in Table 7.1, these other designs require either three glass layers in any azimuthal direction or a non-circular core shape. The feasibility of fabricating these more complex structures has not yet been demonstrated [62, 85, 216].

A commonly used approach to obtain fast saturable gain in passively mode-locked lasers is to combine nonlinear polarization rotation with a polarization filter [211–213]. In this approach, the nonlinear polarization rotation and the polarization filtering using a polarizer are usually implemented separately [211–213]. Our fiber design makes it possible to combine the nonlinear polarization rotation and polarization filtering in one device by splicing a standard fiber with our proposed fiber design,

Table 7.1. Performance comparison between simulation results from different fiber designs

	Ref. [214]	Ref. [161]	Ref. [215]	Our work
Loss	0.04 dB/m	0.34 dB/m	0.04 dB/m	0.02 dB/m
Loss ratio	$\sim$2	$\sim$10	1×10^3	850
# of tubes	8(1) + 0(1/2)	0(1) + 12(1/2)	12(1) + 0(1/2)	8(1) + 0(1/2)
Max. # of layers	1	3	3	2
Core shape	Ellipse	Circle	Circle	Circle
Birefringence	$< 7 \times 10^{-5}$	1×10^{-4}	1.5×10^{-4}	1.3×10^{-5}

and thus enable lower-loss and more efficient fiber laser designs. The fusion splice between tapered negative curvature fibers and step-index fibers has been reported to have a total insertion loss of less than 0.5 dB [101].

7.6 Conclusion

In this chapter, we propose a polarization-filtering and polarization-maintaining negative curvature fiber that includes two nested resonant tubes. The coupling between the glass modes in the nested resonant tubes and the fundamental core modes is used to increase the birefringence and the differential loss between the fundamental core modes in the two polarizations, while one polarization mode still has low loss. The low-loss mode has a leakage loss that is less than of 0.02 dB/m, and the loss ratio between the fundamental core modes in the two polarizations can reach 850. The physics and mechanism for the proposed fiber design are different from those in previous works on polarization-maintaining negative curvature fibers. The proposed design contains at most two glass layers, which has been demonstrated to be feasible to fabricate. This relatively simple design of polarization-filtering and polarization-maintaining low-loss negative curvature fibers will be useful in systems that require a polarization filter that can be integrated with other optical fibers.

CHAPTER EIGHT

Future Prospects and Summary

This chapter published as part of [1]: C. Wei, R. J. Weiblen, C. R. Menyuk, and J. Hu, "Negative curvature fibers," Adv. Opt. Photon. **9**, 504–561 (2017).

8.1 Future Prospects

Due to their ability to transmit light with low loss over a broad bandwidth and with low fiber nonlinearity, negative curvature fibers have many potential applications [220, 221]. We expect extensive research to continue in future years in the areas of data communications, power delivery, nonlinear optics, chemical sensing, bend sensing, as well as mid-IR, ultraviolet (UV), and THz transmission.

In data communications, conventional step-index fibers provide large transmission bandwidth and low transmission loss. However, light propagates about 30% slower in a silica glass fiber than in the vacuum. Air guidance in hollow-core fiber can reduce fiber latency significantly [204, 222]. Additionally, the wavelength-division multiplexing (WDM) bandwidth in a step-index fiber is limited by material absorption. High transmission capacity of 1.48 Tbit/s and 24 Tbit/s has been demonstrated using hollow-core photonic bandgap fibers [204, 223]. In photonic bandgap fibers, the effective index of the core mode must be inside the frequency range of the bandgap so that the bandwidth is smaller than the bandwidth of negative curvature fibers [43, 60]. A negative curvature fiber can significantly increase the data bandwidth of an optical fiber interconnect if the fiber can achieve suitably low loss [52, 141]. A combination of low loss and wide bandwidth in negative curvature fibers may play a key role in high-capacity data transmission [60].

In negative curvature fibers, most of the power is located in air, which does not contribute to the nonlinearity. Energy damage thresholds of 3.2 mJ and 5 mJ were measured using lasers at a wavelength of 1064 nm and a pulse duration of 9 ns [54, 123]. Transmission of 30 mJ pulses was also reported using lasers at a wavelength of 1064 nm and a pulse duration of 30 ns [224]. Such a high damage threshold will enable new applications requiring high power delivery, such as cutting, welding, and engraving [54, 225]. Dispersion was also studied in negative curvature fibers for high-energy femtosecond pulse delivery [100, 226, 227]. Low dispersion was obtained in hypocycloid-shaped kagome fibers with different silica thicknesses [100]. A low dispersion slope was also found in negative curvature fibers because of strong field localization in the air core in a femtosecond pulse transmission experiment [226]. Negative curvature fibers with low dispersion and nonlinearity can also deliver the light for multiphoton microscopy, where optical pulses with an ultrashort duration and a broad wavelength range are required to efficiently excite a diverse range of fluorophores [228].

The ability of negative curvature fibers to deliver high power makes it possible to do nonlinear optics experiments in fiber cores that are filled with gases, vapors, and plasmas, which is not possible using conventional fibers based on total internal reflection [25, 229–234]. Gas-filled negative curvature fibers are particularly suited for ultrafast nonlinear fiber optics because of their ability to guide high intensity light due to their high glass damage threshold, as explained in Ref. [84]. Supercontinuum generation in the UV and mid-IR regions has been studied using gas-filled negative curvature fibers [235, 236]. In addition, experiments can be carried out using different gases in negative curvature fibers, leading to different gas-filled fiber laser sources. Mid-IR gas-filled kagome fiber lasers have been made using C_2H_2, NCH, and I_2 [92, 94, 237, 238]. Stimulated Raman scattering has been demonstrated in a 1-meter-long hollow-core photonic crystal fiber filled with hydrogen gas [25]. Experiments using negative curvature fibers filled with ethane and hydrogen gases have demonstrated efficient 1.5 μm, 1.9 μm, and 4.4 μm emission from stimulated Raman scattering [103, 239–244]. Three-octave spectral comb, spanning wavelengths from 325 nm to 2300 nm, has been generated and guided, using a hydrogen-filled hollow-core photonic crystal fiber [30]. A hypocycloid-shaped kagome fiber filled with hydrogen was also used to generate Raman comb, which spans from 370 nm to 1150 nm covering the whole visible wavelength range [245]. Soliton-plasma interactions have also been studied in a gas-filled kagome hollow-core PCF and negative curvature fibers [233, 246]. High power transmission in negative curvature fibers can also be used for pulse compression [226, 247–250].

Liquid-filled and gas-filled hollow-core PCFs can provide strong light confinement, an enhanced reaction rate, and a long interaction length for chemical sensing experiments [27, 251–254]. Low-loss liquid-filled photonic bandgap fibers have an intrinsic limitation due to a narrow transmission window, which makes Raman or fluorescence spectroscopy experiments difficult [81]. The micron-scale hole size can make the liquid filling process time-consuming, especially for large clusters or viscous liquids [81]. In addition, enlarging the core size in photonic bandgap fibers for the same operational wavelength requires removing additional elements from the core and adds complexity to the fabrication procedure [43, 255]. In negative curvature fibers, core scaling can happen with no additional fabrication complexity [43]. The larger tubes in negative curvature fibers make the liquid filling procedure easier [81, 251]. Gas sensing of acetylene, hydrogen cyanide, methane, and ammonia have been demonstrated in hollow-core bandgap fibers [253, 256–259]. By appropriately choosing the photonic crystal fiber parameters, high-sensitivity gas detection should be possible. Since the absorption region of most gases is at mid-IR wavelengths, the ability of negative curvature fibers to transmit light in the mid-IR makes them attractive for gas-sensing applications.

The bend loss of the two polarization modes in negative curvature fibers can differ significantly, as shown in Chapter 6 [150]. This differential bend loss could be used to make bending sensors [201,202], in which the bend in the transverse direction is quantified by monitoring the losses in the two polarizations. Hence, negative curvature fibers can be used in highly sensitive optical bending sensor systems.

Negative curvature fibers are promising for applications in different wavelength ranges, including the UV, visible, IR, and THz ranges. Infrared fibers have become increasingly prominent in a variety of scientific disciplines and technological applications, such as chemical sensing, environmental monitoring, homeland security, and medical diagnostics [75, 260, 261]. In standard silica fibers, light does not propagate beyond 2 μm. Thus, nonsilica glasses must be used for infrared applications [75]. In negative curvature fibers, only a small amount of power overlaps with the glass region. Hence, the material loss in the glass has only a limited impact on the propagation loss, which is the reason that negative curvature fibers made of silica can still have low loss in the mid-IR region at wavelengths of 3.4 μm and 4.0 μm [51, 52]. Theoretical research shows that, at wavelengths shorter than 4.5 μm, silica negative curvature fibers have a leakage loss that is around or below 0.1 dB/m and are preferable to chalcogenide fibers [142]. At wavelengths longer than 4.5 μm, it is preferable to use As_2S_3 chalcogenide or As_2Se_3 chalcogenide negative curvature fibers since their leakage loss is one or more orders of magnitude lower than the loss of silica negative curvature fibers [142]. The development of hollow-core chalcogenide fibers has been hampered by fabrication difficulties [79]. Negative curvature fibers have a simpler structure than photonic bandgap fibers, which makes it easier in principle to fabricate them [55, 77]. We expect to see more research on negative curvature fibers using non-silica glasses.

The UV regime has turned out to be of essential importance for a vast number of applications, such as Raman microscopy [262–264], photochemistry [252], and lithography [265]. The small overlap with the glass region will make it possible to use negative curvature fibers in UV applications [105, 114].

THz transmission has been studied in tube lattice fibers [83, 110, 111, 266–268], kagome fibers [269], Bragg fibers [270], thin-wall pipe waveguides [132,133,271], photonic bandgap fibers [272], and antiresonant fibers [273, 274]. Guiding the electromagnetic radiation inside a hollow-core fiber is helpful in reducing the propagation loss in this case. A THz spectroscopy and imaging system has been demonstrated using a polymer hollow-core negative curvature fiber [275]. We expect that negative curvature fibers will be used in more THz [276] and spectroscopy [277] applications.

Polarization-maintaining (PM) fiber is a specialty fiber with a strong built-in birefringence. Such fiber is used in applications where preserving polarization state in transmission is essential. Research shows that the birefringence is small in negative curvature fibers whose cladding is composed by an elliptical arrangement of circular dielectric tubes [214]. In particular, the birefringence is always low when the wavelength is close to the center of the transmission windows [214]. Higher birefringence and differential loss can be achieved in negative curvature fibers with more additional nested tubes using different thicknesses in the core boundary [161, 215, 278].

Most of the theoretical study on hollow-core photonic crystal fibers uses ideal structures, which provides a good reference for the experiment. In experiments, structural distortions have significant impact on fiber properties such as bandwidth and leakage loss. The properties of air-core photonic bandgap fibers depend sensitively on the structural parameters [279–281]. The main reason is that the confinement in photonic bandgap fibers requires a periodic cladding. Any distortion of the structure in the cladding region will affect the periodic bandgap structure. In negative curvature fibers, theoretical results show that tube diameter and glass thickness may play a noticeable role on the fiber loss [60, 62, 282]. Variations in these perturbations along the longitudinal axis of the fiber could significantly increase the loss over a wide bandwidth [282]. More effort in the theoretical study of cladding imperfections will lead to a better understanding of the requirements for fiber drawing.

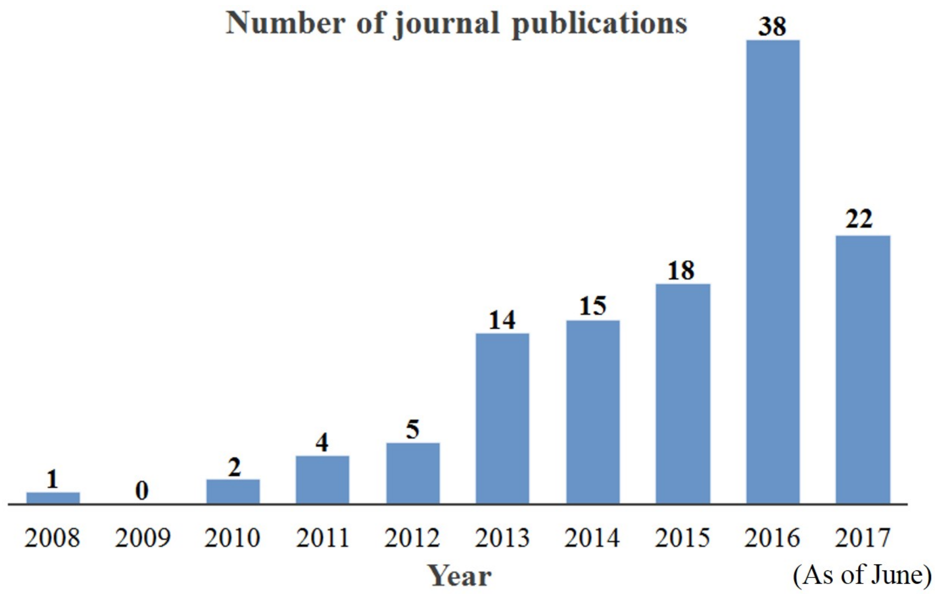

Figure 8.1: Number of journal publications in the references of this dissertation related to hollow-core fibers that use a negative curvature inner core boundary.

8.2 Summary

Negative curvature fibers have drawn much attention in recent years. Figure 8.1 shows the number of journal articles in the references of this dissertation related to hollow-core fibers that use a negative curvature inner core boundary. Steady growth over the years indicates the growing interest in this field. Due to the fabrication complexity, only a handful of groups are able to fabricate photonic bandgap fibers. On the contrary, due to their relative simplicity, more groups can fabricate negative curvature fibers consisting of one ring of tubes [283].

In this dissertation, we show simulation results for the mode properties and the transmission loss in slab waveguides, annular core fibers, and negative curvature fibers. The geometries with glass thicknesses corresponding to antiresonance have low leakage loss. The leakage loss in negative curvature fibers is three orders of magnitude lower than the leakage loss in annular core fibers due to the negative curvature in the core boundary. The effect of negative curvature leads to a lower loss in negative curvature fibers [64,197,284–286] by inhibiting coupling between the fundamental core mode and the cladding modes [37, 57]. There are two elements that are needed to obtain low loss. First, the overlap between the approximate modes must be small. Antiresonance helps make that happen. Second, one must use a fiber structure, in which the wavenumber of the approximate fundamental core mode is not matched to any of wavenumbers of the approximate cladding modes. No matter how small the overlap is, the approximate modes will always couple strongly when the wavenumbers match. The combination of antiresonance in the glass at the core boundary and a wavenumber mismatch with the cladding modes has led to remarkably low loss in negative curvature fibers.

We have described recent advances in negative curvature fibers, including comparison of loss in silica and chalcogenide negative curvature fibers, impact of cladding tubes in chalcogenide negative curvature fibers, higher-order mode suppression in chalcogenide negative curvature fibers, bending-induced mode non-degeneracy and coupling in chalcogenide negative curvature fibers, and polarization-filtering and polarization-maintaining low-loss negative curvature fibers.

The advances in the negative curvature fibers enable a large range of applications, including mid-IR fiber lasers, micromachining, and surgery. Negative curvature fibers will be the best choice for a wide range of different applications because of their combined advantages of low loss, broad bandwidth, and a low power ratio in the glass.

[1] C. Wei, R. J. Weiblen, C. R. Menyuk, and J.Hu, “Negative curvature fibers,” Adv. Opt. Photon. **9**, 504–561 (2017).

[2] P. V. Kaiser and H. W. Astle, “Low-loss single-material fibers made from pure fused silica,” Bell Syst. Tech. J. **53**, 1021–1039 (1974).

[3] J. D. Joannopoulos, S. G. Johnson, J. N. Winn, and R. D. Meade, Photonic crystals: molding the flow of light (Princeton university press, 2011).

[4] E. Yablonovitch, “Inhibited Spontaneous Emission in Solid-State Physics and Electronics,” Phys. Rev. Lett. **58**, 2059–2062 (1987).

[5] S. John, “Strong localization of photons in certain disordered dielectric superlattices,” Phys. Rev. Lett. **58**, 2486–2489 (1987).

[6] J. C. Knight, T. A. Birks, P. St. J. Russell, and D. M. Atkin, “Pure silica single-mode fiber with hexagonal photonic crystal cladding,” in *Conference on Optical Fiber Communications* (Optical Society of America, 1996), postdeadline paper PD3.

[7] J. C. Knight, T. A. Birks, P. St. J. Russell, and D. M. Atkin, “All-silica single-mode optical fiber with photonic crystal cladding,” Opt. Lett. **21**, 1547–1549 (1996).

[8] T. A. Birks, J. C. Knight, and P. St. J. Russell, “Endlessly single-mode photonic crystal fiber,” Opt. Lett. **22**, 961–963 (1997).

[9] N. W. Aschcroft and N. D. Mermin, Solid State Physics (Saunders College, Philadelphia, 1976).

[10] S. L. Altmann, Band Theory of Solids: An Introduction from the Point of View of Symmetry (ClarendonPress, 1994).

[11] F. Couny, F. Benabid, P. J. Roberts, M. T. Burnett, and S. A. Maier, “Identification of Bloch-modes in hollow-core photonic crystal fiber cladding,” Opt. Express **15**, 325–338 (2007).

[12] F. Benabid and P. J. Roberts, “Guidance mechanisms in hollow-core photonic crystal fiber,” Proc. SPIE 6901, Photonic Crystal Materials and Devices VII, 69010U (January 28, 2008).

[13] F. Zolla, G. Renversez, A. Nicolet, B. Kuhlmey, S. Guenneau, D. Felbacq, A. Argyros, and S. Leon-Saval, Foundations of photonic crystal fibres, 2nd ed (Imperial College Press, 2012).

[14] P. St. J. Russell, "Photonic crystal fibers," Science **299**, 358–362 (2003).

[15] P. St. J. Russell, "Photonic-crystal fibers," J. Lightwave Technol. **24**, 4729–4749 (2006).

[16] T. A. Birks, D. Mogilevtsev, J. C. Knight, and P. St. J. Russell, "Dispersion compensation using single-material fibers," IEEE Photon. Technol. Lett. **11**, 674–676 (1999).

[17] P. Yeh and A. Yariv, "Bragg reflection waveguides," Opt. Commun. **19**, 427–430 (1976).

[18] P. Yeh, A. Yariv, and E. Marom, "Theory of Bragg fiber," J. Opt. Soc. Am. **68**, 1196–1201 (1978).

[19] F. Poletti, M. N. Petrovich, and D. J. Richardson, "Hollow-core photonic bandgap fibers: technology and applications," Nanophotonics **2**, 315–340 (2013).

[20] J. C. Knight, J. Broeng, T. A. Birks, and P. St. J. Russell, "Photonic band gap guidance in optical fibers," Science **282**, 1476–1478 (1998).

[21] R. F. Cregan, B. J. Mangan, J. C. Knight, T. A. Birks, P. St. J. Russell, P. J. Roberts, and D. C. Allan, "Single-mode photonic band gap guidance of light in air," Science **285**, 1537–1539 (1999).

[22] P. J. Roberts, F. Couny, H. Sabert, B. J. Mangan, D. P. Williams, L. Farr, M. W. Mason, A. Tomlinson, T. A. Birks, J. C. Knight, and P. St. J. Russell, "Ultimate low loss of hollow-core photonic crystal fibres," Opt. Express **13**, 236–244 (2005).

[23] C. M. Smith, N. Venkataraman, M. T. Gallagher, D. Mller, J. A. West, N. F. Borrelli, D. C. Allan, and K. W. Koch, "Low-loss hollow-core silica/air photonic bandgap fibre," Nature **424**, 657–659 (2003).

[24] J. D. Shephard, J. D. C. Jones, D. P. Hand, G. Bouwmans, J. C. Knight, P. St. J. Russell, and B. J. Mangan, "High energy nanosecond laser pulses delivered single-mode through hollow-core PBG fibers," Opt. Express **12**, 717–723 (2004).

[25] F. Benabid, J. C. Knight, G. Antonopoulos, and P. St. J. Russell, "Stimulated Raman scattering in hydrogen-filled hollow-core photonic crystal fiber," Science **298**, 399–402 (2002).

[26] P. St. J. Russell, P. Hölzer, W. Chang, A. Abdolvand, and J. C. Travers, "Hollow-core photonic crystal fibres for gas-based nonlinear optics," Nat. Photonics **8**, 278–286 (2014).

[27] F. Benabid, F. Couny, J. C. Knight, T. A. Birks, and P. St. J. Russell, "Compact, stable and efficient all-fibre gas cells using hollow-core photonic crystal fibres," Nature **434**, 488–491 (2005).

[28] F. Couny, F. Benabid, and P. S. Light, "Large-pitch kagome-structured hollow-core photonic crystal fiber," Opt. Lett. **31**, 3574–3576 (2006).

[29] G. J. Pearce, G. S. Wiederhecker, C. G. Poulton, S. Burger, and P. St. J. Russell, "Models for guidance in kagome-structured hollow-core photonic crystal fibres," Opt. Express **31**, 12680–12685 (2007).

[30] F. Couny, F. Benabid, P. J. Roberts, P. S. Light, and M. G. Raymer, "Generation and Photonic Guidance of Multi-Octave Optical-Frequency Combs," Science **318**, 1118–1121 (2007).

[31] A. Argyros and J. Pla, "Hollow-core polymer fibres with a kagome lattice: potential for transmission in the infrared," Opt. Express **15**, 7713–7719 (2007).

[32] M. A. Duguay, Y. Kokubun, T. L. Koch, and L. Pfeiffer, "Antiresonant reflecting optical waveguides in SiO_2-Si multiplayer structures," Appl. Phys. Lett. **49**, 13–15 (1986).

[33] Y. Kokubun, T. Baba, T. Sakaki, and K. Iga, "Low-loss antiresonant reflecting optical waveguide on Si substrate in visible-wavelength region," Electron. Lett. **22**, 892–893 (1986).

[34] N. M. Litchinitser, A. K. Abeeluck, C. Headley, and B. J. Eggleton, "Antiresonant reflecting photonic crystal optical waveguides," Opt. Lett. **27**, 1592–1594 (2002).

[35] N. M. Litchinitser, S. C. Dunn, B. Usner, B. J. Eggleton, T. P. White, R. C. McPhedran, and C. M. de Sterke, "Resonances in microstructured optical waveguides," Opt. Express **11**, 1243–1251 (2003).

[36] T. P. White, R. C. McPhedran, C. M. Sterke, N. M. Litchinitser, and B. J. Eggleton, "Resonance and scattering in microstructured optical fibers," Opt. Lett. **27**, 1977–1979 (2002).

[37] B. Debord, M. Alharbi, T. Bradley, C. Fourcade-Dutin, Y. Y. Wang, L. Vincetti, F. Gérôme, and F. Benabid, "Hypocycloid-shaped hollow-core photonic crystal fiber Part I: Arc curvature effect on confinement loss," Opt. Express **21**, 28597–28608 (2013).

[38] M. Alharbi, T. Bradley, B. Debord, C. Fourcade-Dutin, D. Ghosh, L. Vincetti, F. Gérôme, and F. Benabid, "Hypocycloid-shaped hollow-core photonic crystal fiber Part II: Cladding effect on confinement and bend loss," Opt. Express **21**, 28609–28616 (2013).

[39] A. Argyros, S. G. Leon-Saval, J. Pla, and A. Docherty, "Antiresonant reflection and inhibited coupling in hollow-core square lattice optical fibers," Opt. Express **16**, 5642–5648 (2008).

[40] F. Couny, P. J. Roberts, T. A. Birks, and F. Benabid, "Square-lattice large-pitch hollow-core photonic crystal fiber," Opt. Express **16**, 20626–20636 (2008).

[41] S. Février, B. Beaudou, and P. Viale, "Understanding origin of loss in large pitch hollow-core photonic crystal fibers and their design simplification," Opt. Express **18**, 5142–5150 (2010).

[42] F. Gérôme, R. Jamier, J.-L. Auguste, G. Humbert, and J.-M. Blondy, "Simplified hollow-core photonic crystal fiber," Opt. Lett. **35**, 1157–1159 (2010).

[43] F. Poletti, "Nested antiresonant nodeless hollow core fiber," Opt. Express **22**, 23807–23828 (2014).

[44] P. J. Roberts, D. P. Williams, B. J. Mangan, H. Sabert, F. Couny, W. J. Wadsworth, T. A. Birks, J. C. Knight, and P. St. J. Russell, "Realizing low loss air core photonic crystal fibers by exploiting an antiresonant core surround," Opt. Express **13**, 8277–8285 (2005).

[45] G. Pearce, J. Pottage, D. Bird, P. Roberts, J. Knight, and P. St. J. Russell, "Hollow-core PCF for guidance in the mid to far infra-red," Opt. Express **13**, 6937–6946 (2005).

[46] R. Amezcua-Correa, N. G. Broderick, M. N. Petrovich, F. Poletti, and D. J. Richardson, "Design of 7 and 19 cells core air-guiding photonic crystal fibers for low-loss, wide bandwidth and dispersion controlled operation," Opt. Express **15**, 17577–17586 (2007).

[47] Y. Wang, F. Couny, P. J. Roberts, and F. Benabid, "Low loss broadband transmission in optimized core-shaped Kagome hollow-core PCF," in *Conference on Lasers and Electro-Optics 2010*, OSA Technical Digest (CD) (Optical Society of America, 2010), paper CPDB4.

[48] Y. Y. Wang, N. V. Wheeler, F. Couny, P. J. Roberts, and F. Benabid, "Low loss broadband transmission in hypocycloid-core Kagome hollow-core photonic crystal fiber," Opt. Lett. **36**, 669–671 (2011).

[49] A. D. Pryamikov, A. S. Biriukov, A. F. Kosolapov, V. G. Plotnichenko, S. L. Semjonov, and E. M. Dianov, "Demonstration of a waveguide regime for a silica hollow-core microstructured optical fiber with a negative curvature of the core boundary in the spectral region > 3.5 μm," Opt. Express **19**, 1441–1448 (2011).

[50] F. Yu, W. J. Wadsworth, and J. C. Knight, "Low loss silica hollow core fibers for 3–4 μm spectral region," Opt. Express **20**, 11153–11158 (2012).

[51] A. N. Kolyadin, A. F. Kosolapov, A. D. Pryamikov, A. S. Biriukov, V. G. Plotnichenko, and E. M. Dianov, "Light transmission in negative curvature hollow core fiber in extremely high material loss region," Opt. Express **21**, 9514–9519 (2013).

[52] F. Yu and J. C. Knight, "Spectral attenuation limits of silica hollow core negative curvature fiber," Opt. Express **21**, 21466–21471 (2013).

[53] A. Urich, R. R. J. Maier, F. Yu, J. C. Knight, D. P. Hand, and J. D. Shephard, "Flexible delivery of Er:YAG radiation at 2.94 μm with negative curvature silica glass fibers: a new solution for minimally invasive surgical procedures," Biomed. Opt. Express **4**, 193–205 (2013).

[54] P. Jaworski, F. Yu, R. R. J. Maier, W. J. Wadsworth, J. C. Knight, J. D. Shephard, and D. P. Hand, "Picosecond and nanosecond pulse delivery through a hollow-core negative curvature fiber for micro-machining applications," Opt. Express **21**, 22742–22753 (2013).

[55] A. F. Kosolapov, A. D. Pryamikov, A. S. Biriukov, V. S. Shiryaev, M. S. Astapovich, G. E. Snopatin, V. G. Plotnichenko, M. F. Churbanov, and E. M. Dianov, "Demonstration of CO_2-laser power delivery through chalcogenide-glass fiber with negative-curvature hollow core," Opt. Express **19**, 25723–25728 (2011).

[56] B. Debord, A. Amsanpally, M. Chafer, A. Baz, L. Vincetti, J. Blondy, F. Gérôme, and F. Benabid, "7.7 dB/km losses in inhibited coupling hollow-core photonic crystal fibers," in *Conference on Lasers and Electro-Optics*, OSA Technical Digest (online) (Optical Society of America, 2016), paper JTh4C.8.

[57] B. Debord, A. Amsanpally, M. Chafer, A. Baz, M. Maurel, J. M. Blondy, E. Hugonnot, F. Scol, L. Vincetti, F. Gérôme, and F. Benabid, "Ultralow transmission loss in inhibited-coupling guiding hollow fibers," Optica **4**, 209–217 (2017).

[58] M. Michieletto, J. K. Lyngsø, C. Jakobsen, J. Lægsgaard, O. Bang, and T. T. Alkeskjold, "Hollow-core fibers for high power pulse delivery," Opt. Express **24**, 7103–7119 (2016).

[59] J. R. Hayes, S. R. Sandoghchi, T. D. Bradley, Z. Liu, R. Slavik, M. A. Gouveia, N. V. Wheeler, G. T. Jasion, Y. Chen, E. Numkam-Fokoua, M. N. Petrovich, D. J. Richardson, and F. Poletti, "Antiresonant hollow core fiber with octave spanning bandwidth for short haul data communications," in *Optical Fiber Communication Conference Postdeadline Papers*, OSA Technical Digest (online) (Optical Society of America, 2016), paper Th5A.3.

[60] J. R. Hayes, S. R. Sandoghchi, T. D. Bradley, Z. Liu, R. Slavik, M. A. Gouveia, N. V. Wheeler, G. Jasion, Y. Chen, E. N. Fokoua, M. N. Petrovich, D. J. Richardson, and F. Poletti, "Antiresonant hollow core fiber with an octave spanning bandwidth for short haul data communications," J. Lightwave Technol. **35**, 437–442 (2017).

[61] N. V. Wheeler, T. D. Bradley, J. R. Hayes, M. A. Gouveia, S. Liang, Y. Chen, S. R. Sandoghchi, S. M. Abokhamis Mousavi, F. Poletti, M. N. Petrovich, and D. J. Richardson, Low-loss Kagome hollow-core fibers operating from the near- to the mid-IR, Opt. Lett. **42**, 2571–2574 (2017).

[62] A. F. Kosolapov, G. K. Alagashev, A. N. Kolyadin, A. D. Pryamikov, A. S. Biryukov, I. A. Bufetov, and E. M. Dianov, "Hollow-core revolver fibre with a double-capillary reflective cladding," Quantum Electron. **46**, 267–270 (2016).

[63] C. Wei, R. Kuis, F. Chenard, and J. Hu, "Chalcogenide negative curvature hollow-core photonic crystal fibers with low loss and low power ratio in the glass," in *CLEO: 2014*, OSA Technical Digest (online) (Optical Society of America, 2014), paper SM1N.5.

[64] W. Belardi and J. C. Knight, "Effect of core boundary curvature on the confinement losses of hollow antiresonant fibers," Opt. Express **21**, 21912–21917 (2013).

[65] W. Belardi and J. C. Knight, "Hollow antiresonant fibers with reduced attenuation," Opt. Lett. **39**, 1853–1856 (2014).

[66] M. S. Habib, O. Bang, and M. Bache, "Low-loss hollow-core silica fibers with adjacent nested anti-resonant tubes," Opt. Express **23**, 17394–17406 (2015).

[67] A. F. Kosolapov, A. Pryamikov, G. Alagashev, A. Kolyadin, A. Biriukov, and E. Dianov, "Negative curvature hollow-core fibers (NCHCFs) for mid-IR Applications," in *Advanced Photonics*, OSA Technical Digest (online) (Optical Society of America, 2014), paper SoTu2B.3.

[68] G. K. Alagashev, A. D. Pryamikov, A. F. Kosolapov, A. N. Kolyadin, A. Y. Lukovkin, and A. S. Biriukov, "Impact of geometrical parameters on the optical properties of negative curvature hollow core fibers," Laser Phys. **25**, 055101 (2015).

[69] W. Belardi and J. C. Knight, "Hollow antiresonant fibers with low bending loss," Opt. Express **22**, 10091–10096 (2014).

[70] C. Wei, R. A. Kuis, F. Chenard, C. R. Menyuk, and J. Hu, "Higher-order mode suppression in chalcogenide negative curvature fibers," Opt. Express **23**, 15824–15832 (2015).

[71] C. Wei, O. Alvarez, F. Chenard, J. Hu, "Empirical glass thickness for chalcogenide negative curvature fibers," in *Summer Topicals Meeting Series 2015* (IEEE Photonics Society, 2015), paper TuE3.3.

[72] A. D. Pryamikov, G. K. Alagashev, and A. S. Biriukov, "Impact of core cladding boundary shape on the waveguide properties of hollow core microstructured fibers," Laser Phys. **26**, 125104 (2016).

[73] J. H. V. Price, T. M. Monro, H. Ebendorff-Heidepriem, F. Poletti, P. Horak, V. Finazzi, J. Y. Y. Leong, P. Petropoulos, J. C. Flanagan, G. Brambilla, X. Feng, and D. J. Richardson, "Mid-IR supercontinuum generation from non-silica microstructured optical fibers," IEEE J. Sel. Topics Quantum Electron. **13**, 738 (2007).

[74] X. Jiang, N. Y. Joly, M. A. Finger, F. Babic, G. K. L. Wong, J. C. Travers, and P. St. J. Russell, "Deep-ultraviolet to mid-infrared supercontinuum generated in solid-core zblan photonic crystal fibre," Nat. Photonics **9**, 133–139 (2015).

[75] G. Tao, H. Ebendorff-Heidepriem, A. M. Stolyarov, S. Danto, J. V. Badding, Y. Fink, J. Ballato, and A. F. Abouraddy, "Infrared fibers," Adv. Opt. Photon. **7**, 379–458 (2015).

[76] W. Belardi, N. White, J. Lousteau, X. Feng, and F. Poletti, "Hollow core antiresonant fibers in borosilicate glass," in *Workshop on Specialty Optical Fibers and Their Applications*, OSA Technical Digest (online) (Optical Society of America, 2015), paper WW4A.4.

[77] R. R. Gattass, D. Rhonehouse, D. Gibson, C. C. McClain, R. Thapa, V. Q. Nguyen, S. S. Bayya, R. J. Weiblen, C. R. Menyuk, L. B. Shaw, and J. S. Sanghera, "Infrared glass-based negative-curvature anti-resonant fibers fabricated through extrusion," Opt. Express **24**, 25697–25703 (2016).

[78] V. S. Shiryaev, "Chalcogenide glass hollow-core microstructured optical fibers," Front. Mater. **2**, 24 (2015).

[79] V. S. Shiryaev, A. F. Kosolapov, A. D. Pryamikov, G. E. Snopatin, M. F. Churbanov, A. S. Biriukov, T. V.Kotereva, S. V. Mishinov, G. K. Alagashev, and A. N. Kolyadin, "Development of technique for preparation of As_2S_3 glass preforms for hollow core microstructured optical fibers," J. Optoelectron. Adv. M. **16**, 1020–1025 (2014).

[80] P. Uebel, M. C. Günendi, M. H. Frosz, G. Ahmed, N. N. Edavalath, J.-M. Ménard, and P. St. J. Russell, "Broadband robustly single-mode hollow-core PCF by resonant filtering of higher-order modes," Opt. Lett. **41**, 1961–1964 (2016).

[81] X. Liu, W. Ding, Y. Y. Wang, S. Gao, L. Cao, X. Feng, and P. Wang, "Characterization of a liquid-filled nodeless anti-resonant fiber for biochemical sensing," Opt. Lett. **42**, 863–866 (2017).

[82] A. V. Newkirk, J. E. Antonio-Lopez, J. Anderson, R. Alvarez-Aguirre, Z. S. Eznaveh, G. Lopez-Galmiche, R. Amezcua-Correa, and A. Schülzgen, "Modal analysis of antiresonant hollow core fibers using S^2 imaging," Opt. Lett. **41**, 3277–3280 (2016).

[83] V. Setti, L. Vincetti, and A. Argyros, "Flexible tube lattice fibers for terahertz applications," Opt. Express **21**, 3388–3399 (2013).

[84] Z. Wang, W. Belardi, F. Yu, W. J. Wadsworth, and J. C. Knight, "Efficient diode-pumped mid-infrared emission from acetylene-filled hollow-core fiber," Opt. Express **22**, 21872–21878 (2014).

[85] W. Belardi, "Design and properties of hollow antiresonant fibers for the visible and near infrared spectral range," J. Lightwave Technol. **33**, 4497–4503 (2015).

[86] Y. Y. Wang, X. Peng, M. Alharbi, C. F. Dutin, T. D. Bradley, F. Gérôme, M. Mielke, T. Booth, and F. Benabid, "Design and fabrication of hollow-core photonic crystal fibers for high-power ultrashort pulse transportation and pulse compression," Opt. Lett. **37**, 3111–3113 (2012).

[87] X. Huang, W. Qi, D. Ho, K. T. Yong, F. Luan, and S. Yoo, "Hollow core anti-resonant fiber with split cladding," Opt. Express **24**, 7670–7678 (2016).

[88] Y. Chen, M. F. Saleh, N. Y. Joly, and F. Biancalana, "Guiding 2.94 μm using low-loss microstructured antiresonant triangular-core fibers," J. Appl. Phys. **119**, 143104 (2016).

[89] F. Yu, M. Xu, and J. C. Knight, "Experimental study of low-loss single-mode performance in anti-resonant hollow-core fibers," Opt. Express **24**, 12969–12975 (2016).

[90] W. Ding and Y. Wang, "Analytic model for light guidance in single wall hollow-core anti-resonant fibers," Opt. Express **22**, 27242–27256 (2014).

[91] X. Liu, Z. Fan, Z. Shi, Y. Ma, J. Yu, and J. Zhang, "Dual-core antiresonant hollow core fibers," Opt. Express **24**, 17453–17458 (2016).

[92] A. V. V. Nampoothiri, A. M. Jones, C. Fourcade-Dutin, C. Mao, N. Dadashzadeh, B. Baumgart, Y. Y. Wang, M. Alharbi, T. Bradley, N. Campbell, F. Benabid, B. R. Washburn, K. L. Corwin, and W. Rudolph, "Hollow-core optical fiber gas lasers (HOFGLAS): a review [Invited]," Opt. Mater. Express **2**, 948–961 (2012).

[93] F. Emaury, C. F. Dutin, C. J. Saraceno, M. Trant, O. H. Heckl, Y. Y. Wang, C. Schriber, F. Gerome, T. Südmeyer, F. Benabid, and U. Keller, "Beam delivery and pulse compression to sub-50 fs of a mode locked thin disk laser in a gas-filled Kagome-type HC-PCF fiber," Opt. Express **21**, 4986–4994 (2013).

[94] A. V. V. Nampoothiri, B. Debord, M. Alharbi, F. Gérôme, F. Benabid, and W. Rudolph, “CW hollow-core optically pumped I_2 fiber gas laser,” Opt. Lett. **40**, 605–608 (2015).

[95] J. Yang, B. Yang, Z. Wang, W. Liu, “Design of the low-loss wide bandwidth hollow-core terahertz inhibited coupling fibers,” Opt. Commun. **343**, 150–156 (2015).

[96] T. D. Bradley, Y. Wang, M. Alharbi, B. Debord, C. Fourcade-Dutin, B. Beaudou, F. Gerome, and F. Benabid, “Optical properties of low loss (70 dB/km) hypocycloid-core kagome hollow core photonic crystal fiber for Rb and Cs based optical applications,” J. Lightwave Technol. **31**, 2752–2755 (2013).

[97] T. D. Bradley, J. Jouin, J. J. McFerran, P. Thomas, F. Gerome, and F. Benabid, “Extended duration of rubidium vapor in aluminosilicate ceramic coated hypocycloidal core kagome HC-PCF,” J. Lightwave Technol. **32**, 2486–2491 (2014).

[98] L. Vincetti and V. Setti, “Extra loss due to Fano resonances in inhibited coupling fibers based on a lattice of tubes,” Opt. Express **20**, 14350–14361 (2012).

[99] A. Benoît, B. Beaudou, M. Alharbi, B. Debord,F. Gérôme, F. Salin, and F. Benabid, “Over-five octaves wide Raman combs in high-power picosecond-laser pumped H_2-filled inhibited coupling kagome fiber,” Opt. Express **23**, 14002–14009 (2015).

[100] B. Debord, A. Amsanpally, M. Alharbi, L. Vincetti, J. M. Blondy, F. Gérôme, and F. Benabid, “Ultra-large core size hypocycloid-shape inhibited coupling kagome fibers for high-energy laser beam handling,” J. Lightwave Technol. **33**, 3630–3634 (2015).

[101] X. Zheng, B. Debord, L. Vincetti, B. Beaudou, F. Gérôme, and F. Benabid, “Fusion splice between tapered inhibited coupling hypocycloid-core Kagome fiber and SMF,” Opt. Express **24**, 14642-14647 (2016).

[102] D. V. Bogdanovich, A. K. Srivastava, V. G. Chigrinov, A. S. Biriukov, and A. D. Pryamikov, “Hollow core negative curvature fibre with layers of photoaligned optically anisotropic material,” Laser Phys. Lett. **12**, 105101 (2015).

[103] A. V. Gladyshev, A. N. Kolyadin, A. F. Kosolapov, Y. P Yatsenko, A. D. Pryamikov, A. S. Biryukov, I. A. Bufetov, and E, M, Dianov, “Efficient 1.9-μm Raman generation in a hydrogen-filled hollow-core fibre,” Quantum Electron. **45**, 807–812 (2015).

[104] A. A. Krylov, A. K. Senatorov, A. D. Pryamikov, A. F. Kosolapov, A. N. Kolyadin, G. K. Alagashev, A. V. Gladyshev, and I. A. Bufetov, “1.56 μm sub-microjoule femtosecond pulse delivery through low-loss microstructured revolver hollow-core fiber,” Laser Phys. Lett. **14**, 035104 (2017).

[105] A. D. Pryamikov, A. F. Kosolapov, G. K. Alagashev, A. N. Kolyadin, V. V. Vel'miskin, A. S. Biriukov, and I. A. Bufetov, "Hollow-core microstructured 'revolver' fibre for the UV spectral range," Quantum Electron. **46**, 617–626 (2016).

[106] Y. P. Yatsenko, E. N. Pleteneva, A. G. Okhrimchuk, A. V. Gladyshev, A. F. Kosolapov, A. N. Kolyadin, and I. A. Bufetov, "Multiband supercontinuum generation in an air-core revolver fibre," Quantum Electron. **47**, 553–560 (2017).

[107] L. Vincetti and V. Setti, "Waveguiding mechanism in tube lattice fibers," Opt. Express **18**, 23133–23146 (2010).

[108] L. Vincetti and V. Setti, "Confinement loss in kagome and tube lattice fibers: comparison and analysis," J. Lightwave Technol. **30**, 1470–1474 (2012).

[109] L. Vincetti, "Single-mode propagation in triangular tube lattice hollow-core terahertz fibers," Opt. Commun. **283**, 979–984 (2010).

[110] W. Lu, S. Lou, and A. Argyros, "Investigation of flexible low-loss hollow-core fibres with tube-lattice cladding for Terahertz radiation," IEEE J. Sel. Topics Quantum Electron. **22**, 214–220 (2016).

[111] J. Lu, C. Yu, H. Chang, H. Chen, Y. Li, C. Pan, and C. Sun, "Terahertz air-core microstructure fiber," Appl. Phys. Lett. **92**, 064105 (2008).

[112] L. Vincetti, "Empirical formulas for calculating loss in hollow core tube lattice fibers," Opt. Express **24**, 10313–10325 (2016).

[113] X. Huang, S. Yoo, and K. Yong, "Function of second cladding layer in hollow core tube lattice fibers," Sci. Rep. **7**, 1618 (2017).

[114] A. Hartung, J. Kobelke, A. Schwuchow, K. Wondraczek, J. Bierlich, J. Popp, T. Frosch, and M. A. Schmidt, "Double antiresonant hollow core fiber-guidance in the deep ultraviolet by modified tunneling leaky modes," Opt. Express **22**, 19131–19140 (2014).

[115] A. Hartung, J. Kobelke, A. Schwuchow, K. Wondraczek, J. Bierlich, J. Popp, T. Frosch, and M. A. Schmidt, "Origins of modal loss of antiresonant hollow-core optical fibers in the ultraviolet," Opt. Express **23**, 2557–2265 (2015).

[116] J. R. Hayes, F. Poletti, M. S. Abokhamis, N. V. Wheeler, N. K. Baddela, and D. J. Richardson, "Anti-resonant hexagram hollow core fibers," Opt. Express **23**, 1289–1299 (2015).

[117] A. Hartung, J. Kobelke, A. Schwuchow, J. Bierlich, J. Popp, M. A. Schmidt, and T. Frosch, "Low-loss single-mode guidance in large-core antiresonant hollow-core fibers," Opt. Lett. **40**, 3432–3435 (2015).

[118] A. Urich, R. R. J. Maier, F. Yu, J. C. Knight, D. P. Hand, and J. D. Shephard, "Silica hollow core microstructured fibres for mid-infrared surgical applications," J. Non-Cryst. Solids **377**, 236–239 (2013).

[119] M. R. A. Hassan, F. Yu, W. J. Wadsworth, and J. C. Knight , "Cavity-based mid-IR fiber gas laser pumped by a diode laser," Optica **3**, 218–221 (2016).

[120] S. Wu, C. Wang, C. Fourcade-Dutin, B. R. Washburn, F. Benabid, and K. L. Corwin, "Direct fiber comb stabilization to a gas-filled hollow-core photonic crystal fiber," Opt. Express **22**, 23704–23715 (2014).

[121] B. Debord, M. Alharbi, L. Vincetti, A. Husakou, C. Fourcade-Dutin, C. Hoenninger, E. Mottay, F. Gérôme, and F. Benabid, "Multi-meter fiber-delivery and pulse self-compression of milli-Joule femtosecond laser and fiber-aided laser-micromachining," Opt. Express **22**, 10735–10746 (2014).

[122] P. Jaworski, F. Yu, R. M. Carter, J. C. Knight, J. D. Shephard, and D. P. Hand, "High energy green nanosecond and picosecond pulse delivery through a negative curvature fiber for precision micro-machining," Opt. Express **23**, 8498–8506 (2015).

[123] B. Beaudou, F. Gerôme, Y. Y. Wang, M. Alharbi, T. D. Bradley, G. Humbert, J.-L. Auguste, J.-M. Blondy, and F. Benabid, "Millijoule laser pulse delivery for spark ignition through kagome hollow-core fiber," Opt. Lett. **37**, 1430–1432 (2012).

[124] Y. Wang, M. Alharbi, T. D. Bradley, C. Fourcade-Dutina, B. Deborda, B. Beaudoua, F. Gérôme, and F. Benabid, "Hollow-core photonic crystal fibre for high power laser beam delivery," High Power Laser Sci. Eng. **1**, 17–28 (2013).

[125] T. G. Polanyi, H. C. Bredemeier, and T. W. D. Jr, "A CO_2 laser for surgical research," Med. Biol. Eng. **8**, 541–548 (1970).

[126] K. M. Sasaki, A. Aoki, S. Ichinose, T. Yoshino, S. Yamada, and I. Ishikawa, "Scanning electron microscopy and fourier transformed infrared spectroscopy analysis of bone removal using Er:YAG and CO_2 lasers," J. Periodontol. **73**, 643–652 (2002).

[127] S. Amini-Nik, D. Kraemer, M. L. Cowan, K. Gunaratne, P. Nadesan, B. A. Alman, and R. J. D. Miller, "Ultrafast mid-IR laser scalpel: protein signals of the fundamental limits to minimally invasive surgery," PLoS One **5**, e13053 (2010).

[128] S. Stübinger, B. von Rechenberg, H. F. Zeilhofer, R. Sader, and C. Landes, "Er:YAG laser osteotomy for removal of impacted teeth: clinical comparison of two techniques," Lasers Surg. Med. **39**, 583–588 (2007).

[129] H. Garvie-Cook, "Background," in *Novel (Trans) dermal drug delivery strategies: Micro-and Nano-scale assessments.* (Springer, 2016), pp. 5–28.

[130] H. Garvie-Cook, J. M. Stone, F. Yu, R. H. Guy, and S. N. Gordeev, "Femtosecond pulsed laser ablation to enhance drug delivery across the skin," J. Biophoton. **9**, 144–154 (2016).

[131] Y. P. Yatsenko, A. A. Krylov, A. D. Pryamikov, A. F. Kosolapov, A. N. Kolyadin, A. V. Gladyshev, and I. A. Bufetov, "Propagation of femtosecond pulses in a hollow-core revolver fibre," Quantum Electron. **46**, 617–626 (2016).

[132] C. Lai, B. You, J. Lu, T. Lu, J. Peng, C. Sun, and H. Chang, "Modal characteristics of antiresonant reflecting pipe waveguides for terahertz waveguiding," Opt. Express **18**, 309–322 (2010).

[133] E. Nguema, D. Férachou, G. Humbert, J.-L. Auguste, and J.-M. Blondy, "Broadband terahertz transmission within the air channel of thin-wall pipe," Opt. Lett. **36**, 1782–1784 (2011).

[134] W. Ding and Y. Wang, "Semi-analytical model for hollow-core anti-resonant fibers," Front. Phys. **3**, 16 (2015).

[135] J. Hu and C. R. Menyuk, "Understanding leaky modes: Slab waveguide revisited," Adv. Opt. Photon. **1**, 58–106 (2009).

[136] D. Marcuse, Theory of Dielectric Optical Waveguides, 2nd ed. (Academic, New York, 1991).

[137] M. N. O. Sadiku, Numerical Techniques in Electromagnetics, 2nd ed. (CRC Press, 2001).

[138] J. Jin, The Finite Element Method in Electromagnetics, 2nd ed. (Wiley, 2002).

[139] T. P. White, B. T. Kuhlmey, R. C. McPhedran, D. Maystre, G. Renversez, C. M. de Sterke, and L. C. Botten, "Multipole method for microstructured optical fibers. I. Formulation," J. Opt. Soc. Am. B **19**, 2322–2330 (2002).

[140] J. Hu and C. R. Menyuk, "Leakage loss and bandgap analysis in air-core photonic bandgap fiber for nonsilica glasses," Opt. Express **15**, 339–349 (2007).

[141] C. Wei, C. R. Menyuk, and J. Hu, "Impact of cladding tubes in chalcogenide negative curvature fibers," IEEE Photon. J. **8**, 2200509 (2016).

[142] C. Wei, J. Hu, and C. R. Menyuk, "Comparison of loss in silica and chalcogenide negative curvature fibers as the wavelength varies," Front. Phys. **4**, 30 (2016).

[143] F. Poletti, J. R. Hayes, and D. Richardson, "Optimising the performances of hollow antiresonant fibres," in *37th European Conference and Exposition on Optical Communications*, OSA Technical Digest (CD) (Optical Society of America, 2011), paper Mo.2.LeCervin.2.

[144] M. Born and E. Wolf, "Elements of the theory of interference and interferometers," in *Principles of Optics*, (Cambridge University, 1999, 7th ed.), pp. 359–366.

[145] P. K. Choudhury and T. Yoshino, "A rigorous analysis of the power distribution in plastic clad annular core optical fibers," Optik **113**, 481–488 (2002).

[146] M. Hautakorpi and M. Kaivola, "Modal analysis of M-type-dielectric-profile optical fibers in the weakly guiding approximation," J. Opt. Soc. Am. A **22**, 1163–1169 (2005).

[147] B. C. Sarkar, P. K. Choudhury, and T. Yoshino, "On the analysis of a weakly guiding doubly clad dieletric optical fiber with annular core," Microw. Opt. Technol. Lett. **31**, 435–439 (2001).

[148] Y. Koyamada, "Analysis of core-mode to radiation-mode coupling in fiber Bragg gratings with finite cladding radius," J. Lightwave Technol. **18**, 1220–1225, (2000).

[149] K. Saitoh and M. Koshiba, "Leakage loss and group velocity dispersion in air-core photonic bandgap fibers," Opt. Express **11**, 3100–3109 (2003).

[150] C. Wei, C. Menyuk, and J. Hu, "Bending-induced mode non-degeneracy and coupling in chalcogenide negative curvature fibers," Opt. Express **24**, 12228–12239 (2016).

[151] G. Ren, Z. Wang, S. Lou, and S. Jian, "Mode classification and degeneracy in photonic crystal fibers," Opt. Express **11**, 1310–1321(2003).

[152] M. A. Khashan and A. Y. Nassif, "Dispersion of the optical constants of quartz and polymethyl methacrylate glasses in a wide spectral range: 0.2–3 μm," Opt. Commun. **188**, 129–139 (2001).

[153] A. Yariv, "Guided wave optics—propagation in optical fibers," in *Quantum Electronics*, 3rd ed. (Wiley, 1989), pp. 600–650.

[154] B. E. A. Saleh and M. C. Teich, "Guided-Wave Optics," in *Fundamentals of Photonics*, 2nd ed. (Wiley, 2007), pp. 289–299.

[155] K. Saitoh, N. A. Mortensen, and M. Koshiba, "Air-core photonic band-gap fibers: the impact of surface modes," Opt. Express **12**, 394–400 (2004).

[156] Z. Zhang, Y. Shi, B. Bian, and J. Lu, "Dependence of leaky mode coupling on loss in photonic crystal fiber with hybrid cladding," Opt. Express **16**, 1915–1922 (2008).

[157] J. Hu and C. R. Menyuk, "Optimization of the operational bandwidth in air-core photonic bandgap filbers for IR transmission," Opt. Commun. **282**, 18–21 (2009).

[158] K. Saitoh and M. Koshiba, "Confinement losses in air-guiding photonic bandgap fibers," IEEE Photon. Technol. Lett. **15**, 236–238 (2003).

[159] B. J. Mangan, L. Farr, A. Langford, P. J. Roberts, D. P. Williams, F. Couny, M. Lawman, M. Mason, S. Coupland, R. Flea, H. Sabert, T. A. Birks, J. C. Knight, and P. St. J. Russell, "Low loss (1.7 dB/km) hollow core photonic bandgap fiber," in *Optical Fiber Communication Conference*, Technical Digest (CD) (Optical Society of America, 2004), paper PD24.

[160] M. H. Frosz, J. Nold, T. Weiss, A. Stefani, F. Babic, S. Rammler, P. St. J. Russell, "Five-ring hollow-core photonic crystal fiber with 1.8 dB/km loss," Opt. Lett. **38**, 2215–2217 (2013).

[161] W. Ding and Y. Y. Wang, "Hybrid transmission bands and large birefringence in hollow-core anti-resonant fibers," Opt. Express **23**, 21165–21174 (2015).

[162] P. Yeh, A. Yariv, and C. Hong, "Electromagnetic propagation in periodic stratified media. I. General theory," J. Opt. Soc. Am. **67**, 423–438 (1977).

[163] E. N. Fokoua, F. Poletti, and D. J. Richardson, "Analysis of light scattering from surface roughness in hollow-core photonic bandgap fibers," Opt. Express **20**, 20980–20991 (2012).

[164] W. Belardi and J. C. Knight, "Negative curvature fibers with reduced leakage loss," in *Optical Fiber Communication Conference*, OSA Technical Digest (online) (Optical Society of America, 2014), paper Th2A.45.

[165] J. D. Shephard, A. Urich, R. M. Carter, P. Jaworski, R. R. J. Maier, W. Belardi, F. Yu, W. J. Wadsworth, J. C. Knight, and D. P. Hand, "Silica hollow core microstructured fibers for beam delivery in industrial and medical applications," Front. Phys. **3**, 24 (2015).

[166] J. Broeng, S. E. Barkou, T. Søndergaard, and A. Bjarklev, "Analysis of air-guiding photonic bandgap fibers," Opt. Lett. **25**, 96–98 (2000).

[167] M. N. Petrovich, R. Amezcua-Correa, N. G. Broderick, D. J. Richardson, T. Delmonte, M. A.Watson, and E.J. O'Driscoll, "Photonic bandgap fibres for broadband transmission of SWIR wavelengths," in *Electro Magnetic Remote Sensing (EMRS) Defense Technology Centre (DTC) conference 2006*, paper B19.

[168] E. B. Kryukova, V. G. Plotnichenko, and E. M. Dianov, "IR absorption spectra in high-purity silica glasses fabricated by different technologies," in *Proc. SPIE* 4083, 7180 (2000).

[169] M. Bass, J. M. Enoch, E. W. Van Stryland, and W. L. Wolfe, "Infrared Fibers," in *Handbook of Optics: Fiber and Integrated Optics*, (New York, McGraw-Hill, 2000).

[170] C. Xia, M. Kumar, O. P. Kulkarni, M. N. Islam, F. L. Terry, M. J. Freeman, M. Poulain, and G. Maze, "Mid-infrared supercontinuum generation to 4.5 μm in ZBLAN fluoride fibers by nanosecond diode pumping," Opt. Lett. **31**, 2553–2555 (2006).

[171] H. Ebendorff-Heidepriem, K. Kuan, M. R. Oermann, K. Knight, and T. M. Monro, "Extruded tellurite glass and fibers with low OH content for mid-infrared applications," Opt. Mater. Express **2**, 432–442 (2012)

[172] G. B. Thomas and R. L. Finney, Calculus and Analytic Geometry, 9th ed. (Addison-Wesley, Boston, 1995).

[173] V. Q. Nguyen, J. S. Sanghera, P. C. Pureza, F. H. Kung, and I. D. Aggarwal, "Fabrication of arsenic selenide optical fiber with low hydrogen impurities," J. Am. Ceram. Soc. **85**, 2849–2851 (2002).

[174] J. S. Sanghera, I. D. Aggarwal, L. B. Shaw, C. M. Florea, P. Pureza, V. Q. Nguyen, F. Kung, and I. D. Aggarwal, "Nonlinear properties of chalcogenide glass fibers," J. Optoelectron. Adv. Mater. **8**, 21482155 (2006).

[175] M. F. Churbanov, "Recent advances in preparation of high-purity chalcogenide glasses in the USSR," Journal of non-crystalline solids **140**, 324–330 (1992).

[176] C. T. Moynihan, P. B. Macedo, M. S. Maklad, R. K. Mohr, and Howard, R. E., "Intrinsic and impurity infrared absorption in As_2Se_3 glass," Journal of Non-Crystalline Solids **17**, 369–385 (2002).

[177] W. Ding and Y. Wang, "Analytic model for light guidance in single-wall hollow-core anti-resonant fibers," Opt. Express **22**, 27242–27256 (2014).

[178] N. Edavalath, M. H. Frosz, J. Ménard, and P. S. Russell, "Fabrication and side-coupling characterization of hexagonal lattice single-ring hollow-core PCFs," in *Frontiers in Optics 2015*, Optical Society of America, San Jose, USA, 2015, paper: FM3G.3.

[179] A. D. Pryamikov, A. F. Kosolapov, V. G. Plotnichenko, and E. M. Dianov, "Transmission of CO_2 laser radiation through glass hollow core microstructured fibers," in *CO_2 Laser - Optimisation and Application*, D. C. Dumitras, ed. (InTech, 2012).

[180] A. Schliesser, N. Picqué, and T. W. Hänsch, "Mid-infrared frequency combs," Nat. Photonics **6**, 440–449 (2012).

[181] Y. Yao, J. A. Hoffman, and C. F. Gmachl, "Mid-infrared quantum cascade lasers," Nat. Photonics **6**, 432–439 (2012).

[182] W. Xing, J. Bai, and Y. Li, “Mode classification and calculation in all-solid photonic bandgap fibers,” J. Lightw. Technol. **30**, 821–828 (2012).

[183] J. Hu, C. R. Menyuk, L. B. Shaw, J. S. Sanghera, and I. D. Aggarwal, “Computational study of a 3–5 μm source that is created by using supercontinuum generation in As_2S_3 chalcogenide fibers with a pump at 2 μm,” Opt. Lett. **35**, 2907–2909 (2010).

[184] V. G. Ta’eed, N. J. Baker, L. B. Fu, K. Finsterbusch, M. R. E. Lamont, D. J. Moss, H. C. Nguyen, B. J. Eggleton, D. Y. Choi, S. Madden, and B. Luther-Davies, “Ultrafast all-optical chalcogenide glass photonic circuits,” Opt. Exp. **15**, 9205–9221 (2007).

[185] P. Klocek, Handbook of infrared optical materials. New York, NY, USA: CRC, 1991.

[186] J. M. Fini, “Aircore microstructure fibers with suppressed higher-order modes,” Opt. Express **14**, 11354–11361 (2006).

[187] K. Saitoh, N. J. Florous, T. Murao, and M. Koshiba, “Design of photonic band gap fibers with suppressed higher-order modes: Towards the development of effectively single mode large hollow-core fiber platforms,” Opt. Express **14**, 7342–7352 (2006).

[188] J. M. Fini, J. W. Nicholson, R. S. Windeler, E. M. Monberg, L. Meng, B. Mangan, A. Desantolo, and F. V. DiMarcello, “Low-loss hollow-core fibers with improved single-modedness,” Opt. Express **21**, 6233–6242 (2013).

[189] T. Murao, K. Saitoh and M. Koshiba, “Multiple resonant coupling mechanism for suppression of higher-order modes in all-solid photonic bandgap fibers with heterostructured cladding,” Opt. Express **19**, 1713–1727 (2011).

[190] F. Jansen, F. Stutzki, C. Jauregui, J. Limpert, and A. Tünnermann, “Avoided crossings in photonic crystal fibers,” Opt. Express **19**, 13578–13589 (2011).

[191] J. A. West, C. M. Smith, N. F. Borrelli, D. C. Allan, and K. W. Koch, “Surface modes in air-core photonic band-gap fibers,” Opt. Express **12**, 1485–1496 (2004).

[192] G. Renversez, P. Boyer, and A. Sagrini, “Antiresonant reflecting optical waveguide microstructured fibers revisited: a new analysis based on leaky mode coupling,” Opt. Express **14**, 5682–5687 (2006).

[193] F. K. Tittel, D. Richter, and A. Fried, “Mid-infrared laser applications in spectroscopy,” in *Solid-State Mid-Infrared Laser Sources*, I.T. Sorokina and K.L. Vodopyanov, ed. (Springer, 2003).

[194] Y. Bai, S. Slivken, S. Kuboya, S. R. Darvish, and M. Razeghi, “Quantum cascade lasers that emit more light than heat,” Nat. Photonics **4**, 99–102 (2010).

[195] P. Q. Liu, A. J. Hoffman, M. D. Escarra, K. J. Franz, J. B. Khurgin, Y. Dikmelik, X. Wang, J.-Y. Fan, and C. F. Gmachl, "Highly power-efficient quantum cascade lasers," Nat. Photonics **4**, 95–98 (2010).

[196] Y. Bai, N. Bandyopadhyay, S. Tsao, S. Slivken and M. Razeghi, "Room temperature quantum cascade lasers with 27% wall plug efficiency," Appl. Phys. Lett. **98**, 181102 (2011).

[197] M. S. Habib, O. Bang, and M. Bache, "Low-loss single-mode hollow-core fiber with anisotropic anti-resonant elements," Opt. Express **24**, 8429–8436 (2016).

[198] P. Uebel, M. Günendi, M. H. Frosz, G. Ahmed, N. Edavalath, J. Ménard, and P. S. Russell, "A broad-band robustly single-mode hollow-core PCF by resonant filtering of higher order modes," in *Frontiers in Optics 2015*, OSA Technical Digest (online) (Optical Society of America, 2015), paper FW6C.2.

[199] C. Wei, J. Hu, and C. Menyuk, "Bending-induced mode coupling in chalcogenide negative curvature fibers," in *Advanced Photonics 2015*, OSA Technical Digest (online) (Optical Society of America, 2015), paper NT2C.5.

[200] M. Heiblum and J. H. Harris, "Analysis of curved optical waveguides by conformal transformation," IEEE J. Quantum Electron. **11**, 75–83 (1975).

[201] W. Liu, T. Guo, A. C. Wong, H. Y. Tam, and S. He, "Highly sensitive bending sensor based on Er^{3+}-doped DBR fiber laser," Opt. Express **18**, 17834–17840 (2010).

[202] M. Deng, C. P. Tang, T. Zhu, and Y. J. Rao, "Highly sensitive bend sensor based on Mach-Zehnder interferometer using photonic crystal fiber," Opt. Commun. **284**, 2849–2853 (2011).

[203] C. Wei, C. R. Menyuk, and J. Hu, "Polarization-filtering and polarization-maintaining low-loss negative curvature fibers," Opt. Express **26**, 9528–9540 (2018).

[204] F. Poletti, N. V. Wheeler, M. N. Petrovich, N. K. Baddela, E. Numkam Fokoua, J. R. Hayes, D. R. Gray, Z. Li, R. Slavik, and D. J. Richardson, "Towards high-capacity fibre-optic communications at the speed of light in vacuum," Nat. Photonics **7**, 279–284 (2013).

[205] P. K. A. Wai and C. R. Menyuk, "Polarization mode dispersion, decorrelation and diffusion in optical fibers with randomly varying birefringence," J. Lightwave Technol. **14**, 148–157 (1996).

[206] Y. Takushima, S. Yamashita, K. Kikuchi, and K. Hotate, "Polarization-stable and single-frequency fiber lasers," J. Lightwave Technol. **16**, 661–669 (1998).

[207] W. Burns, C. Lin, and R. Moeller, "Fiber-optic gyroscopes with broad-band sources," J. Lightwave Technol. **1**, 98–105 (1983).

[208] J. Noda, K. Okamoto, and Y. Sasaki, "Polarization-maintaining fibers and their applications," J. Lightwave Technol. **4**, 1071–1089 (1986).

[209] C. R. Menyuk, "Nonlinear pulse propagation in birefringent optical fibers," IEEE J. Quantum Electron. **23**, 174–176 (1987).

[210] K. Suzuki, H. Kubota, S. Kawanishi, M. Tanaka, and M. Fujita, "Optical properties of a low-loss polarization-maintaining photonic crystal fiber," Opt. Express **9**, 676–680 (2001).

[211] M. E. Fermann, M. J. Andrejco, Y. Silberberg, and M. L. Stock, "Passive mode locking by using nonlinear polarization evolution in a polarization-maintaining erbium-doped fiber," Opt. Lett. **18**, 894–896 (1993).

[212] A. D. Kim, J. N. Kutz, and D. J. Muraki, "Pulse-train uniformity in optical fiber lasers passively mode-locked by nonlinear polarization rotation," IEEE J. Ouantum Electron. **36**, 465–471 (2000).

[213] M. Salhi, H. Leblond, and F. Sanchez, "Theoretical study of the erbium-doped fiber laser passively mode-locked by nonlinear polarization rotation," Phys. Rev. A **67**, 013802 (2003).

[214] L. Vincetti and V. Setti, "Elliptical hollow core tube lattice fibers for terahertz applications," Opt. Fiber Technol. **19**(1), 31–34 (2013).

[215] S. A. Mousavi, S. R. Sandoghchi, D. J. Richardson, and F. Poletti, "Broadband high birefringence and polarizing hollow core antiresonant fibers," Opt. Express **24**, 22943–22958 (2016).

[216] J. E. Antonio-Lopez, S. Habib, A. V. Newkirk, G. Lopez-Galmiche, Z. S. Eznaveh, J. C. Alvarado-Zacarias, O. Bang, M. Bache, A. Schülzgen, and R. A. Correa, "Antiresonant hollow core fiber with seven nested capillaries," in *2016 IEEE Photonics Conference (IPC)*, Waikoloa, HI, 2016, pp. 402–403.

[217] J. M. Fini, J. W. Nicholson, B. Mangan, L. Meng, R. S. Windeler, E. M. Monberg, A. DeSantolo, F. V. DiMarcello, and K. Mukasa, "Polarization maintaining single-mode low-loss hollow-core fibres," Nat. Commun. **5**, 5085 (2014).

[218] D. J. Richardson, J. Nilsson, and W. A. Clarkson, "High power fiber lasers: current status and future perspectives [Invited]," J. Opt. Soc. B **27**, B63–B92 (2010).

[219] C. Xu and F. W. Wise, "Recent advances in fibre lasers for nonlinear microscopy," Nat. Photonics **7**, 875–882 (2013).

[220] F. Yu and J. C. Knight, "Negative curvature hollow-core optical fiber," IEEE J. Sel. Topics Quantum Electron. **22**, 4400610 (2016).

[221] E. M. Dianov, S. L. Semjonov, and I. A. Bufetov, "New generation of optical fibres," Quantum Electron. **46**, 1–10 (2016).

[222] T. Morioka, Y. Awaji, R. Ryf, P. Winzer, D. Richardson, and F. Poletti, "Enhancing optical communications with brand new fibers," IEEE Commun. Mag. **50**, S31–S42 (2012).

[223] V. A. Sleiffer, Y. Jung, P. Leoni, M. Kuschnerov, N. V. Wheeler, N. K. Baddela, R. G. H. van Uden, C. M. Okonkwo, J. R. Hayes, J. Wooler, E. Numkam, R. Slavik, F. Poletti, M. N. Petrovich, V. Veljanovski, S. U. Alam, D. J. Richardson, and H. de Waardt, "30.7 Tb/s (96×320 Gb/s) DP-32QAM transmission over 19-cell photonic band gap fiber," in *Optical Fiber Communication Conference/National Fiber Optic Engineers Conference 2013*, OSA Technical Digest (online) (Optical Society of America, 2013), paper OW1I.5.

[224] C. Dumitrache, J. Rath, and A. P. Yalin, "High power spark delivery system using hollow core kagome lattice fibers," Materials **7**, 5700–5710 (2014).

[225] M. R. B. Andreeta, L. S. Cunha, L. F. Vales, L. C. Caraschi, and R. G. Jasinevicius, "Bidimensional codes recorded on an oxide glass surface using a continuous wave CO_2 laser," J. Micromech. Microeng. **21**, 025004 (2011).

[226] A. N. Kolyadin, G. K. Alagasheva, A. D. Pryamikova, L. Mouradianb, A. Zeytunyanb, H. Toneyanb, A. F. Kosolapova, and I. A. Bufetov, "Negative curvature hollow-core fibers: dispersion properties and femtosecond pulse delivery," Phys. Procedia **73**, 59–66 (2015).

[227] R. M. Carter, W. N. MacPherson, P. Jaworski, F. Yu, R. Beck, J. D. Shephard, and D. P. Hand, "Dispersion measurement of microstructured negative curvature hollow core fiber," Opt. Eng. **55**, 116106 (2016).

[228] B. Sherlock, F. Yu, J. Stone, S. Warren, C. Paterson, M. A. A. Neil, P. M. W. French, J. Knight, and C. Dunsby, "Tunable fibre-coupled multiphoton microscopy with a negative curvature fibre," J. Biophoton. **9**, 715–720 (2016).

[229] G. I. Stegeman and R. H. Stolen, "Waveguides and fibers for nonlinear optics," J. Opt. Soc. Am. B **6**, 652-662 (1989).

[230] J. C. Travers, W. Chang, J. Nold, N. Y. Joly, and P. St. J. Russell, "Ultrafast nonlinear optics in gas-filled hollow-core photonic crystal fibers," J. Opt. Soc. Am. B **28**, A11–A26 (2011).

[231] J. M. Dudley and J. R. Taylor, "Ten years of nonlinear optics in photonic crystal fibre," Nat. Photonics **3**, 85–90 (2009).

[232] A. R. Bhagwat and A. L. Gaeta, "Nonlinear optics in hollow-core photonic bandgap fibers," Opt. Express **16**, 5035–5047 (2008).

[233] P. Hölzer, W. Chang, J. C. Travers, A. Nazarkin, J. Nold, N. Y. Joly, M. Saleh, F. Biancalana, and P. St. J. Russell, "Femtosecond nonlinear fiber optics in the ionization regime," Phys. Rev. Lett. **107**, 203901 (2011).

[234] F. Tani, J. C. Travers, and P. St. J. Russell, "Multimode ultrafast nonlinear optics in optical waveguides: numerical modeling and experiments in kagome photonic-crystal fiber," J. Opt. Soc. Am. B **31**, 311–320 (2014).

[235] M. I. Hasan, N. Akhmediev, and W. Chang, "Mid-infrared supercontinuum generation in supercritical xenon-filled hollow-core negative curvature fibers," Opt. Lett. **41**, 5122–5125 (2016).

[236] M. Cassataro, D. Novoa, M. C. Günendi, N. N. Edavalath, M. H. Frosz, J. C. Travers, and P. St.J. Russell, "Generation of broadband mid-IR and UV light in gas-filled single-ring hollow-core PCF," Opt. Express **25**, 7637–7644 (2017).

[237] A. M. Jones, A. V. V. Nampoothiri, A. Ratanavis, T. Fiedler, N. V. Wheeler, F. Couny, R. Kadel, F. Benabid, B. R. Washburn, K. L. Corwin, and W. Rudolph, "Mid-infrared gas filled photonic crystal fiber laser based on population inversion," Opt. Express **19**, 2309–2316 (2011).

[238] N. Dadashzadeh, M. P. Thirugnanasambandam, H. W. K. Weerasinghe, B. Debord, M. Chafer, F. Gerome, F. Benabid, B. R. Washburn, and K. L. Corwin, "Near diffraction-limited performance of an OPA pumped acetylene-filled hollow-core fiber laser in the mid-IR," Opt. Express **25**, 13351–13358 (2017).

[239] Z. Wang, F. Yu, W. J. Wadsworth, and J. C. Knight, "Efficient 1.9 μm emission in H_2-filled hollow core fiber by pure stimulated vibrational Raman scattering," Laser Phys. Lett. **11**, 105807 (2014).

[240] A. N. Kolyadin, G. K. Alagashev, A. D. Pryamikov, A. V. Gladyshev, A. F. Kosolapov, A. S. Biriukov, and IA. Bufetov, "Negative curvature hollow core fibers for Raman lasing in the mid IR spectral range," J. Phys. Conf. Ser. **737**, 012009 (2016).

[241] Y. Chen, Z. Wang, B. Gu, F. Yu, and Q. Lu, "Achieving a 1.5 μm fiber gas Raman laser source with about 400 kW of peak power and a 6.3 GHz linewidth," Opt. Lett. **11**, 5118–5121 (2016).

[242] A. V. Gladyshev, A. N. Kolyadin, A. F. Kosolapov, Y. P. Yatsenko, A. D. Pryamikov, A. S. Biriukov, I. A. Bufetov, and E. M. Dianov, "Low-threshold 1.9 μm Raman generation in microstructured hydrogen-filled hollow-core revolver fibre with nested capillaries," Laser Phys. **27**, 025101 (2016).

[243] B. Gu, Y. Chen, and Z. Wang, "Characteristics of 1.9-μm laser emission from hydrogen-filled hollow-core fiber by vibrational stimulated Raman scattering," Opt. Eng. **55**, 126114 (2016).

[244] A. V. Gladyshev, A. F. Kosolapov, M. M. Khudyakov, Y. P. Yatsenko, A. N. Kolyadin, A. A. Krylov, A. D. Pryamikov, A. S. Biriukov, M. E. Likhachev, I. A. Bufetov, and E. M. Dianov, "4.4 μm Raman laser based on hollow-core silica fibre," Quantum Electron. **47**, 491–494 (2017).

[245] B. Debord, M. Alharbi, A. Benoît, D. Ghosh, M. Dontabactouny, L. Vincetti, J.-M. Blondy, F. Gérôme, and F. Benabid, "Ultra low-loss hypocycloid-core Kagome hollow-core photonic crystal fiber for green spectral-range applications," Opt. Lett. **39**, 6245–6248 (2014).

[246] M. S. Habib, C. Markos, O. Bang, and M. Bache, "Soliton-plasma nonlinear dynamics in mid-IR gas-filled hollow-core fibers," Opt. Lett. **42**, 2232–2235 (2017).

[247] O. H. Heckl, C. J. Saraceno, C. R. E. Baer, T. Südmeyer, Y. Y. Wang, Y. Cheng, F. Benabid, and U. Keller, "Temporal pulse compression in a xenon-filled Kagome-type hollow-core photonic crystal fiber at high average power," Opt. Express **19**, 19142–19149 (2011).

[248] F. Emaury, C. J. Saraceno, B. Debord, D. Ghosh, A. Diebold, F. Gérôme, T. Südmeyer, F. Benabid, and U. Keller, "Efficient spectral broadening in the 100-W average power regime using gas-filled kagome HC-PCF and pulse compression," Opt. Lett. **39**, 6843–6846 (2014).

[249] T. Balciunas, C. Fourcade-Dutin, G. Fan, T. Witting, A. A. Voronin, A. M. Zheltikov, F. Gérôme, G. G. Paulus, A. Baltuska, and F. Benabid, "A strong-field driver in the single-cycle regime based on self-compression in a kagome fibre," Nat. Commun. **6**, 6117 (2015).

[250] F. Guichard, A. Giree, Y. Zaouter, M. Hanna, G. Machinet, B.Debord, F. Gérôme, P. Dupriez, F. Druon, C. Hönninger, E. Mottay, F. Benabid, and P. Georges, "Nonlinear compression of high energy fiber amplifier pulses in air-filled hypocycloid-core Kagome fiber," Opt. Express **23**, 7416–7423 (2015).

[251] A. M. Cubillas, X Jiang, T. G. Euser, N. Taccardi, B. J. M. Etzold, P. Wasserscheid, and P. St. J. Russell, "Photochemistry in a soft-glass single-ring hollow-core photonic crystal fiber," Analyst **142**, 925–929 (2017).

[252] A. M. Cubillas, S. Unterkofler, T. G. Euser, B. J. Etzold, A. C. Jones, P. J. Sadler, P. Wasserscheid, and P. St. J. Russell, "Photonic crystal fibres for chemical sensing and photochemistry," Chem. Soc. Rev. **42**, 8629–8648 (2013).

[253] T. Ritari, J. Tuominen, H. Ludvigsen, J. C. Petersen, H. Sorensen, T. P. Hansen, and H. R. Simonsen, "Gas sensing using air-guiding photonic crystal fibers," Opt. Express **12**, 4080–4087 (2004).

[254] S. Gao, Y. Y. Wang, X. Liu, C. Hong, S. Gu, and P. Wang, "Nodeless hollow-core fiber for the visible spectral range," Opt. Lett. **42**, 61–64 (2017).

[255] V. Sleiffer, Y. Jung, N. Baddela, J. Surof, M. Kuschnerov, V. Veljanovski, J. Hayes, N. Wheeler, E. Numkam Fokoua, J. Wooler, D. Gray, N. Wong, F. Parmigiani, S. Alam, M. Petrovich, F. Poletti, D. Richardson, and H. de Waardt, "High capacity mode-division multiplexed optical transmission in a novel 37-cell hollow-core photonic bandgap fiber," J. Lightwave Technol. **32**, 854–863 (2014).

[256] S. Ghosh, J. E. Sharping, D. G. Ouzounov, and A. L. Gaeta, "Resonant optical interactions with molecules confined in photonic band-gap fibers," Phys. Rev. Lett. **94**, 093902 (2005).

[257] L. W. Kornaszewski, N. Gayraud, J. M. Stone, W. N. Macpherson, A. K. George, J. C. Knight, D. P. Hand, and D. T. Reid, "Mid-infrared methane detection in a photonic bandgap fiber using a broadband optical parametric oscillator," Opt. Express **15**, 11219–11224 (2007).

[258] N. Gayraud, U. W. Kornaszewski, J. M. Stone, J. C. Knight, D. T. Reid, D. P. Hand, and W. N. MacPherson, "Mid-infrared gas sensing using a photonic bandgap fiber," Appl. Opt. **47**, 1269–1277 (2008).

[259] A. M. Stolyarov, A. Gumennik, W. McDaniel, O. Shapira, B. Schell, F. Sorin, K. Kuriki, G. Benoit, A. Rose, and J. D. Joannopoulos, "Enhanced chemiluminescent detection scheme for trace vapor sensing in pneumatically-tuned hollow core photonic bandgap fibers," Opt. Express **20**, 12407–12415 (2012).

[260] B. J. Eggleton, B. Luther-Davies, and K. Richardson, "Chalcogenide photonics," Nat. Photonics **5**, 141–148 (2011).

[261] J. S. Sanghera, L. B. Shaw, and I. D. Aggarwal, "Chalcogenide glass fiber-based mid-IR sources and applications," IEEE J. Sel. Topics Quantum Electron. **15**, 114–119 (2009).

[262] T. Frosch, M. Schmitt, T. Noll, G. Bringmann, K. Schenzel, and J. Popp, "Ultrasensitive in situ tracing of the alkaloid dioncophylline A in the tropical liana Triphyophyllum peltatum by applying deep-UV resonance Raman microscopy," Anal. Chem. **79**, 986–993 (2007).

[263] T. Frosch, N. Tarcea, M. Schmitt, H. Thiele, F. Langenhorst, and J. Popp, "UV Raman imaging-A promising tool for astrobiology: Comparative Raman studies with different excitation wavelengths on SNC martian meteorites," Anal. Chem. **79**, 1101–1108 (2007).

[264] E. B. Hanlon, R. Manoharan, T. W. Koo, K. E. Shafer, J. T. Motz, M. Fitzmaurice, J. R. Kramer, I. Itzkan, R. R. Dasari, and M. S. Feld, "Prospects for in vivo Raman spectroscopy," Phys. Med. Biol. **45**, R1–R59 (2000).

[265] G. J. Leggett, "Light-directed nanosynthesis: near-field optical approaches to integration of the top-down and bottom-up fabrication paradigms," Nanoscale **4**, 1840–1855 (2012).

[266] L. Vincetti, "Numerical analysis of plastic hollow core microstructured fiber for Terahertz applications," Opt. Fiber Technol. **15**, 398–401 (2009).

[267] L. Vincetti, V. Setti, and M. Zoboli, "Terahertz tube lattice fibers with octagonal symmetry," IEEE Photon. Technol. Lett. **22**, 972–974 (2010).

[268] H. Li, G. Ren, B.Zhu, Y. Gao, B. Yin, J. Wang, and S. Jian, "Guiding terahertz orbital angular momentum beams in multimode Kagome hollow-core fibers," Opt. Lett. **42**, 179–182 (2017).

[269] J. Anthony, R. Leonhardt, S. G. Leon-Saval, and A. Argyros, "THz propagation in kagome hollow-core microstructured fibers," Opt. Express **19**, 18470–18478 (2011).

[270] A. Dupuis, K. Stoeffler, B. Ung, C. Dubois, and M. Skorobogatiy, "Transmission measurements of hollow-core THz Bragg fibers," J. Opt. Soc. Am. B **28**, 896–907 (2011).

[271] J. T. Lu, C. H. Lai, T. F. Tseng, H. Chen, Y. F. Tsai, I. J. Chen, Y. J. Hwang, H. C. Chang, and C. K. Sun, "Terahertz polarization-sensitive rectangular pipe waveguides," Opt. Express **19**, 21532–21539 (2011).

[272] C. S. Ponseca, R. Pobre, E. Estacio, N. Sarukura, A. Argyros, M. C. Large, and M. A. van Eijkelenborg, "Transmission of terahertz radiation using a microstructured polymer optical fiber," Opt. Lett. **33**, 902–904 (2008).

[273] D. S. Wu, A. Argyros, and S. G. Leon-Saval, "Reducing the size of hollow terahertz waveguides," J. Lightwave Technol. **29**, 97–103 (2011).

[274] J. Yang, J. Zhao, C. Gong, H. Tian, L. Sun, P. Chen, L. Lin, and W. Liu, "3D printed low-loss THz waveguide based on Kagome photonic crystal structure," Opt. Express **22**, 22454–22460 (2016).

[275] W. Lu and A. Argyros, "Terahertz spectroscopy and imaging with flexible tube-lattice fiber probe," J. Lightwave Technol. **32**, 4019–4025 (2014).

[276] S. Atakaramians, A. Stefani, H. Li, M. S. Habib, J. G. Hayashi, A. Tuniz, X. Tang, J. Anthony, R. Lwin, A. Argyros, S. C. Fleming, B. T. Kuhlmey, "Fiber-drawn metamaterial for THz waveguiding and imaging," J. Infrared Millim. Terahertz Waves, 1–17 (2017).

[277] S. Okaba, T. Takano, F. Benabid, T. Bradley, L. Vincetti, Z. Maizelis, V. Yampolskii, F. Nori, and H. Katori, "Lamb-Dicke spectroscopy of atoms in a hollow-core photonic crystal fibre," Nat. Commun. **5**, 4096 (2014).

[278] S. A. Mousavi, D. J. Richardson, S. R. Sandoghchi, and F. Poletti, "First design of high birefringence and polarising hollow core anti-resonant fibre," in *Optical Communication (ECOC), 2015 European Conference on*, Valencia, 2015, pp. 1–3.

[279] M. J. Li, J. A. West, and K. W. Koch, "Modeling effects of structural distortions on air-core photonic bandgap fibers," J. Lightwave Technol. **25**, 2463–2468, (2007).

[280] E. N. Fokoua, D. J. Richardson, and F. Poletti, "Impact of structural distortions on the performance of hollow-core photonic bandgap fibers," Opt. Express **22**, 2735–2744 (2014).

[281] E. N. Fokoua, S. R. Sandoghchi, Y. Chen, G. T. Jasion, N. V. Wheeler, N. K. Baddela, J. R. Hayes, M. N. Petrovich, D. J. Richardson, and F. Poletti, "Accurate modelling of fabricated hollow-core photonic bandgap fibers," Opt. Express **23**, 23117–23132 (2015).

[282] R. J. Weiblen, C. R. Menyuk, R. R. Gattass, L. B. Shaw, and J. S. Sanghera, "Fabrication tolerances in As_2S_3 negative-curvature antiresonant fibers," Opt. Lett. **41**, 2624–2627 (2016).

[283] W. J. Wadsworth, F. Yu, and J. C. Knight, "Useful light from photonic crystal fibres," in *Conference on Lasers and Electro-Optics*, OSA Technical Digest (2016) (Optical Society of America, 2016), paper SW1I.5. (Mentioned in the talk).

[284] S. Chaudhuri, L. Van Putten, F. Poletti, and P. Sazio, "Low loss transmission in negative curvature optical fibers with elliptical capillary tubes," J. Lightwave Technol. **34**, 4228–4231(2016).

[285] L. D. van Putten, E. N. Fokoua, S. M. A. Mousavi, W. Belardi, S. Chaudhuri, J. V. Badding, and F. Poletti, "Exploring the effect of the core boundary curvature in hollow antiresonant fibers," IEEE Photon. Technol. Lett. **29**, 263–266 (2017).

[286] M. S. Habib, O. Bang, and M. Bache, "Low-loss hollow-core anti-resonant fibers with semi-circular nested tubes," IEEE J. Sel. Topics Quantum Electron. **22**, 4402106 (2016).

Curriculum Vitae

Chengli Wei

Address: 1825 S. 5th Street, Apt. 17, Waco, TX 76706
Phone: (254)723-3175
Email: chengli_wei@baylor.edu

EDUCATION

Baylor University, Waco, TX, US — 08/2012 – Present

- Electrical and Computer Engineering (Ph.D. Candidate)

Nankai University, Tianjin, China — 09/2009 – 07/2012

- Optics Engineering (M.S.)

Tianjin University, Tianjin, China — 09/2005 – 07/2009

- Optoelectronic Technology and Science (B.S.)

AWARDS AND HONORS

- Second place in student competition during Optical Society Of America (OSA) annual meeting (2017)
- Who's Who among Students in American Universities and Colleges (2017)
- E-poster presenter at Optical Society Of America (OSA) annual meeting (2017)
  (10% of award among accepted papers)
- Student travel award in IEEE Photonics Society Summer Topicals Meeting Series (2015)
- Baylor travel award to professional meetings (2014, 2015, 2016, 2017)

ARCHIVAL JOURNAL PUBLICATIONS

1. **C. Wei**, C. R. Menyuk, and J. Hu, "Polarization-filtering and polarization-maintaining low-loss negative curvature fibers," Opt. Express **26**, 9528–9540 (2018).
2. **C. Wei**, J. Weiblen, C. R. Menyuk, and J. Hu, "Negative curvature fibers," Adv. Opt. Photonics **9**, 504–561 (2017). **(Impact factor: 17.8)**
3. **C. Wei**, C. R. Menyuk, and J. Hu, "Comparison of loss in silica and chalcogenide negative curvature fibers as the wavelength varies", Front. Phys. **4**, 30 (2016).
4. **C. Wei**, C. R. Menyuk, and J. Hu, "Impact of cladding tubes in chalcogenide negative curvature fibers", IEEE Photon. J. **8**, 2200509 (2016).
5. **C. Wei**, C. R. Menyuk, and J. Hu, "Bending-induced mode non-degeneracy and coupling in chalcogenide negative curvature fibers," Opt. Express **24**, 12228–12239 (2016).
6. Z. Zhu, J. Yuan, H. Zhou, J. Hu, J. Zhang, **C. Wei**, F. Yu, S. Chen, Y. Lan, Y. Yang, Y. Wang, C. Niu, Z. Ren, J. Lou, Z. Wang, and J. Bao, "Excitonic resonant emission absorption of surface plasmon in transition metal dichalcogenides for chip-level electronic photonic integrated circuits," ACS Photonics **3**, 869–874 (2016).
7. J. Hu, C. R. Menyuk, **C. Wei**, L. B. Shaw, J. S. Sanghera, and I. D. Aggarwal, "Highly efficient cascaded amplification using Pr^{3+}-doped mid-infrared chalcogenide fiber

amplifiers," Opt. Lett. **40**, 3687–3690 (2015).

8. **C. Wei**, R. A. Kuis, F. Chenard, C. R. Menyuk, and J. Hu, "Higher-order mode suppression in chalcogenide negative curvature fibers," Opt. Express **23**, 15824–15832 (2015).
9. S. Li, Z. Wang, Y. Liu, T. Han, Z. Wu, **C. Wei**, H. Wei, J. Li, and W. Tong, "Bending sensor based on intermodal interference properties of two-dimensional waveguide array fiber," Opt. Lett. **37**, 1610–1612 (2012).
10. X. Zheng, Y. Liu, Z. Wang, T. Han**, C. Wei**, and J. Chen, "Transmission and temperature sensing characteristics of a selectively liquid-filled photonic-bandgap-fiber-based Sagnac interferometer," Appl. Phys. Lett. **100**, 141104 (2012).

REFERRED CONFERENCE PROCEEDINGS

1. **C. Wei**, J. Young, C. R. Menyuk, and J. Hu, "Temperature sensor using fluid-filled negative curvature fibers," in Proc. Conference on Lasers and Electro-Optics (CLEO), San Jose, CA, doc. ID 2929860 (May 2018).
2. C. R. Menyuk, **C. Wei**, J. Weiblen, J. Hu, R. Gattass, L. B. Shaw, and J. S Sanghera, "Chalcogenide negative curvature fibers," in Proc. SPIE 10435, Technologies for Optical Countermeasures XIV, 104350I (2017).
3. **C. Wei**, C. Menyuk, and J. Hu, "Bent negative curvature fibers using circular or elliptical cladding tubes," in Frontiers in Optics (Optical Society of America, 2017), paper JW4A.9.
4. **C. Wei**, C. Menyuk, and J. Hu, "Higher-order mode suppression in chalcogenide negative curvature fibers with gaps between cladding tubes," in Advanced Photonics 2016 (IPR, NOMA, Sensors, Networks, SPPCom, SOF), OSA Technical Digest (online) (Optical Society of America, 2016), paper JTu4A.32.
5. J. Hu, C. R. Menyuk, **C. Wei**, B. Shaw, J. S. Sanghera, and I. Aggarwal, "Pr^{3+}-doped mid-infrared chalcogenide fiber amplifiers using cascaded Amplification," in Proc. Conference on Lasers and Electro-Optics (CLEO), San Jose, CA, paper STh1O.7 (2016).
6. **C. Wei**, R. A. Kuis, F. Chenard, C. R. Menyuk, and J. Hu, "Mode coupling in chalcogenide negative curvature fibers," in Proc. Conference on Lasers and Electro-Optics (CLEO), San Jose, CA, paper JTu5A.93 (2016).
7. **C. Wei**, O. Alvarez, F. Chenard, and J. Hu, "Empirical glass thickness for chalcogenide negative curvature fibers," in Proc. 2015 IEEE Photonics Society Summer Topicals Meeting Series, Mid Infrared Photonics, Nassau, Bahamas, paper TuE3.3 (2015).
8. **C. Wei**, J. Hu, and C. Menyuk, "Bending-induced mode coupling in chalcogenide negative curvature fibers," in Proc. Advanced Photonics, Boston, MA, paper NT2C.5 (2015).
9. **C. Wei**, R. Kuis, F. Chenard, and J. Hu, "Chalcogenide negative curvature hollow-core photonic crystal fibers with low loss and low power ratio in the glass," in Proc. Conference on Lasers and Electro-Optics (CLEO), San Jose, CA, paper SM1N.5 (2014).
10. **C. Wei**, Z. Wang, Y. Liu, B. Liu, H. Zhang, and Y. Liu, "Coupling characteristics of a fluid-filled dual-core photonic crystal fiber based on temperature tuning", in SPIE/OSA/IEEE Asia Communications and Photonics, pp. 83071R-83071R. International Society for Optics and Photonics (2011).